DLR-IB-RM-OP-2020-66

Modeling and Control for Unmanned Stratospheric Flight Missions from Takeoff to Landing

Master's Thesis

Eduardo Rodrigues Della Noce

Deutsches Zentrum
DLR für Luft- und Raumfahrt

Institut für Robotik und Mechatronik	BJ.: 2020
	DLR-IB-RM-OP-2020-66

MASTERARBEIT

MODELING AND CONTROL FOR UNMANNED STRATOSPHERIC FLIGHT MISSIONS FROM TAKEOFF TO LANDING

Freigabe:	Der Bearbeiter:	Unterschriften
	Eduardo Rodrigues Della Noce	
	Betreuer:	
	Dr. Tin Muskardin	
	Dr. Konstantin Kondak	
	Der Institutsdirektor	
	Prof. Dr. Alin Albu-Schäffer	

Dieser Bericht enthält 134 Seiten, 83 Abbildungen und 42 Tabellen

Ort: Oberpfaffenhofen	Datum: 03.08.2020	Bearbeiter: Eduardo R. Della Noce	Zeichen:

Institute of Robotics and Mechatronics
German Aerospace Center

Technische Universität München

Technical University of Munich
Eduardo Rodrigues Della Noce

Master's Thesis

Modeling and Control for Unmanned Stratospheric Flight Missions from Takeoff to Landing

Supervisor: Prof. Dr. Alin Albu-Schäffer
Advisors: Dr. Tin Muskardin
Dr. Konstantin Kondak

Munich, Germany
2020

Statutory Declaration

I declare on oath towards the Institute of Robotics and Mechatronics of the German Aerospace Center and the Chair for Sensor Based Robotic Systems and Intelligent Assistance Systems of the Technical University of Munich that I have prepared the present Master's Thesis independently and with the aid of nothing but the resources listed in the bibliography.

Munich, August 3^{rd}, 2020

Eduardo Rodrigues Della Noce

"Through the new strangeness of noise and light he could just make the shape of Ford Prefect sitting back and laughing wildy.
A tremendous feeling of peace came over him. He knew that, at last, for once and forever, it was now all, finally, over."

— Douglas Adams, *Mostly Harmless*

Acknowledgments

To start with, I would like to thank everyone that was involved in the making of this work. First of all, I must express my gratitude to Dr. Tin Muskardin, with whom I had the pleasure of working with in the German Aerospace Center (*Deutsches Zentrum für Luft- und Raumfahrt*) (DLR) for the entire duration of my stay there, which is now completing over a year and four months; he was always willing to help and taught me a lot. I must also thank both Georg Balmer and Dr. Konstantin Kondak for trusting me with the amazing opportunity of working in such a unique project and consistently giving me very useful insights and feedback. This thesis would be impossible without any of these three people. I am also grateful to Prof. Dr. Alin Albu-Schäffer, to the Technical University of Munich (*Technische Universität München*) (TUM) and to the Institute of Robotics and Mechatronics of DLR for allowing me this opportunity. On this note, I must thank my home university as well, the Polytechnic School of the University of São Paulo, for providing me and others the chance to come to TUM as part of a Double Degree Program.

I would also like to take a moment to thank and appreciate my friends for always being there for me. I have no idea what would be of me without them and all the memories we created together. In particular I would like to mention Rafael Naß de Andrade and Catharina Martinez Moreira, who were here for me since the beginning of this journey to Germany, and are still here right until the end. They have also contributed valuable insights into this thesis, and I cannot thank them enough for everything, work or otherwise.

Finally, I am also thankful to my family, in particular my mother, Marly Rodrigues Della Noce, and my father, Edney Della Noce, for always supporting me in all my decisions. I am truly grateful for their love and everything they have ever done for me.

Abstract

High-Altitude Long Endurance (HALE) aircraft are platforms that can take flight to altitudes as high as $20km$ and can stay there for virtually unlimited amounts of time. This type of aircraft is the main focus of study of the presented thesis, which can be divided in two stages: in the first stage, time domain system identification is studied and applied to create a high fidelity model of a HALE aircraft, which is then used to evaluate the viability of landing such an aircraft on mobile platforms; and in the second stage, a geometry-based method is used to create models for the same aircraft at varying altitudes, which are then used to develop a gain scheduling strategy to allow for safe, stable flight from the ground to the stratosphere.

Available results of system identification for low altitude aircraft are examined, and a minimal model structure is found. With that, the procedure is applied to a HALE aircraft, and the fidelity of the model is evaluated by well-known standards, arriving at the conclusion that the model is of high fidelity. Then, using different sets of available data, the consistency in results of the method and model structure is also investigated.

Using the high fidelity model created, an analysis is made to evaluate the feasibility of landing the HALE Unmanned Aerial Vehicle (UAV) in an automatic way on top of a ground vehicle with a roof-mounted platform, which is a landing strategy proposed in other works. Controller synthesis is done for the individual vehicles and the cooperative control between them, leading to an examination of its stability and performance, using both deterministic and stochastic methods.

Shifting to the second phase of the work, the emphasis returns to the modeling of the aircraft, but instead, geometry based methods are used to generate models across different altitudes, covering the full flight envelope from the ground to the maximum altitude of HALEs in the stratosphere. The generated model is validated against data from real experiments, and its behavior throughout the flight envelope is analyzed.

Finally, to deal with the control instability that is present at higher altitudes, a gain scheduling strategy is proposed. This strategy is designed with a minimalistic philosophy, where the different gains are first analyzed to see which ones most influence the seen behavior, and then only those are used as design variables in an optimization scheme defined to find the ideal gain values to stabilize the system, while also changing said gains as little as possible.

Keywords: High Altitude Long Endurance Aircraft, Landing on Mobile Platforms, Stratospheric Flight of Unmanned Aerial Vehicle, System Identification, Gain Scheduling.

Contents

List of Figures

List of Tables

Symbols

Physical Quantities

m	Total mass
I	Moment of inertia with respect to the body frame
ρ	Air density

Important Quantities

V_a	True airspeed
V_k	Ground-speed
a	Absolute acceleration
χ	Course angle
γ	Flight path angle
α	Angle of attack
β	Sideslip angle
ω	Rotational engine speed
h	Altitude

Aircraft States

u	Air velocity on x-axis direction in body frame
v	Air velocity on y-axis direction in body frame
w	Air velocity on z-axis direction in body frame
ϕ	Roll angle
θ	Pitch angle
ψ	Yaw angle
p	Roll rate
q	Pitch rate
r	Yaw rate

Aircraft Forces and Moments

X	Force in x-axis direction
Y	Force in y-axis direction
Z	Force in z-axis direction
L	Moment around x-axis direction (roll)
M	Moment around y-axis direction (pitch)
N	Moment around z-axis direction (yaw)
$(\cdot)_b$	Forces and moments described in body frame
$(\cdot)_s$	Forces and moments described in stability frame
$(\cdot)^{aero}$	Forces and moments related to aerodynamics
$(\cdot)^{prop}$	Forces and moments related to propulsion

Control

δa	Aileron deflection
δe	Elevator deflection
δf	Flaps deflection
δr	Rudder deflection
δt	Throttle variation

Acronyms

AHRS	Attitude and Heading Reference System
AVL	Athena Vortex Laticce
CFD	Computational Fluid Dynamics
DLR	German Aerospace Center (*Deutsches Zentrum für Luft- und Raumfahrt*)
DOF	Degrees of Freedom
EKF	Extended Kalman Filter
EKS	Extended Kalman Smoothing
FAA	Federal Aviation Administration
GNSS	Global Navigation Satellite System
GOF	Goodness of Fit
GPS	Global Positioning System
HAP	High Altitude Platform
HALE	High-Altitude Long Endurance
IAE	Integral of Absolute Error
IEKF	Iterative Extended Kalman Filter
IMU	Inertial Measurement Unit
ISCA	Integral Squared of Controller Action
ISCD	Integral Squared of Controller Derivative
ISE	Integral of Squared Error
ITAE	Integral of Time-weighted Absolute Error

ITSE	Integral of Time-weighted Squared Error
KF	Kalman Filter
MEMS	Micro-Electro-Mechanical Systems
MIMO	Multiple-Input Multiple-Output
MPC	Model Predictive Control
NED	North East Down
NRMSE	Normalized Root Mean Squared Error
OEM	Output Error Method
PI	Proportinal-Integral
PID	Proportinal-Integral-Derivative
RMSE	Root Mean Squared Error
SISO	Single-Input Single-Output
TDPA	Time Domain Passivity Control Approach
TECS	Total Energy Control System
TIC	Theil's Inequality Coefficient
TUM	Technical University of Munich (*Technische Universität München*)
UAV	Unmanned Aerial Vehicle
UGV	Unmanned Ground Vehicle
VLM	Vortex Lattice Method
VRU	Vertical Reference Unit

Introduction

Over the past years, the amount of artificial satellites in orbit around Earth has been rapidly increasing, and currently there are 5972 of them in total [1]. However, as of 1st of April of 2020, only 2666 are still in operation [2]. This large discrepancy can be in the most part credited to the fact that it is nigh on impossible to maintain and repair this type of spacecraft. The large amount of inoperative satellites also raises the problem of collision with space debris. Furthermore, satellites are inherently restrained to their orbits, which restricts their use considerably, since it is unfeasible to accomplish tasks such as remaining quasi-stationary at an arbitrary location, relocating as necessary, patrolling over a designated area, among others.

Hence, there have been many recent projects on High Altitude Platforms (HAPs) and High-Altitude Long Endurance (HALE) aircraft from both industry and government entities in an attempt to find a viable way of extending on or even substituting satellites and solving the issues listed above. This particular type of Unmanned Aerial Vehicles (UAVs) is designed for stratospheric flight, achieving altitudes in the order of $20km$, and with the use of solar energy generators and appropriate batteries, they can remain airborne for virtually unlimited periods of time. This allows for their use in many different applications, such as earth observation, meteorology and establishing and maintaining communication networks. According to Romeo et al. [3], HALE UAVs are a promising alternative due to being cheaper, easier to maintain, and overall more flexible.

Some projects with the objective of creating functional HALE aircraft include Aquila by Facebook, Solara-50 by Google, Helios by NASA, Zephyr by Airbus and ELHASPA by DLR, among others [4]. Facebook and Google in particular had initially a lot of interest in this field as a means of solving the global connectivity problem [5]. However, as of today, Airbus is the only company with an operational HAP aircraft (Zephyr), and most of the competition has canceled their research on the topic. Facebook has ceased its activities after their Aquila aircraft had a structural failure during one of its landing approaches [6], while Google declared the end of their project due to "economics and technical feasibility" [7], having also had an accident earlier [8].

As seen in Jones [9], one of the main design goals of HALE aircraft is to maximize aerodynamic efficiency, so that they are able to operate for long periods of time at high altitudes. This translates to high aspect ratios and low airspeed, both measures taken to reduce drag. In order to support the weight of the UAV with low airspeed, it becomes necessary for the aircraft weight to be low, which, together with the aforementioned high aspect ratios, results in the necessity of having very lightweight structures. All of these factors combined generate a couple of challenges, which are still open:

- The lightweight design leads to low payload capacities.

- The low airspeed means, especially during landing, that even relatively small wind disturbances can lead to problems such as stall and high crosswind sensitivity (high crab angles at low wind speeds).
- The large dimensions lead to slow rotational dynamics, which not only make it harder to reject turbulence, but also increases the difficulty of performing a de-crab maneuver during landing, raising safety concerns.

In order to address these issues, Facebook attempted to remove the landing gear of its aircraft Aquila, landing in "a 500 foot circle of level gravel, about 6 inches deep and with the consistency of rough sand" [10]. In theory, the removal of the landing gear can mean increased payload capacity and the removal of a runway for landing as proposed can mitigate the concerns with wind disturbances. However, as seen in the accident report [6], it is mentioned that "the operator expected some damage during normal landings", which highlights an intrinsic flaw of this idea and demonstrates these problems are still mostly unsolved [11].

Moreover, as mentioned by Lee et al. [4], flights to the stratosphere cover a wide range of altitudes and Mach numbers, making the dynamic behavior of the aircraft vary significantly during the ascent, which leads to potential safety concerns. Addressing these issues is essential to enable further research and eventual mission deployment of these types of aircraft.

1.1 Project Background

The study of UAVs has long been a focus of the Flying Robots Group at the Institute of Robotics and Mechatronics of the German Aerospace Center (*Deutsches Zentrum für Luft- und Raumfahrt*) (DLR), which is closely cooperating with one of its spin-off companies Elektra Solar GmbH on the research and development of HAPs and HALE aircraft. The aircraft used in the aforementioned projects will be presented. Among the studies conducted over them, those related to system identification and landing of UAVs on mobile platforms are of particular interest to this work. Both of these points will also be addressed in the next sections.

1.1.1 Penguin BE UAV

Penguin BE UAV is a commercially available small electric high-wing unmanned aerial vehicle, developed by UAV Factory [12]. It has a $640Wh$ lithium polymer battery, a geared brushless propulsion with $2700W$ of available power, a wingspan of $3.30m$, a length of $2.27m$, and an empty weight of $14.9kg$ with a maximum payload of $6.60kg$ [13]. In terms of sensors equipped by DLR, it contains a 3DM-Gx3-25 Inertial Measurement Unit (IMU) from MicroStrain, a PSS-8 pitot tube from Simtec and a Novatel Flex-Pak6 RTK-GPS receiver and antenna [11]. Available as control surfaces are aileron, elevator and rudder in a V-Tail configuration, while thrust is generated by an electric motor with a propeller.

Figure 1.1: Penguin BE UAV. Source: [12].

1.1.2 Elektra 1 Solar

"Elektra One Solar OPS | UAS" is a solar electric aircraft developed by Elektra Solar GmbH. It has a wingspan of $13m$, a wing surface of $10m^2$, a maximum takeoff weight of $380kg$ and a maximum payload and battery weight of $200kg$ [14]. Elektra 1 Solar is equipped with a MTi 100-series all-in-one sensor which is capable of providing a Micro-Electro-Mechanical Systems (MEMS) based IMU, Vertical Reference Unit (VRU), Attitude and Heading Reference System (AHRS) and Global Navigation Satellite System (GNSS) data, as well as a PSS-8 pitot tube from Simtec [15]. Available as control surfaces are aileron, elevator and rudder, while thrust is generated by a electric motor with a propeller.

Figure 1.2: Elektra 1 Solar in flight. Source: [15].

1.1.3 Elektra 2 Solar

"Elektra Two Solar OPS | UAS" is a HALE aircraft developed by Elektra Solar GmbH. It has a wingspan of $27m$, a wing area of $28.6m^2$, a maximum takeoff weight of $600kg$ and a maximum payload and battery weight of $310kg$ [16]. Elektra 2 Solar is equipped with the same sensors as Elektra 1 Solar. Furthermore, it also has aileron, elevator, rudder and motor with propeller present for its control.

Figure 1.3: Elektra 2 Solar in flight. Source: [16].

1.1.4 System Identification

According to Zadeh [17], "System identification is the determination, on the basis of observation of input and output, of a system within a specified class of systems to which the system under test is equivalent." It is, in essence, a way of creating a model for a process based on experimental data.

Using system identification for the modeling of aircraft is a well-documented process. Hamel et al. [18] offer a historical overview of the evolution of this method. More of the process itself can be seen in Jategaonkar [19] and Klein et al. [20]. In summary, by performing specific maneuvers to excite the eigenmodes of the system, it is possible to use that flight data to generate a parameterized aerodynamic model of an aircraft. If the data acquired is precise enough, and the chosen model parameters are adequate to represent the system, it is possible to create local high fidelity models of the aircraft with this method, which enables its use for dynamic analysis and controller synthesis. In particular, for stratospheric missions, Lee et al. [4] suggest the use of a Global System Identification scheme, where simulations using prediction tools (such as Vortex Lattice Method (VLM)) can be used in conjunction with flight data in order to expand the region where the identified model can be considered high fidelity.

Recently, inside of DLR, this strategy has been used to create models for the three aircraft previously mentioned: Penguin BE, whose identification was done by Coelho [21] and Lee [15]; Elektra 1 Solar, whose identification was done by Lee [15] and Páez [22]; and Elektra 2 Solar, whose identification was done by Kalra [23].

1.1.5 Landing on Mobile Platforms

Another project which will be considered in this thesis is a landing strategy that utilizes a mobile ground vehicle in cooperation with the UAV for the touchdown of the aircraft instead of the use of a landing gear. This is a promising field of research that serves as an alternative way of increasing payload capacity and expanding the conditions in which the aircraft can safely land. According to Muskardin et al. [24], these two main objectives are achieved in the following way: first, the removal of the landing gear from the aircraft can reduce its weight by about 6 to 15% [25], thereby increasing the payload capacity; and second, it can increase operational availability, since with a moving platform the UAV is not required anymore to align with the runway direction, which removes the concerns with the de-crab maneuver during landing.

This concept was first mentioned in Laiacker et al. [26], whose article focused on the use of a multi-sensor system for the execution of a vision based landing, analyzing the state estimation, approach and landing control with tests on a fixed runway. In his thesis, Balmer [27] modeled the Penguin BE UAV using VLM and tested different types of control strategies for the UAV, comparing their performances and suitability for landing the UAV on a mobile platform. This was followed by Muskardin et al. [24], who then made a linear analysis of the cooperative control system and realized the first tests showing successful landings with the demonstrator setup (which consists of the Penguin BE UAV and a semi-autonomous automobile, shown in Figure 1.4). Further improvements and additional experimental results were presented by Muskardin et al. [28]. In parallel, both Persson et al. [29] and Pavani [30] worked on the development of a Model Predictive Control (MPC) which could be used for the landing procedure, generating desired inputs for both the UAV and the ground vehicle. Finally, a comprehensive analysis in simulation was added by Muskardin [11] to show the expected performance of the system in varying situations, while also proposing and comparing two different types of cooperative landing control architectures.

Figure 1.4: Demonstrator setup with Penguin BE and a semi-autonomous vehicle. Source: [28].

1.2 Problem Statement

While Kalra [23] has used the system identification method to create a model for the Elektra 2 aircraft, the performance metrics of it did not match the established threshold necessary for the model to have a response which can be considered representative of the system. Upon further inspection, the issue appears to be related to the data used, which contained problems such as drift, and the aerodynamic derivatives chosen, which seem to be over-fitting the system.

Furthermore, Muskardin's [11] analysis was done with only a small UAV, and as of this point in time, no analysis has been done with an actual HALE aircraft. Analyzing the performance of the developed landing system for such type of aerial vehicle is of crucial importance for the future of this project.

At last, to tackle the issues related to the wide range of Mach numbers, Reynolds numbers and altitudes, a way of modeling HALE UAVs at different altitudes must be studied, and a control strategy to safely cover the entire flight envelope must be developed.

1.3 Goals

The main subject of interest in this work is the Elektra 2 Solar aircraft, and the goal is to both analyze the feasibility and performance of its landing on a mobile platform and find a set of controller gains which can be scheduled to enable stratospheric flight safely. In order to achieve this, smaller steps must be taken, and the work can be essentially divided in four stages.

First, a high fidelity model of Elektra 2 Solar must be developed. To clear the concerns related to the chosen parameters used in the identification process, it is reasonable to re-evaluate the results for both Penguin BE and Elektra 1 Solar as well, making different selections and seeing how that impacts the system response and its performance metrics. Once a minimal set of parameters has been found, then data from different IMUs can be used from Elektra 2 Solar and one can attempt to create a model for Elektra 2 Solar using system identification with the new minimized set of aerodynamic derivatives with the data that has already been acquired. The consistency of the new model must then also be verified.

Second, the high fidelity Elektra 2 Solar model can then be used to perform a complete examination of its capabilities regarding the landing on a ground vehicle. For this, the simulation framework developed by Muskardin [11] must be adapted and the necessary optimizations must be repeated with the new aircraft. When all cooperative gains are correctly set, an analysis of disturbance rejection and landing performance can be performed, using both deterministic and stochastic approaches.

Following that, the focus changes to the development of models for Elektra 2 Solar at different altitudes. Since, at this point, no identification maneuvers can be performed at high altitudes, it is impossible to use the system identification process developed in the first stage to create the necessary models. Therefore, VLM will be used to generate models of the aircraft at different altitudes, and an analysis of the

changes in aircraft dynamics will be conducted. Even if VLM is not able to produce high fidelity models, its responses should still be at least coherent with what might be observed in the real aircraft, and therefore, its investigation could provide reasonable insights into the fundamental issues.

Finally, a gain scheduling strategy for Elektra 2 Solar has to be developed, to guarantee it can safely complete its flight up to the stratosphere. A minimalistic approach philosophy will be taken, which translates to seeking to change as few gains as possible, and each as little as possible. In order for this to be achieved, an initial investigation must be conducted by means of a sensitivity analysis to determine which gains are the most important to overcome any instabilities that may appear, and latter an optimization algorithm must be defined and used to find the optimal gains to control the aircraft at each chosen operating point.

1.4 Thesis Outline

This thesis is divided into seven chapters, and each of them shall be briefly introduced in the following paragraphs.

Chapter 1 gives an overview of the general state of HALE aircraft and the current challenges being faced in their deployment. The background of the related projects developed in DLR is given, as well as information of the aircraft with available data to analyze. Finally, the goals of this work are defined.

Chapter 2 presents the theoretical background required for the understanding of this thesis is presented. First, the general equations of motion used and the dynamics of aircraft are discussed. This is followed by an explanation of the available methods for system identification in the time domain of aircraft, which are used to model the aerodynamic forces that act on aerial vehicles. The control strategy used in Elektra 2 Solar is then presented. Lastly, the strategies considered and methods used to analyze the capabilities of landing aircraft on mobile platforms are shown.

Chapter 3 presents the parts of this project related to system identification of aircraft. A summary of previous works done at DLR related to the subject is presented. The relevant issues are then discussed, and adjustments to the methods used so far are explained, together with how they address the aforementioned problems. The methodology of testing is then presented, and finally, the new results acquired are shown and compared to the previous ones mentioned earlier.

Chapter 4 presents the advancements made in landing aircraft on mobile platforms. A quick overview of properties related to the current implementation is given, followed by the suggested adaptations to improve the shown performance. The methodology used for tuning the controllers of the aircraft, ground vehicle, and cooperative landing control systems are then explained, as well as the procedures utilized for analyzing the cooperative landing strategies, followed by the results acquired.

Chapter 5 presents the process of modeling an aircraft at high altitudes. An introduction is given, where the software used is described, along with the required inputs for them and its theoretical limitations. The results are then shown, and the

level of fidelity of the generated models is evaluated, along with a general analysis of its behavior.

Chapter 6 presents the strategy employed to stabilize the aircraft throughout its entire ascent towards high altitudes, in the form of gain scheduling. A small summary is given on what gain scheduling is, and some of its common applications. The proposed methodology of establishing a gain scheduling strategy is then discussed, going over the analysis necessary for it, and the criteria chosen for finding the optimal gain values at each operating point. The results acquired are then shown.

Chapter 7 concludes the work, while also providing paths that can be followed in future research.

Theoretical Background

2.1 Aircraft Equations of Motion and Dynamics

In this section, the considered equations of motion and relevant dynamics of aircraft are presented, which are based on a rigid body model with 6 Degrees of Freedom (DOF) and take aerodynamic, propulsion and gravitational forces and moments into consideration. First, many different frames that can be considered are all summarized, and the equations of motion are presented. This is followed by an overview of how the aerodynamic and propulsion forces and moments can be calculated and how they can be inserted into the equations of motion.

2.1.1 Coordinate Frames

Many coordinate frames can be found in the literature. Here, a summary of the relevant ones for this work is presented. More details on each one and others can be found on common literature, such as Cook [31] and Zipfel [32].

- *Aerodynamic frame*: has its origin on the aircraft's center of gravity; the x axis points to the direction of the aircraft's true airspeed; the y axis is defined as being perpendicular to the x and z axes according to the positive direction of the right hand rule; and the z axis points downwards in the symmetry plane of the aircraft. It moves with the aircraft and rotates with the relative airflow.
- *Body frame*: has its origin on the aircraft's center of gravity; the x axis points to the direction of the aircraft's nose, along the fuselage; the y axis points to the aircraft's right wing; and the z is defined as being perpendicular to the x and y axes according to the positive direction of the right hand rule. It moves and rotates with the aircraft.
- *Local (Runway) Frame*: has its origin centered at some point on the surface of the earth (for example, the beginning of an airport runway, in the centerline); the x axis points to a defined direction (for example, the direction of the runway); the y axis is defined as being perpendicular to the x and z axes according to the positive direction of the right hand rule; and the z axis points towards the earth's center. It does not move, and it rotates with the angular velocity of the Earth.
- *North East Down (NED) Frame*: has its origin on the aircraft's center of gravity; the x axis points to the geographical north pole; the y axis is defined as being perpendicular to the x and z axes according to the positive direction of the right hand rule; and the z axis points towards the earth's center. It moves with the aircraft, and rotates to always keep its directions true to the geographical directions.
- *Stability Frame*: has its origin on the aircraft's center of gravity; the x axis points to the projection of the true airspeed in the xz symmetry plane; the y axis points

to the aircraft's right wing; and the z is defined as being perpendicular to the x and y axes according to the positive direction of the right hand rule. It moves with the aircraft and rotates partly with the aircraft and partly with the relative airflow.

2.1.2 Equations of Motion

The equations of motion of the rigid body with 6 DOF model for aircraft are well known and their derivation is simple, as can been seen in Zipfel [32] and others [33; 34]. The non-linear, flat earth equations written in body frame are used, since they were considered sufficiently precise for the purposes of this work. All 12 aircraft states are inertally referenced (kinematic) quantities, describing the motion of the aircraft with respect to the ground. Furthermore, the aircraft is considered symmetric with respect to the xz plane. Lastly, the x and y navigation equations are omitted, since they are not relevant for the dynamic analysis of the aircraft. The equations can be written as follows:

Force equations

$$\dot{u} = a_x - g \cdot sin(\theta) + r \cdot v - q \cdot w \tag{2.1}$$
$$\dot{v} = a_y + g \cdot sin(\phi) \cdot cos(\theta) + p \cdot w - r \cdot u \tag{2.2}$$
$$\dot{w} = a_z + g \cdot cos(\phi) \cdot cos(\theta) + q \cdot u - p \cdot v \tag{2.3}$$

Kinematic equations

$$\dot{\phi} = p + (q \cdot sin(\phi) + r \cdot cos(\phi)) \cdot tan(\theta) \tag{2.4}$$
$$\dot{\theta} = q \cdot cos(\phi) - r \cdot sin(\phi) \tag{2.5}$$
$$\dot{\psi} = \frac{q \cdot sin(\phi) + r \cdot cos(\phi)}{cos(\theta)} \tag{2.6}$$

Moment equations

$$\dot{p} = C_1 \cdot p \cdot q - C_2 \cdot q \cdot r + C_3 \cdot L_b + C_4 \cdot N_b \tag{2.7}$$
$$\dot{q} = C_5 \cdot p \cdot r - C_6 \cdot (p^2 - r^2) + C_7 \cdot M_b \tag{2.8}$$
$$\dot{r} = C_8 \cdot p \cdot q - C_1 \cdot q \cdot r + C_4 \cdot L_b + C_9 \cdot N_b \tag{2.9}$$

Navigation equations

$$\dot{h} = u \cdot sin(\theta) - v \cdot sin(\phi) \cdot cos(\theta) - w \cdot cos(\phi) \cdot cos(\theta) \tag{2.10}$$

The acceleration terms are defined as $a_x = \frac{X_b}{m}$, $a_y = \frac{Y_b}{m}$ and $a_z = \frac{Z_b}{m}$. These accelerations, as well as the pitch rates, can be measured directly by an IMU [19].

The constants $C_1, ..., C_9$ are calculated as function of the moments of inertia of the aircraft:

$$C_1 = \frac{I_{xz} \cdot (I_x - I_y + I_z)}{I_x \cdot I_z - I_{xz}^2} \tag{2.11}$$

$$C_2 = \frac{I_z \cdot (I_z - I_y) + I_{xz}^2}{I_x \cdot I_z - I_{xz}^2} \tag{2.12}$$

$$C_3 = \frac{I_z}{I_x \cdot I_z - I_{xz}^2} \tag{2.13}$$

$$C_4 = \frac{I_{xz}}{I_x \cdot I_z - I_{xz}^2} \tag{2.14}$$

$$C_5 = \frac{I_z - I_x}{I_y} \tag{2.15}$$

$$C_6 = \frac{I_{xz}}{I_y} \tag{2.16}$$

$$C_7 = \frac{1}{I_y} \tag{2.17}$$

$$C_8 = \frac{(I_x - I_y) \cdot I_x + I_{xz}^2}{I_x \cdot I_z - I_{xz}^2} \tag{2.18}$$

$$C_9 = \frac{I_x}{I_x \cdot I_z - I_{xz}^2} \tag{2.19}$$

2.1.3 Aerodynamic Forces and Moments

The process of developing an accurate model of the aerodynamic forces of an aerial vehicle is generally costly and can take a long time, being normally done either by complex numerical simulations (such as Computational Fluid Dynamics (CFD)) or by experiments in wind tunnels. As another option, one can also use System Identification methods to achieve the same, as will be explained in Section 2.2.

When none of these methods are available, or the project is still in a conceptual phase, other alternatives used to generate low fidelity models are also possible, such as those based on VLM. Klöckner [35] presents an approach which generates results with decent reliability using only the geometry of the aircraft as input, with a precision of around 20%.

In the case of the current work, models will be generated with both System Identification (for use in landing analysis) and VLM (for a use in the gain scheduling). As will be explained in Section 2.2, the forces calculated by the use of System Identification are already given in body frame in a straightforward manner, and no conversion or discussion is necessary at this point. For VLM models, however, the forces are given in the stability frame, and are calculated based on dimensionless coefficients.

The forces and moments in the stability frame in terms of aerodynamic coefficients can be written as:

$$X_s = -\frac{1}{2} \cdot \rho \cdot V_a^2 \cdot S_{ref} \cdot C_D \tag{2.20}$$

$$Y_s = \frac{1}{2} \cdot \rho \cdot V_a^2 \cdot S_{ref} \cdot C_Y \tag{2.21}$$

$$Z_s = -\frac{1}{2} \cdot \rho \cdot V_a^2 \cdot S_{ref} \cdot C_L \tag{2.22}$$

$$L_s = \frac{1}{2} \cdot \rho \cdot V_a^2 \cdot S_{ref} \cdot b_{ref} \cdot C_l \tag{2.23}$$

$$M_s = \frac{1}{2} \cdot \rho \cdot V_a^2 \cdot S_{ref} \cdot c_{ref} \cdot C_m \tag{2.24}$$

$$N_s = \frac{1}{2} \cdot \rho \cdot V_a^2 \cdot S_{ref} \cdot b_{ref} \cdot C_n \tag{2.25}$$

where S_{ref} is the plan-form area of the wing, b_{ref} is the wing span, and c_{ref} is the reference cord length.

Each coefficient $C_D, C_Y, C_L, C_l, C_m, C_n$ can be calculated as a function of multiple different factors, such as true airspeed V_a, angle of attack α, sideslip angle β, derivatives $\dot{\alpha}$ and $\dot{\beta}$, angular rates p, q, r, Mach number Ma, control surface deflections $\delta a, \delta e, \delta r$, among others. Each coefficient which relates other quantities to the aerodynamic coefficients are called aerodynamic stability and control derivatives, which can be found locally for a point in the flight envelope given the aircraft's geometry, Reynolds' number, air density, viscosity and flap setting.

To use these calculated forces and moments, which are in stability frame, in the equations of motion, which are expressed in body frame, a rotation around the angle of attack $\alpha = atan(w/u)$ is necessary. As such:

$$X_b^{aero} = X_s \cdot cos(\alpha) - Z_s \cdot sin(\alpha) \tag{2.26}$$

$$Y_b^{aero} = Y_s \tag{2.27}$$

$$Z_b^{aero} = X_s \cdot sin(\alpha) + Z_s \cdot cos(\alpha) \tag{2.28}$$

$$L_b^{aero} = L_s \cdot cos(\alpha) - N_s \cdot sin(\alpha) \tag{2.29}$$

$$M_b^{aero} = M_s \tag{2.30}$$

$$N_b^{aero} = L_s \cdot sin(\alpha) + N_s \cdot cos(\alpha) \tag{2.31}$$

2.1.4 Propulsion Forces and Moments

The propulsion forces and moments are normally modeled using experimental data, and the choices of model can vary widely depending on the type of propulsion considered. It is also possible to obtain a model for them with system identification as well, as will be discussed in Section 2.2. For this work, all reviewed aircraft have a single propeller as a source of thrust, and a simple model of both electric motor and propeller will be used.

First, the moment generated by the motor itself can be calculated as:

$$Q_{motor} = \frac{P_{motor}}{\omega} \tag{2.32}$$

where P_{motor} is the motor power, which can be calculated as a function of the input throttle.

Second, the thrust force and torque from the propeller can be calculated as:

$$T_{propeller} = C_T \cdot \frac{4}{\pi^2} \cdot \rho \cdot R_{prop}^4 \cdot \omega^2 \tag{2.33}$$

$$Q_{propeller} = C_P \cdot \frac{-4}{\pi^3} \cdot \rho \cdot R_{prop}^5 \cdot \omega^2 \tag{2.34}$$

where C_T and C_P are the coefficients of thrust and power, respectively, and R_{prop} is the propeller radius. The coefficients of thrust and power can be experimentally acquired (as seen on Brandt et al. [36]) or approximated (as seen in Klöckner [35]) and, in general terms, calculated as function of the advance ratio (defined as $J_{ratio} = (\pi \cdot V_a) / (\omega \cdot R_{prop})$), Reynolds number Re and rotational engine speed ω.

Lastly, the rotational engine speed has its own differential equation, in the form:

$$(I_{propeller} + I_{motor}) \cdot \dot{\omega} = Q_{motor} + Q_{propeller} \tag{2.35}$$

With these quantities in hand, the contribution of the motor and propeller to the aircraft dynamics can be summarized in the following equations in the body frame:

$$X_b^{prop} = T_{propeller} \tag{2.36}$$

$$Y_b^{prop} = 0 \tag{2.37}$$

$$Z_b^{prop} = 0 \tag{2.38}$$

$$L_b^{prop} = -Q_{motor} \tag{2.39}$$

$$M_b^{prop} = T_{propeller} \cdot (z_{propeller} - z_{CG}) \tag{2.40}$$

$$N_b^{prop} = 0 \tag{2.41}$$

The term M_b^{prop} reflects how the propeller center is not aligned with the center of gravity of the aircraft, and therefore, a force generated there in x direction is bound to also generate a moment with that distance as lever.

2.2 Time Domain Aircraft System Identification

As mentioned in Section 1.1.4, system identification is a strategy that allows the creation of high fidelity models based on experimental data. The process as a whole can be separated into three main stages: data gathering, identification and validation. For the identification stage in this work, the Two Step Method will be used. Although the Output Error Method (OEM) is the most popular strategy for time domain aircraft system identification [37; 38], the Two Step Method has been shown to be able to produce similar results to those of OEM [39] and has two key advantages, those being: the easiness with which the aerodynamic structure can be changed, even in nonlinear cases [19; 40; 41]; and the possibility of extending its results with an incremental model update scheme [15].

The Two Step Method has its name due to separating the identification phase in two separate processes: first, a data compatibility check (or flight path reconstruction);

and second, the parameter identification process. The process of system identification using the Two Step Method is summarized in Figure 2.1 and each step will be given more details in the following sections.

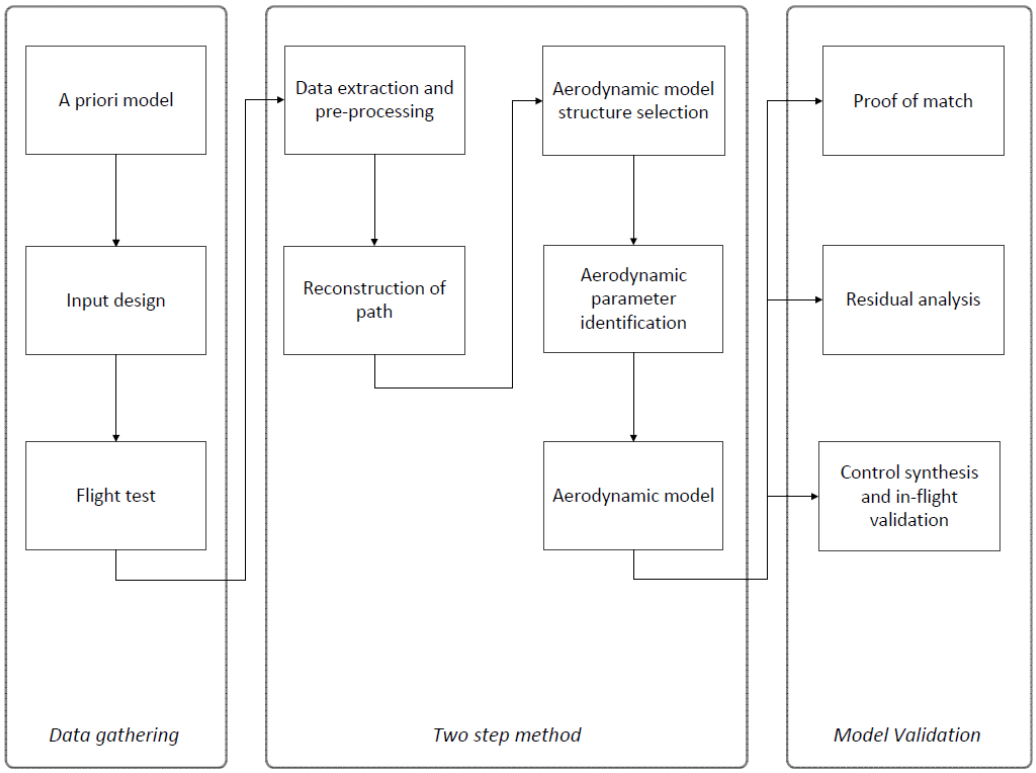

Figure 2.1: System Identification process with the Two Step Method. Source: [15].

2.2.1 Data Gathering

As previously mentioned, experiments need to be realized to get data for system identification. However, these experiments must be carefully considered and designed, otherwise it is impossible to create any kind of sensible data from them. Therefore, an initial model must be prepared and an identifiability analysis must be carried out, where the response of the system is evaluated for different maneuvers and it is analyzed for each maneuver whether there is enough information in it to identify the chosen parameters. In terms of available maneuvers, Jategaonkar [19] offers a selection to specifically excite different eigenmodes and general information of the aircraft. These include:

- Elevator 3-2-1-1: short period
- Elevator pulse: phugoid
- Bank angle: level turn maneuver
- Aileron/spoiler: bank-to-bank maneuver
- Rudder doublet: dutch roll
- Thrust doublet: for propulsion identification

In flight experiments, each selected maneuver is executed more than once to mitigate any noise that might be on the data due to impossible-to-predict disturbances. With that done, the data is also separated in identification data and validation data; so one set of the maneuvers is used to find the desired aerodynamic parameters, and the other is used solely for comparison with the prediction generated from the first set.

2.2.2 Data Compatibility Check (Flight Path Reconstruction)

Once the gathered data has been extracted and the all the necessary pre-processing of it has been done, the stage is set for the beginning of the identification process. In this first step, the data measured must be corrected for any sensor biases and drifts that might be in place, while also being smoothed to eliminate noise. There is a variety of methods available, as seen in Mulder et al. [42], but for this project we focus on how to achieve this with two different approaches: a stochastic one with a Kalman Filter (KF), and a deterministic one with OEM.

2.2.2.1 Kalman Filter

According to Jategaonkar [19], for processes where at least part of the inputs have a random pattern and are non-measurable, a straightforward integration scheme is not enough for an accurate estimation of the states, as would be the case in a purely deterministic system. In this context, Kalman Filtering is a stochastic approach that is able to efficiently estimate said states in linear systems [43]. Its two main advantages are its yielding of a minimum variance estimator and its recursive operation suitable for computational implementation [19]. The scheme is essentially composed of two stages, one for prediction, and another for correction. For nonlinear problems, an Extended Kalman Filter (EKF) is available, which works in a similar manner to its linear counterpart. The derivation of the estimation-before-modelling approach for the use of EKF in flight path reconstruction can be found in different authors [44–46].

An EKF method must be written in the form of:

$$\dot{x} = f(x(t), u(t), \mathfrak{w}(t)) \tag{2.42}$$

$$y(t) = g(x(t)) \tag{2.43}$$

$$z(t_k) = y(t_k) + \mathfrak{v}(t_k) \tag{2.44}$$

where $x(t)$ is the state vector, $u(t)$ is the measured inputs vector, $y(t)$ is the observation vector in continuous time, $z(t_k)$ is the observation vector in discrete time and $\mathfrak{w}(t)$ and $\mathfrak{v}(t_k)$ are noise vectors from the process and measurements respectively.

The state vector is defined as $x(t) = [x_a(t), \mathfrak{A}(t), \Theta]^T$, with $x_a(t) = [u, v, w, p, q, r, \phi, \theta, \psi, h]^T$ being the aircraft states, $\mathfrak{A}(t) = [\mathfrak{A}_0, \mathfrak{A}_1, \mathfrak{A}_2]^T$ being a vector that represents forces and moments where $\mathfrak{A}_i(t) = [X, Y, Z, L, M, N]^T$ and $\Theta = [\Delta a_x, \Delta a_y, \Delta a_z, \Delta p, \Delta q, \Delta r, \Delta\alpha, \Delta\beta, K_{V_a}]^T$ being the vector that represents biases and scaling factors of sensors.

The forces and moments in the estimation-before-modeling approach are modeled as a third order Gauss-Markov process with Gaussian white noise $\mathfrak{w}$ (shown below), which results in a quadratic polynomial interpolation of the forces and moments as a function of time, with its coefficients being updated at each time step recursively [15].

This approach yields good tolerance to low sampling rate in the measurement, as well as sensor noises [47].

$$\begin{bmatrix} \dot{\mathfrak{A}}_0 \\ \dot{\mathfrak{A}}_1 \\ \dot{\mathfrak{A}}_2 \end{bmatrix} = \begin{bmatrix} 0 & 1 & 0 \\ 0 & 0 & 1 \\ 0 & 0 & 0 \end{bmatrix} \begin{bmatrix} \mathfrak{A}_0 \\ \mathfrak{A}_1 \\ \mathfrak{A}_2 \end{bmatrix} + \begin{bmatrix} \mathfrak{w}_{\mathfrak{A}_0} \\ \mathfrak{w}_{\mathfrak{A}_1} \\ \mathfrak{w}_{\mathfrak{A}_2} \end{bmatrix} \tag{2.45}$$

Biases related to accelerations are modeled as Markov processes, while biases related to angular rates are considered constants.

$$\dot{\Delta a_i} = -\frac{1}{\tau}\Delta a_i + \mathfrak{w}_{\Delta a_i} \tag{2.46}$$

$$\dot{\Delta p} = \dot{\Delta q} = \dot{\Delta r} = 0 \tag{2.47}$$

where τ is an arbitrary time constant, generally chosen between 1 and 10 [15].

As observation variables, one can then define $y(t) = [u_m, v_m, w_m, p_m, q_m, r_m, \phi_m, \theta_m, \psi_m, h_m, V_{a_m}, \alpha_m, \beta_m, a_{x_m}, a_{y_m}, a_{z_m}]^T$, which thus means $z(t_k) = [u_{GPS}, v_{GPS}, w_{GPS}, p_{IMU}, q_{IMU}, r_{IMU}, \phi_{KF}, \theta_{KF}, \psi_{KF}, h_{GPS}, V_{a_{AP}}, \alpha_{est}, \beta_{est}, a_{x_{IMU}}, a_{y_{IMU}}, a_{z_{IMU}}]^T$. The Euler angles are estimated using a KF which runs in real time and can mitigate the inherent drawbacks of accelerometers and gyroscopes. α_{est} and β_{est} are optional estimated values of the angle of attack and side-slip angle, which can be done as seen in [48]. The scaling factor K_{V_a} corrects the measurements form the airdata probe. Finally, if the position of the IMU relative to the center of gravity is known, the acceleration measurements can also be corrected for that. The measurement model, therefore, can be found below.

$$u_m(t) = u(t), \qquad u_{GPS}(t_k) = u_m(tk) + \mathfrak{v}_u(t_k) \tag{2.48}$$

$$v_m(t) = v(t), \qquad v_{GPS}(t_k) = v_m(tk) + \mathfrak{v}_v(t_k) \tag{2.49}$$

$$w_m(t) = w(t), \qquad w_{GPS}(t_k) = w_m(tk) + \mathfrak{v}_w(t_k) \tag{2.50}$$

$$p_m(t) = p(t) + \Delta p, \qquad p_{IMU}(t_k) = p_m(tk) + \mathfrak{v}_p(t_k) \tag{2.51}$$

$$q_m(t) = q(t) + \Delta q, \qquad q_{IMU}(t_k) = q_m(tk) + \mathfrak{v}_q(t_k) \tag{2.52}$$

$$r_m(t) = r(t) + \Delta r, \qquad r_{IMU}(t_k) = r_m(tk) + \mathfrak{v}_r(t_k) \tag{2.53}$$

$$\phi_m(t) = \phi(t) \qquad \phi_{KF}(t_k) = \phi_m(tk) + \mathfrak{v}_\phi(t_k) \tag{2.54}$$

$$\theta_m(t) = \theta(t) \qquad \theta_{KF}(t_k) = \theta_m(tk) + \mathfrak{v}_\theta(t_k) \tag{2.55}$$

$$\psi_m(t) = \psi(t) \qquad \psi_{KF}(t_k) = \psi_m(tk) + \mathfrak{v}_\psi(t_k) \tag{2.56}$$

$$h_m(t) = h(t), \qquad h_{GPS}(t_k) = h_m(tk) + \mathfrak{v}_h(t_k) \tag{2.57}$$

$$V_{a_m}(t) = K_{V_a}\sqrt{u(t)^2 + v(t)^2 + w(t)^2}, \qquad V_{a_{AP}}(t_k) = V_{a_m}(t_k) + \mathfrak{v}_{V_a}(t_k) \tag{2.58}$$

$$\alpha_m(t) = arctan\frac{w(t)}{u(t)} + \Delta\alpha, \qquad \alpha_{est}(t_k) = \alpha_m + \mathfrak{v}_\alpha(t_k) \tag{2.59}$$

$$\beta_m(t) = arcsin\frac{v(t)}{\sqrt{u(t)^2 + v(t)^2 + w(t)^2}} + \Delta\beta, \quad \beta_{est}(t_k) = \beta_m + \mathfrak{v}_\beta(t_k) \tag{2.60}$$

$$a_{x_m}(t) = \frac{X(t)}{m} - (q(t)^2 + r(t)^2) \cdot x_{IMU} + (p(t) \cdot q(t) - \dot{r}(t)) \cdot y_{IMU} + (p(t) \cdot r(t) + \dot{q}(t)) \cdot z_{IMU} + \Delta a_x \tag{2.61}$$

$$a_{x_{IMU}}(t_k) = a_{x_m}(t_k) + \mathfrak{v}_{a_x}(t_k) \tag{2.62}$$

$$a_{y_m}(t) = \frac{Y(t)}{m} - (p(t) \cdot q(t) + \dot{r}(t)) \cdot x_{IMU} + (p(t)^2 + r(t)^2) \cdot y_{IMU} + (q(t) \cdot r(t) + \dot{p}(t)) \cdot z_{IMU} + \Delta a_y \tag{2.63}$$

$$a_{y_{IMU}}(t_k) = a_{y_m}(t_k) + \mathfrak{v}_{a_y}(t_k) \tag{2.64}$$

$$a_{z_m}(t) = \frac{Z(t)}{m} - (p(t) \cdot r(t) - \dot{q}(t)) \cdot x_{IMU} + (q(t) \cdot r(t) + \dot{p}(t)) \cdot y_{IMU} + (p(t)^2 + q(t)^2) \cdot z_{IMU} + \Delta a_z \tag{2.65}$$

$$a_{z_{IMU}}(t_k) = a_{z_m}(t_k) + \mathfrak{v}_{a_z}(t_k) \tag{2.66}$$

About the type of KF to be used, Lee [15] performed a study including a variety of possibilities and concluded an approach with an Iterative Extended Kalman Filter (IEKF) with backward Extended Kalman Smoothing (EKS) provided the best results.

2.2.2.2 Output Error Method

While OEM is generally used for the identification as a whole, as mentioned in Section 2.2, it can also be used exclusively to determine the biases of the gathered data, as has been done by multiple authors [21; 39; 40; 49]. When compared to Kalman Filtering, since this is a deterministic approach, it can prove itself to be more attractive to use when there is no previous known information about the statistics of noise and sensor bias [19; 50].

As implemented, this method tries to identify the biases in the sensors for both angular rates and accelerations measured. The nonlinear state equations considered are as follows:

$$\dot{u} = (a_{xm} - \Delta a_x) - g \cdot sin(\theta) + (r_m - \Delta r) \cdot v - (q_m - \Delta q) \cdot w \tag{2.67}$$

$$\dot{v} = (a_{ym} - \Delta a_y) + g \cdot sin(\phi) \cdot cos(\theta) + (p_m - \Delta p) \cdot w - (r_m - \Delta r) \cdot u \tag{2.68}$$

$$\dot{w} = (a_{zm} - \Delta a_z) + g \cdot cos(\phi) \cdot cos(\theta) + (q_m - \Delta q) \cdot u - (p_m - \Delta p) \cdot v \tag{2.69}$$

$$\dot{\phi} = (p_m - \Delta p) + ((q_m - \Delta q) \cdot sin(\phi) + (r_m - \Delta r) \cdot cos(\phi)) \cdot tan(\theta) \tag{2.70}$$

$$\dot{\theta} = (q_m - \Delta q) \cdot cos(\phi) - (r_m - \Delta r) \cdot sin(\phi) \tag{2.71}$$

$$\dot{\psi} = \frac{(q_m - \Delta q) \cdot sin(\phi) + (r_m - \Delta r) \cdot cos(\phi)}{cos(\theta)} \tag{2.72}$$

$$\dot{h} = u \cdot sin(\theta) - v \cdot sin(\phi) \cdot cos(\theta) - w \cdot cos(\phi) \cdot cos(\theta) \tag{2.73}$$

where the subscript m indicates the measurements (which are given as input), and prescript Δ indicates a bias (which is the parameters that need to be estimated and are here assumed constant). The states are initialized with the measured values at the start of each maneuver, and a forward simulation with the above equations is performed.

The responses obtained, called the observed states, are then compared to the measured states, and using gradient-based method, an optimization is run to maximize the likelihood function, which can be done by minimizing the determinant of the error covariance matrix. More details can be found on [19]. In essence, the biases are considered design variables, and the error between observed and measured states is the objective function.

2.2.3 Parameter Identification

After the data has been processed, the forces and moments that act on the aircraft from aerodynamics and propulsion can be reconstructed. This is done by default when using KF with the estimations and EKS, and, in the case of OEM, they can be calculated using the corrected accelerations and angular rates.

With the estimated forces, the model structure must be defined. This involves choosing the equations that can best represent the system, and which parameters from it must be found. Often, a linear derivative aerodynamics model is used, which, in the xz plane, has the form:

$$X = X_0 + X_u \cdot u + X_w \cdot w + X_q \cdot q + X_{\delta_e} \cdot \delta_e + X_{\delta_t} \cdot \delta_t \tag{2.74}$$

$$Z = Z_0 + Z_u \cdot u + Z_w \cdot w + Z_q \cdot q + Z_{\delta_e} \cdot \delta_e \tag{2.75}$$

$$M = M_0 + M_u \cdot u + M_w \cdot w + M_q \cdot q + M_{\delta_e} \cdot \delta_e \tag{2.76}$$

where each coefficient is called an aerodynamic, control surface or propulsion derivative. The use of this equation comes from the derivation of state space representation of aircraft, which can be found in the literature [19; 34; 51]. Alternatively, it can also be seen as a multivariate linear Taylor series approximation. On this note, the method is flexible enough to allow for the use of nonlinear equations as well, which can contain nonlinear terms coming from the same Taylor expression interpretation. Lee [15], for example, suggested the use of the following nonlinear equations:

$$\begin{aligned} X = {} & X_0 + X_u \cdot u + X_w \cdot w + X_q \cdot q + X_{\delta_e}\delta_e + X_{\delta_t} \cdot \delta_t \\ & + X_{wq} \cdot w \cdot q + X_{w\delta_e} \cdot w \cdot \delta_e + X_{w^2} \cdot w^2 \end{aligned} \tag{2.77}$$

$$\begin{aligned} Z = {} & Z_0 + Z_u \cdot u + Z_w \cdot w + Z_q \cdot q + Z_{\delta_e}\delta_e \\ & + Z_{wq} \cdot w \cdot q + Z_{w\delta_e} \cdot w \cdot \delta_e + Z_{w^2} \cdot w^2 \end{aligned} \tag{2.78}$$

$$\begin{aligned} M = {} & M_0 + M_u \cdot u + M_w \cdot w + M_q \cdot q + M_{\delta_e}\delta_e \\ & + M_{wq} \cdot w \cdot q + M_{w\delta_e} \cdot w \cdot \delta_e + M_{w^2} \cdot w^2 \end{aligned} \tag{2.79}$$

The states used in any case can be the directly measured states from Global Positioning System (GPS) and other sources, or can come from the estimated and smoothed states. Once an appropriate model has been chosen, ordinary least squares can be used to find each of the coefficients. More on the use of ordinary least squares for system identification can be found in Ljung [52].

2.2.4 Validation

As a general concept, validation can be done at each step of the process. It is done by seeing how well the simulated data and measured data match, and this can

be performed with both the identification set and the validation set. After the data compatibility check, one can validate the biases and the smoothing of the accelerations and angular rates by comparing the states resulting from the forward simulation to the measured states. After the parameter identification, one can compare the forces generated from the model (using the measured data) to the estimated forces. And finally, the aerodynamic model as a whole can be validated by realizing a complete forward simulation with the identified aerodynamic and propulsion parameters, and comparing the forces and states of this simulation to the estimated forces and measured states.

There are many statistical parameters which can be used as performance metrics available in the literature. Jategaonkar [19] suggests the use of Goodness of Fit (GOF) and Theil's Inequality Coefficient (TIC) as possible metrics for validation of model prediction capabilities. Other parameters include the coefficient of determination R^2, the Root Mean Squared Error (RMSE) and the Normalized Root Mean Squared Error (NRMSE). For a set z of measured data, and a set y of simulated data, these statistical metrics can be calculated as:

$$R^2 = 1 - \frac{||z(t_k) - y(t_k)||^2}{||z(t_k) - \overline{z}||^2} \tag{2.80}$$

$$RMSE = \sqrt{\frac{\sum_{k=1}^{N}[z(t_k) - y(t_k)]^2}{N}} \tag{2.81}$$

$$NRMSE = \frac{RMSE}{z_{max} - z_{min}} \tag{2.82}$$

$$GOF = NMSE = 1 - \frac{\sum_{k=1}^{N}[z(t_k) - y(t_k)]^2}{\sum_{k=1}^{N}[z(t_k) - \overline{z}]^2} \tag{2.83}$$

$$TIC = \frac{\sqrt{\frac{1}{N}\sum_{k=1}^{N}[z(t_k) - y(t_k)]^2}}{\sqrt{\frac{1}{N}\sum_{k=1}^{N} z(t_k)} + \sqrt{\frac{1}{N}\sum_{k=1}^{N} y(t_k)}} \tag{2.84}$$

where $\overline{z}$ is the average value of z and z_{max}, z_{min} are the maximum and minimum value of z respectively. If the vector norm $||\cdot||$ is taken to be the L2-norm, then R^2 and GOF are equivalent.

According to Jategaonkar [19], TIC can be more relevant than GOF when analyzing correlation between the simulated data and the measured data, since the latter may considered a straight line better than a signal that has similar amplitude and dampening but is shifted. A value of $TIC < 0.3$ indicates a good match between data [19].

A summary of the statistical metrics is given on Table 2.1. More information can be found on Jategaonkar et al. [53] and Rencher et al. [54].

Aside from these standard statistical parameters, other means of validation come from the Federal Aviation Administration (FAA)'s standards of fidelity [55], which establish when a model can be considered high fidelity for the simulation of an aircraft. Table 2.2 summarizes two of the tests relevant for system identification and their criteria of tolerance for dynamics.

Statistical Measure	Range (from Best Match to Worst Match)
R^2	$1 \rightarrow -\infty$
$RMSE$	$0 \rightarrow +\infty$
$NRMSE$	$0 \rightarrow +\infty$
GOF	$1 \rightarrow -\infty$
TIC	$0 \rightarrow 1$

Table 2.1: General characteristics of important statistical measures for validation.

Tests	Tolerances	Flight Condition	Comments
phugoid dynamics	±10% of period; 10% of time to half or double amplitude, or ±0.02 of damping ratio	Cruise	test should include three full cycles (6 overshoots after input completed) or that sufficient to determine time to half or double amplitude, whichever is less
short period dynamics	±1.5° pitch or 2°/sec. pitch rate; ±0.10g normal acceleration	Cruise	test in normal and non-normal control state.

Table 2.2: FAA criteria for high fidelity simulation. Adapted from: [55].

2.3 Total Energy Control System (TECS)

The Total Energy Control System (TECS) is a Multiple-Input Multiple-Output (MIMO) control strategy introduced by Lambregts [56] which is capable of decoupling airspeed and altitude control by using coordinated inputs of elevator and throttle. This is a very challenging feat to do with a classical Single-Input Single-Output (SISO) strategy, yet it is very important for landing maneuvers on mobile platforms (which will be talked about more in Section 2.4), as being able to overcome longitudinal errors without influencing the altitude of the aircraft is required, especially in the final phase of touchdown [11; 27].

An intuitive introduction into the core workings of TECS is now given. The following development can be found in the related literature [11; 27; 56–58].

If a single point-mass model is considered, the energy of the aircraft at any point can be written as:

$$E = \frac{1}{2} \cdot m \cdot V^2 + m \cdot g \cdot (h - h_0) \tag{2.85}$$

and the applied power of the system is then:

$$P = \dot{E} = m \cdot V \cdot \dot{V} + m \cdot g \cdot \dot{h} \tag{2.86}$$

Now, looking from a input and loss of energy perspective, the applied power can also be written as function of generated thrust and induced drag:

$$P = (T - D) \cdot V \tag{2.87}$$

Note that lift and side force are both perpendicular to the velocity of the aircraft, and therefore, do not produce any work and don't contribute to the energy or power. Since equations 2.86 and 2.87 both represent the same quantity, their right-hand side terms must also be equal, and, using the definition of the flight path angle $sin(\gamma) = \frac{\dot{h}}{V}$, an equation relating them can be written:

$$\frac{\dot{V}}{g} + sin(\gamma) = \frac{T - D}{mg} \tag{2.88}$$

At this point, two important considerations are made:

- Flight path angles are assumed small, and as such, $sin(\gamma)$ can be approximated to γ;
- The variation of drag is considered slow, and therefore, $T - D$ can, for a moment, be considered a variation of thrust around its local trim condition δT.

The final equation can then be written as:

$$\frac{\delta T}{m \cdot g} = \frac{\dot{V}}{g} + \gamma \tag{2.89}$$

This equation essentially gives the short-term requirement increase or decrease of thrust for a desired change in either velocity ($\dot{V}$) or altitude (γ). Also of note is that, if only the thrust increases or decreases, both the speed and the altitude will simultaneously increase or decrease accordingly; in other words, it is only capable of increasing or decreasing the total system energy. Thus, for an effective independent control, TECS still needs a second actuator to handle the conversion of energy.

This actuator is chosen to be the elevator, since it does not influence the total power, and can influence $\dot{V}$ and γ in opposing ways; what this means is that, given a deflection on the elevator, if the velocity goes up, the altitude will go down, and vice-versa. The control variable, therefore, can be taken to be $\frac{\dot{V}}{g} - \gamma$.

In summary then, the thrust control determines the energy variation of the system, while the elevator control determines its distribution between kinetic and potential energy. This process of energy increase, decrease or conversion is illustrated in Figure 2.2.

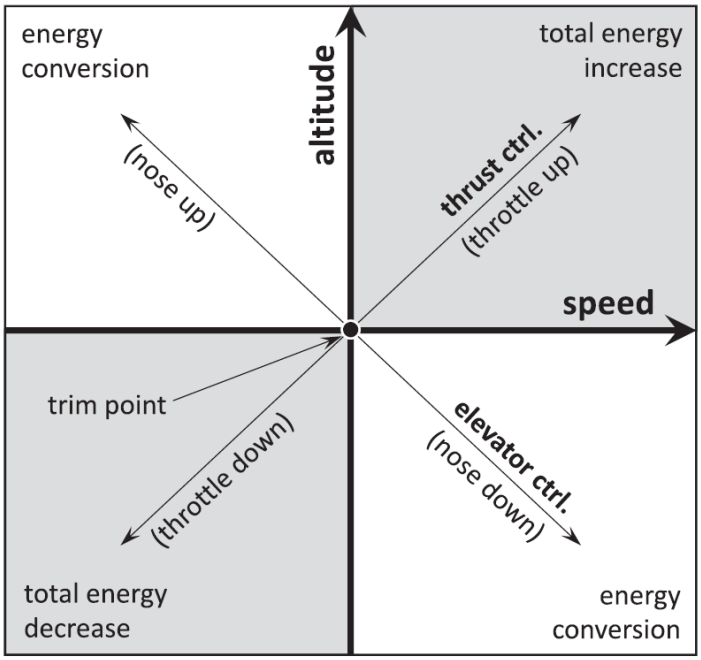

Figure 2.2: Energy increase, decrease and conversion using TECS. Source: [59].

In practice, the core functionality of TECS is implemented as a Proportinal-Integral (PI) controller in the form:

$$\frac{T_{des}}{m \cdot g} = K_{TI} \cdot \frac{1}{s}\left(e_\gamma + \frac{e_{\dot{V}}}{g}\right) - K_{TP} \cdot \left(\gamma + \frac{\dot{V}}{g}\right) \tag{2.90}$$

$$\theta_{des} = K_{EI} \cdot \frac{1}{s}\left(e_\gamma - \frac{e_{\dot{V}}}{g}\right) - K_{EP} \cdot \left(\gamma - \frac{\dot{V}}{g}\right) \tag{2.91}$$

where $e_\gamma = \gamma_{des} - \gamma, e_{\dot{V}} = \dot{V}_{des} - \dot{V}$ are the flight path angle and acceleration errors respectively. The desired accelerations and flight path angles are generated in an outer loop as simple proportional controllers:

$$\dot{V}_{des} = K_V \cdot (V_{a_{des}} - V_a) \tag{2.92}$$

$$\dot{h}_{des} = K_h \cdot (h_{des} - h) \tag{2.93}$$

$$\gamma_{des} = \frac{\dot{h}_{des}}{V} \tag{2.94}$$

and the desired thrust and θ are used respectively in PI with feed forward and Proportinal-Integral-Derivative (PID) inner loops to generate the throttle and elevator commands.

$$\delta_t = K_{thr} \cdot \left(\frac{T_{des}}{m \cdot g} - \frac{T}{m \cdot g}\right) + K_{i,thr} \cdot \frac{1}{s}\left(\frac{T_{des}}{m \cdot g} - \frac{T}{m \cdot g}\right) + K_{FF} \cdot \frac{m \cdot g}{T_{max}} \cdot \frac{T_{des}}{m \cdot g} \tag{2.95}$$

$$\delta_e = K_\theta \cdot (\theta_{des} - \theta) + K_{i,\theta} \cdot \frac{1}{s}(\theta_{des} - \theta) + K_q \cdot (-q) \tag{2.96}$$

where T_{max} is the maximum possible thrust the system is able to give, which means the component $\frac{m \cdot g}{T_{max}}$ serves a normalizing function over the feed forward term. Furthermore, while the thrust is generally not measured directly, for control in TECS it can be estimated using models such as those presented in Section 2.1.4.

Finally, some envelope protection measures must be taken to ensure the commands are limited to within the operational availability of the aircraft. First, the inputs must be limited with the conditions of minimum and maximum possible thrust:

$$\frac{-D}{m \cdot g} < \frac{\dot{V}_{des}}{g}, \gamma_{des} < \frac{T_{max} - D}{m \cdot g} \tag{2.97}$$

Second, their rates must also be limited to respect boundaries of maximum acceleration desired:

$$\frac{n_{min} g}{V} < \frac{\ddot{V}_{des}}{g}, \dot{\gamma}_{des} < \frac{n_{max} g}{V} \tag{2.98}$$

where $n_{min}g, n_{max}g$ are minimum and maximum acceleration limits.

Lastly, limits must be set to protect against stall and over-speed.

$$K_V \cdot (V_{min} - V_a) < \dot{V} < K_V \cdot (V_{max} - V_a) \tag{2.99}$$

The values of $n_{min}g, n_{max}g, V_{min}, V_{max}$ can depend on the aircraft and mission requirements. Furthermore, the first condition only limits the individual values, but not their sum; this, however, is dealt with by a priority logic inside of TECS which can tell when it's impossible to follow both commands and chooses only one to actually use.

In terms of values of the controller gains $K_{TI}, K_{EI}, K_{TP}, K_{EP}$, in order to achieve correct decoupling of the longitudinal and vertical controls, the proportional gains must be kept at 1 and the integral gains must have the same value [56].

2.4 Automatic Control System for Landing on Mobile Platforms

As explained in Section 1.1.5, landing UAVs on a ground vehicle in a cooperative way is a very novel concept. Here, an overview of the currently proposed strategy is given.

Figure 2.3 illustrates the six stages present in the cooperative landing procedure, as defined by Muskardin [11]:

1. Waypoint tracking
2. Initial descent
3. Final approach
4. Flare and touchdown
5. Ground lock and deceleration
6. Full stop

In waypoint tracking, the aircraft automatically follows a predetermined general path to begin the procedure. During this time, the Unmanned Ground Vehicle (UGV) is kept on standby.

During the initial descent, the aircraft slowly reduces its altitude in order to approach the maneuver start point, which is generally around $300m$ behind and $20m$ above the point where the ground vehicle is. Once more, the UGV remains on standby.

It is at the final approach stage that the cooperative maneuver starts. At this phase, the UGV starts to accelerate to match the speed of the aircraft, while the UAV descents closer to the ground. When they become sufficiently close, both vehicles start synchronizing their positions and velocities to each other in the horizontal plane.

The flare and touchdown stage begins when the UAV and UGV have achieved positional synchronization and the aircraft is flying at the desired landing airspeed only a few meters directly above the ground vehicle. The UAV must now slowly reduce its altitude further until touchdown on the platform on top the UGV is achieved. During this process, both vehicles must still act cooperatively to maintain their horizontal positions aligned and reject external disturbances (such as wind gusts). At a given altitude in this process, when the vehicles are close, the aircraft engine must be retarded in order to keep away from any accidental damage to either the engine or the platform.

After touchdown occurs, the aircraft gets locked to the landing platform in order to avoid any form of sudden relative movement which could cause it to slip away. At this point, the UGV takes center stage in the process and begins the deceleration of the joined vehicles.

Finally, once deceleration is done, both vehicles come together to a full stop and the maneuver is terminated.

Therefore, a cooperative control for the synchronization of the horizontal position of both UAV and UGV is necessary for stages 3 and 4. Muskardin [11] proposes two possibilities for this: a safety-based approach and a performance-based approach.

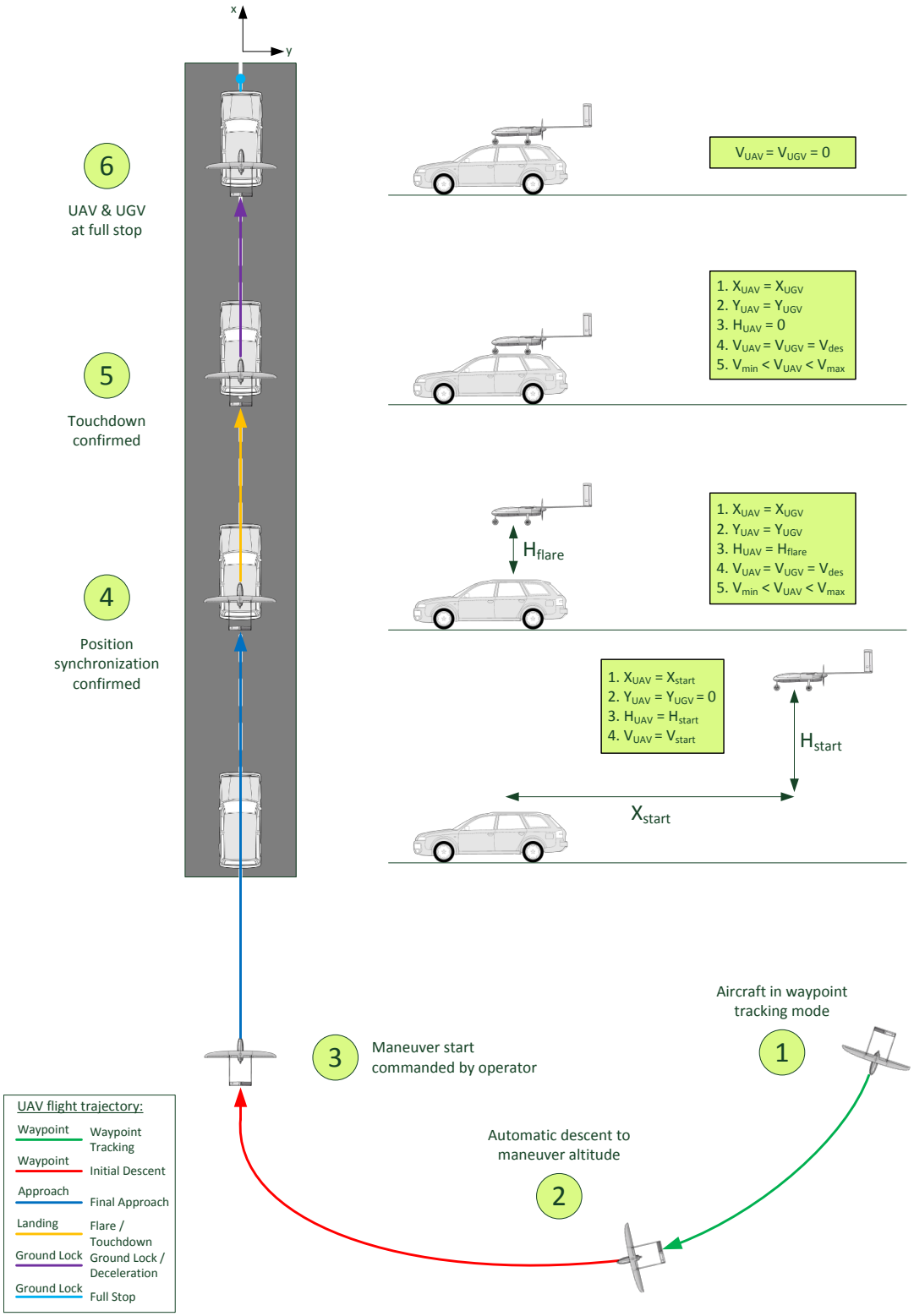

Figure 2.3: Phases of the cooperative landing maneuver. Source: [11].

2.4.1 Safety-Based Landing Control

As the name suggests, this is a conservative approach that is based on established landing procedures.

During the approach phase, the aircraft is commanded to glide at a constant flight path angle (determined as $\gamma = 3°$) and recommended landing airspeed, while also centralizing its position in relation to the UGV in the lateral direction. The UGV begins to increase its speed with a constant acceleration. When a given criteria is met (in Muskardin's work [11], the ground vehicle gets to a speed close enough to the UAV's groundspeed), the horizontal control is switched to a cooperative strategy, which remains active until touchdown.

In the flare phase, the desired flight path angle stops being constant to allow for a smoother landing. This is done following the procedure presented by Lambregts et al. [60]:

$$\dot{h}_{flare} = k \cdot (h + h_B) \tag{2.100}$$

where k and h_B are determined so $\dot{h}_{flare}(h_{flare}) = \dot{h}_{descent}$ and $\dot{h}_{flare}(0) = 0$; in other words, the transition between normal descent and flare descent is made smoothly, and touchdown is made at zero relative vertical velocity. Figure 2.4 illustrates the vertical control strategy during the final approach and flare.

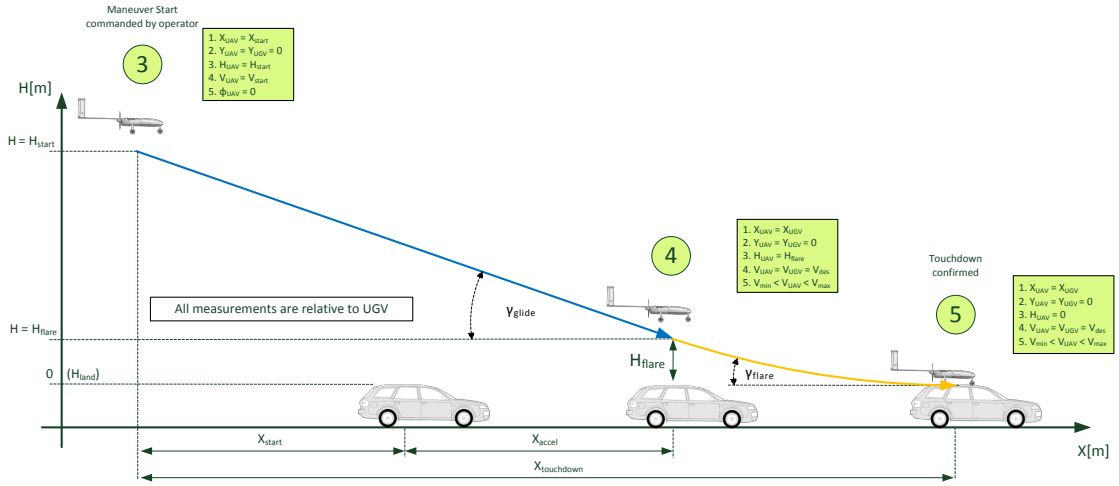

Figure 2.4: Lateral view of the final approach. Source: [11].

In terms of the cooperative horizontal control, the UAV synchronizes the lateral direction and the UGV synchronizes the longitudinal direction. This method of unilateral action from both vehicles was chosen because it results in an overall system stability which is independent of communication time delays [11].

Figures 2.5a and 2.5b show the cooperative control structure that is used in this approach. C_{XG}, C_{YA} are both PID controllers, the first being for longitudinal control of the UGV and the second for lateral control of the UAV. $G(s)$ represents the UGV

and $A(s)$ represents the UAV. The dashed line with a lateral controller for the ground vehicle C_{YG} is an optional term to align the UGV with the centerline of the runway.

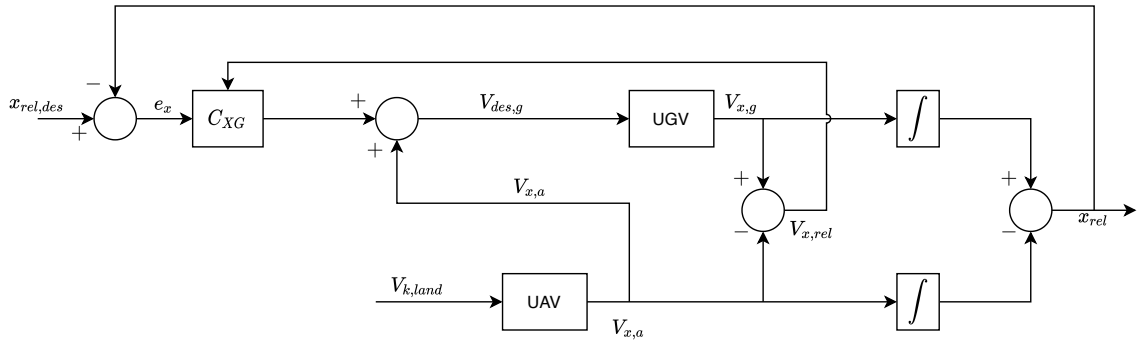

(a) Longitudinal control. Adapted from: [11; 61].

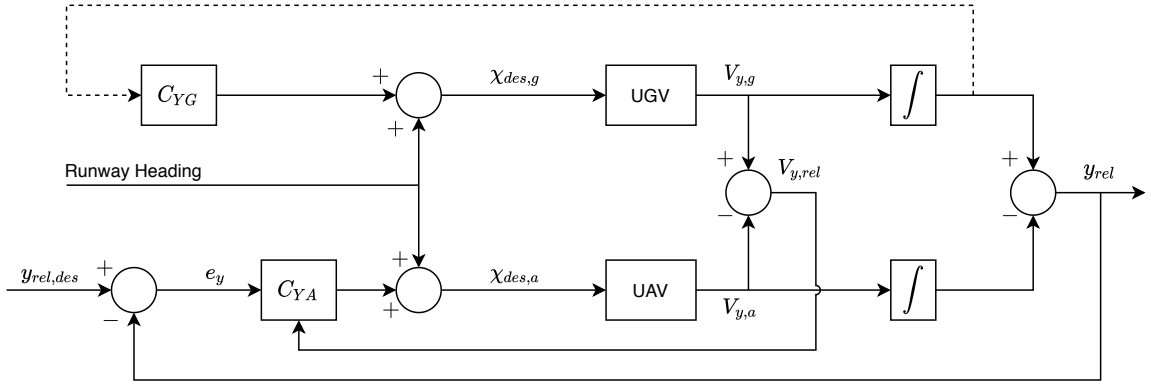

(b) Lateral control. Adapted from: [11; 61].

Figure 2.5: Structure of the safety-based cooperative horizontal synchronization control.

On the derivative part of the PID controllers, the signal is not mathematically derived; instead, the error in velocities is directly used. The controllers C_{XG} and C_{YA} have their inputs given in Cartesian coordinates $e_x, e_{v_x}, e_y, e_{v_y}$, and as such, their outputs are also Cartesian commands $V_{x_{des}}, V_{y_{des}}$. However, both UAV and UGV take commands in polar coordinates $V_{k_{des}}, \chi_{des}$. The conversion from one system to another is given by:

$$V_{k_{des}} = \sqrt{V_{x_{des}}^2 + V_{y_{des}}^2} \tag{2.101}$$

$$\chi_{des} = atan\left(\frac{V_{y_{des}}}{V_{x_{des}}}\right) \tag{2.102}$$

Finally, to ensure a fail-safe behavior, a finite state machine is used, which was developed by Muskardin et al. [28] and can be seen in Figure 2.6. Note all dimensions are relative to the UGV.

In the "low go-around to retry" state, the UAV is commanded back up to the flare height h_{flare} and both vehicles must synchronize their positions before the aircraft can

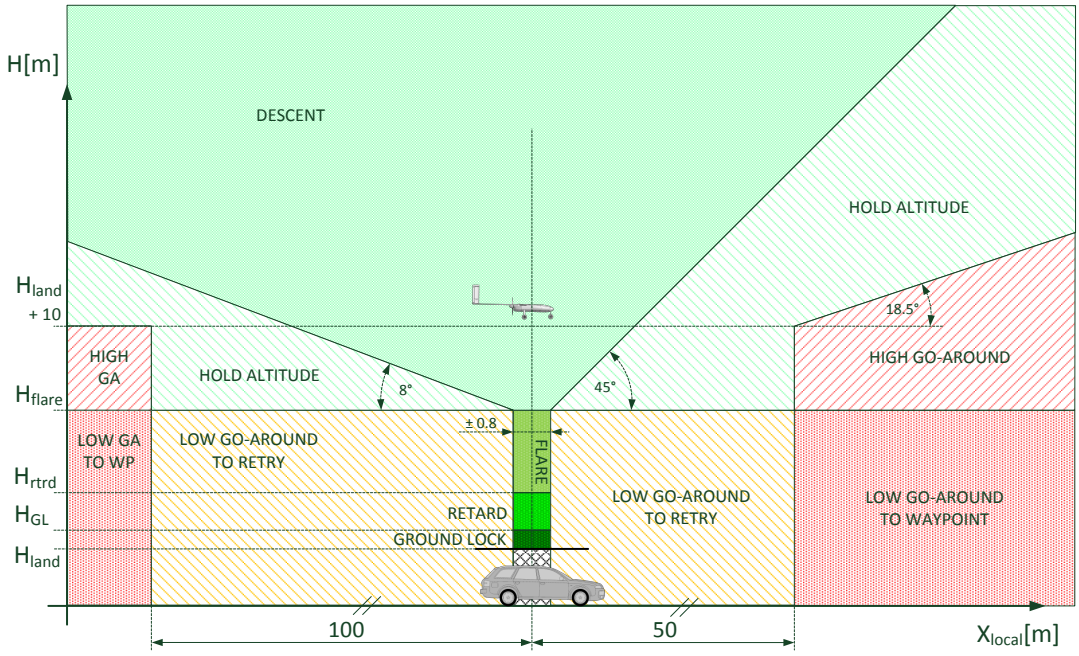

(a) Side view of the state machine's geometric constraints in longitudinal direction. Source: [11].

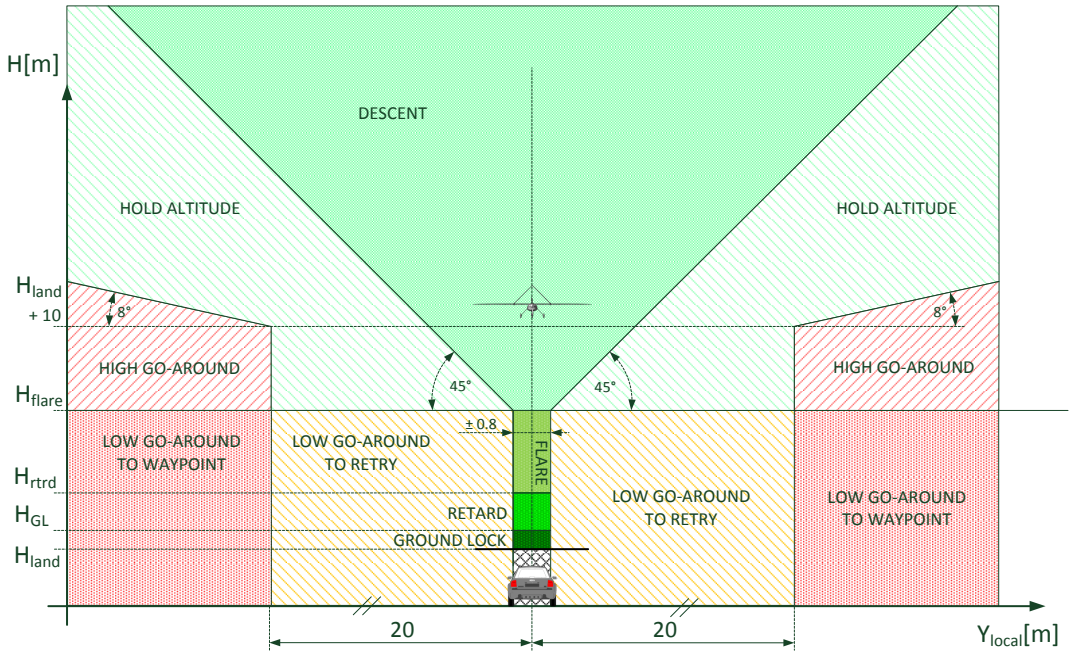

(b) Rear view of the state machine's geometric constraints in lateral direction. Source: [11].

Figure 2.6: State machine used for cooperative control. Source: [11].

attempt to descend again. In the “high go-around” and ”low go-around to waypoint” states, the maneuver is aborted and the aircraft is commanded back to waypoint tracking mode. Finally, in the “hold altitude” state, the approach of the UAV to the ground is suspended. In all other states, the landing proceeds normally as has been discussed before.

2.4.2 Performance-Based Landing Control

The performance-based approach was designed by Muskardin [11] to achieve two main goals: decrease the runway used during the landing procedure, and reject disturbances (such as wind gusts) during critical states as much as possible. In terms of what is carried over from the safety-based approach in the performance-based, the state machine is still present (only the “hold altitude” state is suppressed in favor of better performance, being substituted by “descent”), and the flight path angle control in the flare stage is also the same. The main differences, therefore, are the input generation of both vehicles during the final approach stage and the horizontal synchronization control in the flare stage.

2.4.2.1 Model Predictive Control

During the final approach, a MPC is utilized to calculate an optimized trajectory and generate optimal inputs $V_{k_{des}}, \chi_{des}$ to both UAV and UGV, as well as a γ_{des} command for the aircraft. This MPC strategy was first studied by Persson et al. [29], expanded by Pavani [30] and further investigated in Muskardin [11]. In the following, all equations are written in the local reference frame, and subscript $(\cdot)_a$ expresses the variable is related to the UAV while subscript $(\cdot)_g$ expresses the variable is related to the UGV.

Inside of the MPC the vehicles are modeled using a linear approach with first order system approximations.

$$\dot{x}_a = V_{k,a} \tag{2.103}$$

$$\dot{y}_a = \overline{V_K} \cdot \chi_a \tag{2.104}$$

$$\dot{V}_{k,a} = \frac{1}{\tau_{V,a}} \cdot (V_{k,a}^{des} - V_{k,a}) = a_a \tag{2.105}$$

$$\dot{\chi}_a = \frac{1}{\tau_{\chi,a}} \cdot (\chi_a^{des} - \chi_a) \tag{2.106}$$

$$\dot{h}_a = \overline{V_K} \cdot \gamma_a \tag{2.107}$$

$$\dot{\gamma}_a = \frac{1}{\tau_{\gamma,a}} \cdot (\gamma_a^{des} - \gamma_a) \tag{2.108}$$

$$\dot{x}_g = V_{k,g} \tag{2.109}$$
$$\dot{y}_g = \overline{V_K} \cdot \chi_g \tag{2.110}$$
$$\dot{V}_{k,g} = \frac{1}{\tau_{V,g}} \cdot (V_{k,g}^{des} - V_{k,g}) = a_g \tag{2.111}$$
$$\dot{\chi}_g = \frac{1}{\tau_{\chi,g}} \cdot (\chi_g^{des} - \chi_g) \tag{2.112}$$

where $\overline{V_K}$ is the landing maneuver trim velocity and $\tau_{V,a}, \tau_{\chi,a}, \tau_{\gamma,a}, \tau_{V,g}, \tau_{\chi,g}$ are the time constants of the closed-loop system response for commanded velocity, course angle and flight path angle.

The trajectory planning and input generation can then be formulated as an optimization problem, with states $s = [x_a, y_a, V_{k,a}, a_a, \chi_a, h_a, \gamma_a, x_g, y_g, V_{k,g}, a_g, \chi_g]^T$ and inputs $u = [V_{k,a}^{des}, \chi_a^{des}, V_{k,g}^{des}, \chi_g^{des}]^T$. Note the addition of accelerations a_a, a_g in the states: this is done so they can also be part of weight of the objective function and can be subjected to limitations imposed on the states. On the subject of problem formulation, the optimization is verily done in a decoupled manner: first the horizontal part of the optimization is done, and its predicted states are then used in the vertical optimization. Once both are concluded, the optimal control inputs from both are fed to the vehicle controllers.

Additionally, supplementary geometrical constraints are defined for the MPC to ensure safe operation. To avoid positions that could be considered dangerous, slack zones are introduced, which are zones that add to the cost function upon entrance, making them unfavorable from an optimization standpoint. Figure 2.7 illustrates how these zones are defined. Finally, terminal weights are also used, which are terms inserted to minimize the final value of select variables.

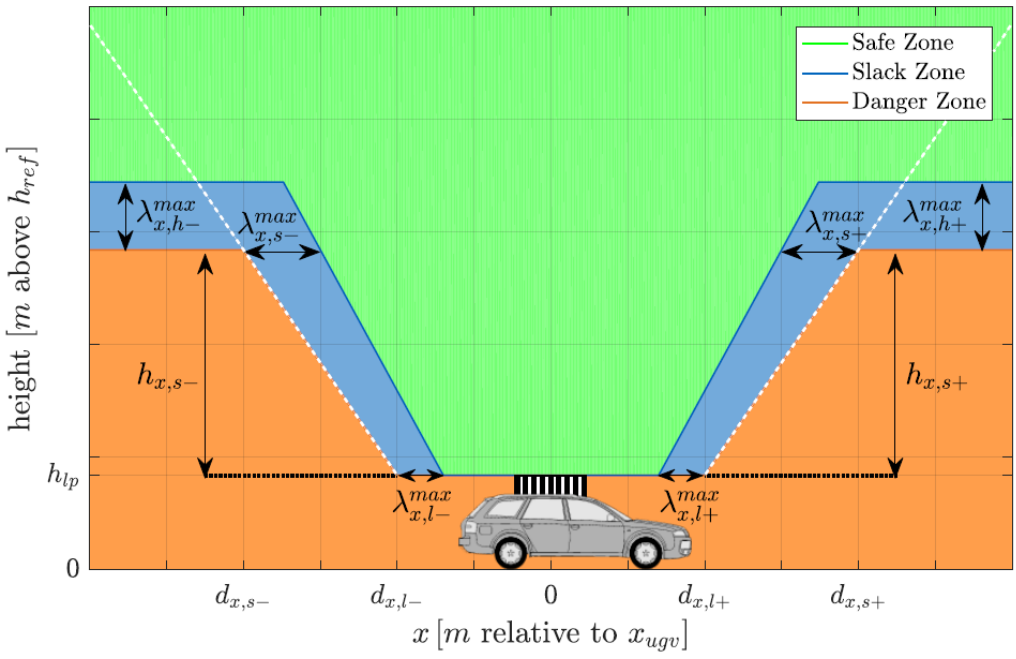

Figure 2.7: Geometrical constraints of the MPC. Source: [30].

Horizontal Optimization

In summary, the MPC's horizontal objective function can be written as:

$$J_{xy} = \lambda_{xy}^T \cdot L_{xy} \cdot \lambda_{xy} + \varepsilon^T \cdot P_{xy} \cdot \varepsilon + u_{xy}^T \cdot Q_{xy} \cdot u_{xy} + \dot{u}_{xy}^T \cdot R_{xy} \cdot \dot{u}_{xy} + s_{xy,end}^T \cdot W_{xy} \cdot s_{xy,end} \quad (2.113)$$

where:

- λ_{xy} is the slack variables vector.
- L_{xy} is the slack weighting matrix.
- ε is the state error vector.
- P_{xy} is the error weighting matrix.
- u_{xy} is the input vector.
- Q_{xy} is the input weighting matrix.
- $\dot{u}_{xy}$ is the input derivative vector.
- R_{xy} is the input derivative weighting matrix.
- $s_{xy,end}$ is the terminal state vector.
- W_{xy} is the terminal weighting matrix.

The state, input and state error vectors for the horizontal plane are defined as:

$$s_{xy} = \begin{bmatrix} x_a \\ y_a \\ V_{k,a} \\ a_a \\ \chi_a \\ x_g \\ y_g \\ V_{k,g} \\ a_g \\ \chi_g \end{bmatrix} \qquad u = \begin{bmatrix} V_{k,a}^{des} \\ \chi_a^{des} \\ V_{k,g}^{des} \\ \chi_g^{des} \end{bmatrix} \qquad \varepsilon = \begin{bmatrix} x_g - x_a \\ y_g - y_a \\ V_{k,g} - V_{k,a} \\ a_g - a_a \\ \chi_g - \chi_a \end{bmatrix} \quad (2.114)$$

The matrices P_{xy}, Q_{xy}, R_{xy} are diagonal matrices:

$$P_{xy} = \begin{bmatrix} p_x & 0 & 0 & 0 & 0 \\ 0 & p_y & 0 & 0 & 0 \\ 0 & 0 & p_{V_k} & 0 & 0 \\ 0 & 0 & 0 & p_a & 0 \\ 0 & 0 & 0 & 0 & p_\chi \end{bmatrix} \quad Q_{xy} = \begin{bmatrix} q_{V,a} & 0 & 0 & 0 \\ 0 & q_{\chi,a} & 0 & 0 \\ 0 & 0 & q_{V,g} & 0 \\ 0 & 0 & 0 & q_{chi,g} \end{bmatrix} \quad R_{xy} = \begin{bmatrix} r_{V,a} & 0 & 0 & 0 \\ 0 & r_{\chi,a} & 0 & 0 \\ 0 & 0 & r_{V,g} & 0 \\ 0 & 0 & 0 & r_{chi,g} \end{bmatrix} \quad (2.115)$$

While Q_{xy} and R_{xy} both have constant entries, P_{xy} does not. Adaptive weights are used for state alignment in the horizontal plane, which are weights that have their values changed depending on the value of the states themselves. This is done to mitigate any possible dependency of the total cost contribution of each entry on the initial conditions. In its case, each weight p is updated at each call of the MPC, which was designed as follows:

$$p_i = p_i^k + p_i^l \cdot |i_g^0 - i_a^0| \qquad \forall i \in x, y, V_k, a, \chi \tag{2.116}$$

where p^k represents a constant weight contribution, p^l represents a linear weight contribution, and the 0 superscript indicates the value considered is the one at the beginning of the iteration call. According to Muskardin [11], adding these adaptive terms "has proven to be very beneficial in terms of system robustness and overall performance".

The terminal weighting matrix only has two non-zero entries, which relate to the end states of x_g and y_g. These two are chosen since the first represents the amount of runway used to succeed on touchdown, which is an important metric to minimize, and the second expresses the distance to the centerline of the runway, which should be kept minimal for safety.

$$W_{xy} = \begin{bmatrix} 0 & 0 & 0 & 0 & 0 & 0 & 0 & 0 & 0 & 0 \\ 0 & 0 & 0 & 0 & 0 & 0 & 0 & 0 & 0 & 0 \\ 0 & 0 & 0 & 0 & 0 & 0 & 0 & 0 & 0 & 0 \\ 0 & 0 & 0 & 0 & 0 & 0 & 0 & 0 & 0 & 0 \\ 0 & 0 & 0 & 0 & 0 & 0 & 0 & 0 & 0 & 0 \\ 0 & 0 & 0 & 0 & 0 & w_{x,g} & 0 & 0 & 0 & 0 \\ 0 & 0 & 0 & 0 & 0 & 0 & w_{y,g} & 0 & 0 & 0 \\ 0 & 0 & 0 & 0 & 0 & 0 & 0 & 0 & 0 & 0 \\ 0 & 0 & 0 & 0 & 0 & 0 & 0 & 0 & 0 & 0 \\ 0 & 0 & 0 & 0 & 0 & 0 & 0 & 0 & 0 & 0 \end{bmatrix} \tag{2.117}$$

The state vector is constrained by the conditions $s_{xy}^{min} - \lambda_{xy} \leq s_{xy} \leq s_{xy}^{max} + \lambda_{xy}$, where s_{xy}^{min} and s_{xy}^{max} are determined appropriately as minimum and maximum allow values for each state. Similarly, the input vector is also constrained by minimum and maximum values $u_{xy}^{min} \leq u_{xy} \leq u_{xy}^{max}$. Finally, the terminal constraint is defined as $\varepsilon_{end} = 0$.

Vertical Optimization

Likewise, the MPC's vertical objective function can be written as:

$$J_z = \lambda_z^T \cdot L_z \cdot \lambda_z + p_h \cdot [h_a - h_{lp}]^2 \cdot b_h^* + p_\gamma \cdot \gamma_a^2 \cdot b_{xy}^* + Q_z \cdot u_z^2 + \cdot R_z \cdot \dot{u}_z^2 \tag{2.118}$$

where:

- λ_z is the slack variables vector.
- L_z is the slack weighting matrix.

- p_h is the weighting factor of altitude.
- h_{lp} is the landing platform altitude.
- b_h^* is a binary variable, whose value is only 1 if the aircraft is within the region considered safe to vertically approach the UGV.
- p_γ is the weighting factor of the flight path angle.
- b_z^* whose value is only 1 when b_h^* is zero.
- u_z is the input value γ_a^{des}.
- Q_z is the input weighting factor.
- $\dot{u}_z$ is the input derivative $\dot{\gamma_a^{des}}$.
- R_z is the input derivative weighting factor.

States h_a and γ_a are constrained by $h_a^{min} \leq h_a \leq h_a^{max}$ and $\gamma_a^{min} - \lambda_\gamma \leq \gamma_a \leq \gamma_a^{max} + \lambda_\gamma$. For more details on the implementation of the MPC, the interested reader is referred to Pavani [30] and Muskardin [11]. The MPC is switched off when the aircraft arrives at the flare state, and a horizontal cooperative control is used from there. This is done since the MPC inputs requires relatively speaking extensive time to compute, and that may cause problems when it is necessary to quickly react to disturbances once the aircraft and ground vehicle are already very close to each other.

2.4.2.2 Horizontal Synchronization Control

When it comes to the horizontal cooperative control in the flare condition, both vehicles synchronize both directions, which is done to maximize the amount of disturbance the system can reject. Since this is a bilateral approach, concerns can be raised about the stability dependency of the system in regard to the communication time delay; Muskardin et al. [59] have suggested the use of a Time Domain Passivity Control Approach (TDPA) in cases the delay becomes too high to mitigate this shortcoming and stabilize the system, but that lies beyond the scope of this work. Figures 2.8a and 2.8b show the cooperative control structure that is used in this approach.

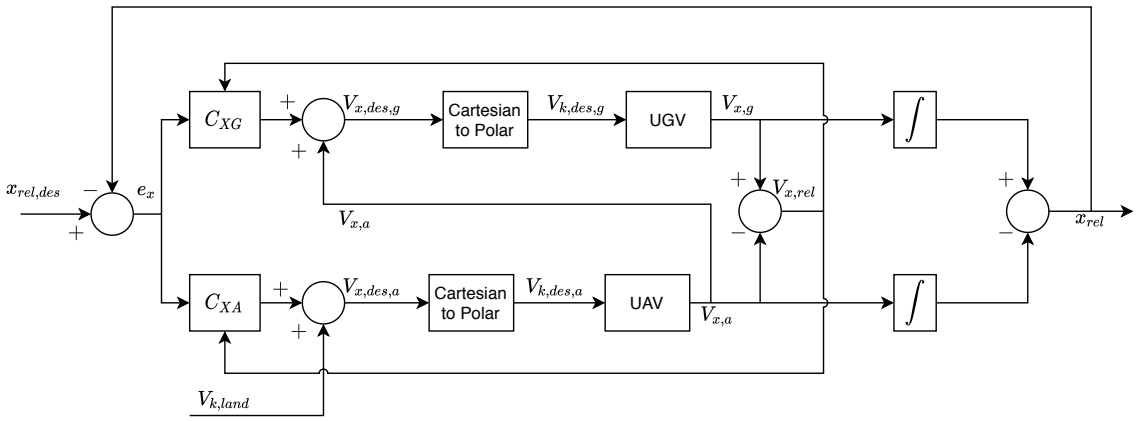

(a) Longitudinal control. Adapted from: [11; 61].

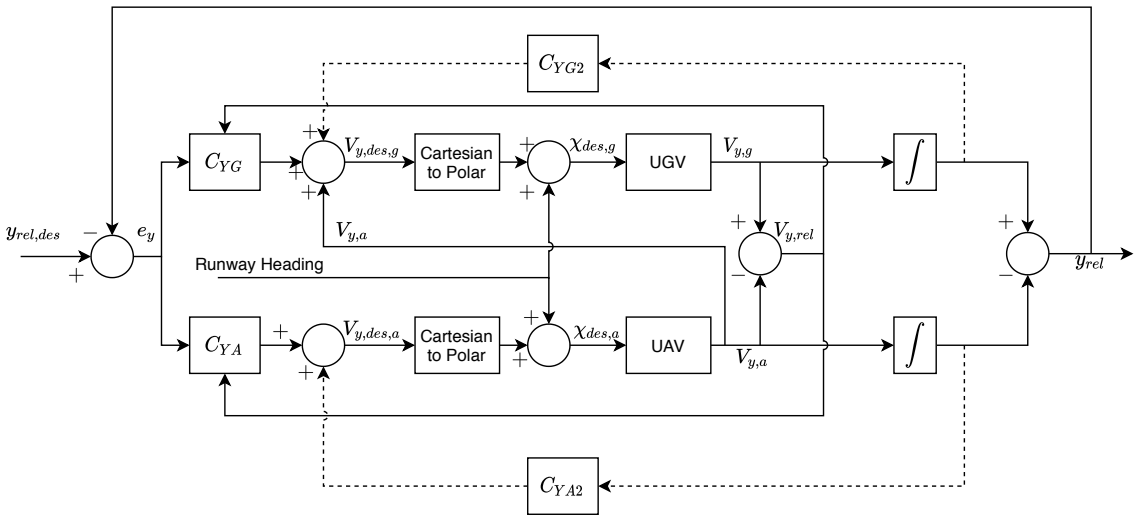

(b) Lateral control. Adapted from: [11; 61].

Figure 2.8: Structure of the performance-based cooperative horizontal synchronization control.

2.5 Time Domain Design for Controller Tuning

There are many methods available in the control literature for tuning the controller gains of a system. An interested reader in the subject in general is referred to Skogestad [62], Ogata [63], Astrom [64], Dorf [65], among others. Here, we focus on the use of time domain methods through the means of numerical optimization, which one can also find out more about in the aforementioned works.

Essentially, a nonlinear constrained numerical optimization scheme can be setup with the controller gain values as design variables. The system is then forced to respond to some external input (which can include a change in setpoint, an injected disturbance, or some other variation), and the response is saved and evaluated according to different metrics. These criteria include:

- Integral of Absolute Error (IAE): $\int_0^\infty |e| dt$.
- Integral of Time-weighted Absolute Error (ITAE): $\int_0^\infty t \cdot |e| dt$.
- Integral of Squared Error (ISE): $\int_0^\infty e^2 dt$.
- Integral of Time-weighted Squared Error (ITSE): $\int_0^\infty t \cdot e^2 dt$.
- Maximum control derivative: $max|\dot{u}|$.
- Integral Squared of Controller Action (ISCA): $\int_0^\infty u^2 dt$.
- Integral Squared of Controller Derivative (ISCD): $\int_0^\infty \dot{u}^2 dt$.
- Overshoot: O "the maximum peak value of the response curve measured from the desired response of the system" [63].
- Settling time: T_s time required for the response of the system to remain bounded by a certain criteria related to its final value (generally 2% or 5% of its value).

- Rise time: T_r time required for the response to go from 10% to 90% of its final value.

As objective function, a linear function with the selected criteria can be used, where each coefficient is the weight given to the respective metric. Finally, an optimization algorithm is chosen; one possibility is the use of the Nelder-Mead method [66]. With this, once the lower and upper limit values of each gain are given, the problem formulation is complete and, at the end, the optimization should result in optimal controller gain values. Which criteria to choose and which weights to assign to them is an exercise that wholly depends on the application.

System Identification of Penguin BE UAV, Elektra 1 Solar and Elektra 2 Solar

3.1 Previous Work

In this section, the previous results in system identification of the Penguin BE UAV, Elektra 1 Solar and Elektra 2 Solar will be summarized. In the data gathering of these aircraft, only maneuvers related to the longitudinal and vertical dynamics were made, namely elevator pulse (for phugoid excitation), elevator 3-2-1-1 (for short period excitation) and throttle doublet (for thrust variation dynamics), and therefore, while the lateral dynamics will be considered in the flight reconstruction step, they will not be taken into consideration when formulating the model structure and finding the derivative coefficients.

3.1.1 Penguin BE

For Penguin BE, a total of 15 maneuvers were performed, which are separated in 5 phugoid, 5 short period, and 5 thrust variations. In both the works of Lee [15] and Coelho [21], after the data underwent a detailed analysis, 6 of those were selected as part of the identification set, 2 of each type, and for the validation set, 3 others were chosen, one of each type.

Lee [15] used the Two Step Method, with a KF approach to the data compatibility check. Table 3.1 shows the identified aerodynamic and propulsion derivatives, while Tables 3.2 and 3.3 showing the model validation of forces and states.

Term	Value	Term	Value	Term	Value
X_0	9.2587	Z_0	-45.44	M_0	-2.1589
X_u	-2.2797	Z_u	-4.74	M_u	0.0928
X_w	1.3422	Z_w	-9.04	M_w	-0.5579
X_q	-1.3519	Z_q	-88.21	M_q	-6.8804
$X_{\delta e}$	27.3732	$Z_{\delta e}$	333.88	$M_{\delta e}$	-48.9397
$X_{\delta t}$	51.4792				

Table 3.1: Penguin BE aerodynamic derivatives from Lee [15].

	Identification Set			**Validation Set**		
Coefficient	X	Z	M	X	Z	M
R^2	0.868	0.616	0.422	0.848	0.665	0.1359
$RMSE$	3.109	19.779	1.0899	4.10	20.83	1.239
$NRMSE$	0.071	0.067	0.045	0.078	0.067	0.053

Table 3.2: Averaged statistical measures for the forces and moment in model validation of Penguin BE from Lee [15].

	Identification Set				**Validation Set**			
Coefficient	u	w	q	θ	u	w	q	θ
GOF	0.77	0.72	0.514	0.688	0.76	0.52	0.52	0.72
TIC	0.03	0.28	0.355	0.254	0.038	0.453	0.345	0.236

Table 3.3: Averaged statistical measures for the states in model validation of Penguin BE from Lee [15].

Coelho [21], on the other hand, compared different methods for the identification of Penguin BE, and ultimately concluded the OEM method yielded slightly better results than the Two Step Method, pointing out the difference may be the inclusion of the additional engine dynamics used in OEM. Table 3.4 shows the aerodynamic derivatives from the Two Step Method, while Tables 3.5 and 3.6 showing the model validation of forces and states. Finally, Table 3.7 shows the model validation of states using OEM, with the inclusion of motor engine angular velocity ω.

Term	**Value**	**Term**	**Value**	**Term**	**Value**
X_0	24.8912	Z_0	-60.0449	M_0	-1.6648
X_u	-1.9521	Z_u	-4.2001	M_u	0.06910
X_w	1.9181	Z_w	-10.8758	M_w	-0.4797
X_q	-1.5002	Z_q	-170.2218	M_q	-7.4845
$X_{\delta e}$	-22.0493	$Z_{\delta e}$	28.5036	$M_{\delta e}$	-55.9172
$X_{\delta t}$	44.7413				

Table 3.4: Penguin BE aerodynamic derivatives from the Two Step Method from Coelho [21].

In all cases, however, some values of TIC remain above the recommended 0.3 threshold.

	Identification Set			**Validation Set**		
Coefficient	X	Z	M	X	Z	M
R^2	0.7609	0.6232	0.4831	0.7524	0.6593	0.03696
$RMSE$	4.5079	20.3579	0.9393	4.6814	22.2496	1.2930
$NRMSE$	0.08668	0.06067	0.04044	0.09414	0.06072	0.05926

Table 3.5: Averaged statistical measures for the forces and moment in model validation of Penguin BE from the Two Step Method from Coelho [21].

	Identification Set				**Validation Set**			
Coefficient	u	w	q	θ	u	w	q	θ
GOF	0.3680	0.1027	0.5069	0.3745	0.5330	-1.0559	0.4331	0.3207
TIC	0.04729	0.3101	0.3423	0.3437	0.05612	0.3979	0.3833	0.3688

Table 3.6: Averaged statistical measures for the states in model validation of Penguin BE from the Two Step Method from Coelho [21].

	Identification Set					**Validation Set**				
Coefficient	u	w	q	θ	ω	u	w	q	θ	ω
GOF	0.6604	0.3876	0.7225	0.7669	0.9363	0.7366	-0.4452	0.6843	0.5399	0.9156
TIC	0.0347	0.2737	0.2861	0.2222	0.0102	0.0424	0.3514	0.3080	0.2879	0.0152

Table 3.7: Averaged statistical measures for the states in model validation of Penguin BE from the Output Error Method from Coelho [21].

3.1.2 Elektra 1 Solar

For Elektra 1 Solar, a total of 9 maneuvers were performed, which were separated in 3 phugoid, 3 short period and 4 thrust variations. However, as seen in Lee [15], of those only 2 phugoid maneuvers were considered adequate for the identification process, with one serving as the identification set and the other as the validation set. In his work, Lee used the Two Step Method with different types of KF for flight path reconstruction, while also attempting two different model structures, a linear one and a nonlinear one, shown in equations 2.77 to 2.79. Tables 3.8 to 3.10 show the results of linear identification and validation, and Tables 3.11 to 3.13 show the results of nonlinear identification and validation.

Overall, the performance metrics demonstrated are all within the established threshold, but no significant difference is seen between the linear and nonlinear models.

Term	Value	Term	Value	Term	Value
X_0	848.6782	Z_0	-3468.6	M_0	-335.9959
X_u	-82.5606	Z_u	-12.6203	M_u	13.2402
X_w	8.3085	Z_w	-91.5232	M_w	-1.5825
X_q	2808.8	Z_q	-10522	M_q	-1081.8
$X_{\delta e}$	4818.9	$Z_{\delta e}$	-14559	$M_{\delta e}$	-4073.2
$X_{\delta t}$	1200.4				

Table 3.8: Elektra 1 Solar linear aerodynamic derivatives from Lee [15].

	Identification Set			Validation Set		
Coefficient	X	Z	M	X	Z	M
R^2	0.69	0.79	0.30	0.65	0.77	0.29
$RMSE$	41.89	153.7	15.89	49.15	178.5	19.29
$NRMSE$	0.065	0.042	0.041	0.063	0.043	0.039

Table 3.9: Averaged statistical measures for the forces and moment in linear model validation of Elektra 1 Solar from Lee [15].

	Identification Set				Validation Set			
Coefficient	u	w	q	θ	u	w	q	θ
GOF	0.9037	0.5856	0.8959	0.9323	0.7156	0.5119	0.8765	0.8981
TIC	0.0094	0.2154	0.1660	0.0971	0.1872	0.2626	0.1753	0.1239

Table 3.10: Averaged statistical measures for the states in linear model validation of Elektra 1 Solar from Lee [15].

Term	Value	Term	Value	Term	Value
X_0	909.5517	Z_0	-3886.4	M_0	-338.7066
X_u	-85.4185	Z_u	22.9396	M_u	12.5911
X_w	-121.5265	Z_w	279.3562	M_w	28.2114
X_q	3059.3	Z_q	-11500	M_q	-1115.9
$X_{\delta e}$	7151	$Z_{\delta e}$	-23309	$M_{\delta e}$	-4526.1
$X_{\delta t}$	1298.2				
X_{wq}	-443.7352	Z_{wq}	583.6403	M_{wq}	133.1528
$X_{w\delta e}$	-5143.2	$Z_{w\delta e}$	15717	$M_{w\delta e}$	1168.7
X_{w^2}	-18.9805	Z_{w^2}	-52.707	M_{w^2}	3.069

Table 3.11: Elektra 1 Solar nonlinear aerodynamic derivatives from Lee [15].

	Identification Set			**Validation Set**		
Coefficient	X	Z	M	X	Z	M
R^2	0.921	0.937	0.443	0.847	0.883	0.418
$RMSE$	21.01	82.56	14.11	32.44	127.1	17.32
$NRMSE$	0.027	0.020	0.0292	0.042	0.031	0.036

Table 3.12: Averaged statistical measures for the forces and moment in nonlinear model validation of Elektra 1 Solar from Lee [15].

	Identification Set				**Validation Set**			
Coefficient	u	w	q	θ	u	w	q	θ
GOF	0.8821	0.5789	0.8834	0.9279	0.8569	0.5576	0.8507	0.9061
TIC	0.0104	0.2390	0.1764	0.1023	0.0133	0.2201	0.1985	0.1289

Table 3.13: Averaged statistical measures for the states in nonlinear model validation of Elektra 1 Solar from Lee [15].

3.1.3 Elektra 2 Solar

For Elektra 2 Solar, a total of 30 maneuvers were performed, out of which 7 phugoid excitation maneuvers were selected for system identification by Kalra [23]. In her work, Kalra used the Two Step Method, with the data compatibility check being done by OEM. The identified derivatives are shown in Table 3.14, while Table 3.15 shows the model validation of states.

Term	**Value**	**Term**	**Value**	**Term**	**Value**
X_0	-7030.2	Z_0	-3892.3	M_0	-236.91
X_u	-48.16	Z_u	-34.84	M_u	6.995
X_w	5.74	Z_w	-0.0014	M_w	-2.017
X_q	-114.7	Z_q	-8070.2	M_q	-654.74
$X_{\delta e}$	-448.5	$Z_{\delta e}$	-0.0179	$M_{\delta e}$	-2685
$X_{\delta t}$	12323.8				

Table 3.14: Elektra 2 Solar linear aerodynamic derivatives from Kalra [23].

As can be seen, the results shown do not meet the required threshold set of $TIC < 0.3$. Kalra pinpoints this relative poor results are due to the quality of the flight data used in the identification process, which contained considerable drift [23].

	Identification Set				Validation Set			
Coefficient	u	w	q	θ	u	w	q	θ
GOF	-1.556	-60.634	-0.07206	-1.659	-1.648	-55.276	-0.00679	-2.4185
TIC	0.0984	0.8099	0.3746	0.3372	0.0936	0.764	0.3708	0.3564

Table 3.15: Averaged statistical measures for the states in linear model validation of Elektra 2 Solar from Kalra [23].

3.2 Proposed Changes

A couple of improvements can be made to the system identification process using the Two Step Method as it is being currently done.

First, the terms related to throttle and thrust are a constant source of errors. Coelho [21] points out that, by not including engine dynamics in the process, throttle variations are immediately reflected upon in the forces, which is not what is observed in real experiments due to the inertia of the engine and propeller causing a delay in the acceleration of the engine speed and consequential increase in thrust force, and that can cause a severe mismatch in the modeling. Furthermore, Lee [15] observes that the relation between throttle and thrust may not be linear, and large variations in throttle, such as those which are part of the throttle doublet maneuver, should cause nonlinear force disturbances, which cannot be reflected with only a linear term. Indeed, by using the available logdata from TECS where thrust forces are estimated, a relation between throttle and estimated thrust for Elektra 2 Solar can be made as an example, which is shown in Figure 3.1. As can be seen, this is a case where the relation is at least cubic in nature, and a linear term would not suffice to model it adequately. Finally, by only considering a linear term in the longitudinal direction, the possible influence of the thrust force in pitch dynamics mentioned in Section 2.1.4 is overlooked.

Considering these numerous issues, and that propulsion models for the relevant aircraft have been internally developed and validated, the choice made in this work is to use those instead of trying to directly identify any related terms. As such, the throttle doublet maneuvers from Penguin BE will be discarded, and the $X_{\delta t}$ term will be removed from the model structure in general. Instead, in the identification process, the propulsion force and moments will be calculated using the aforementioned model and subtracted from the estimated force and moments, so that only the aerodynamic effects of the aircraft are identified.

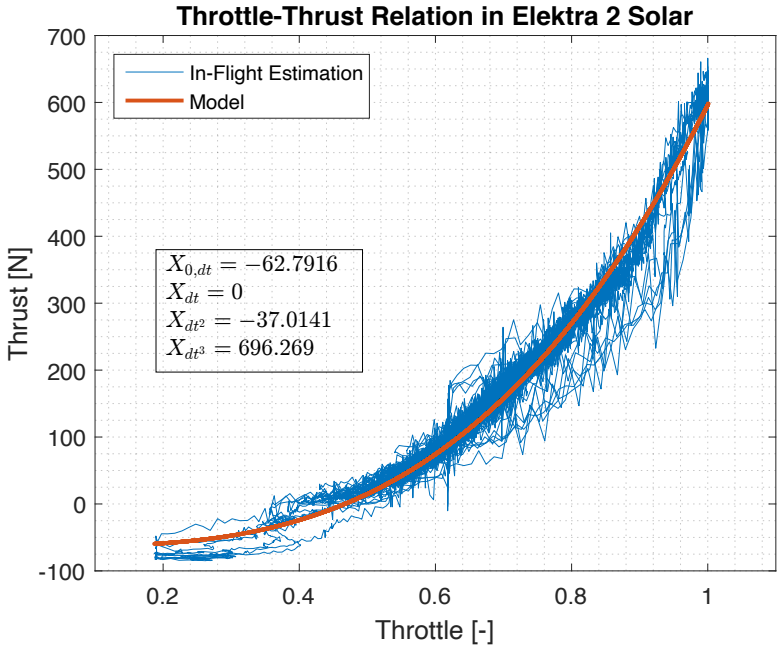

Figure 3.1: Relation between throttle and thrust using flight logdata from Elektra 2 Solar.

Another general change introduced here is the attempt to reduce model parameters, instead of increasing them. Ockham's Razor, or the principle of simplicity, is used to define what constitutes a "best model" for an application, and, in translation, that principles reads as: "The number of entities should not be increased beyond what is necessary to explain anything" [67]. As explained in Jategaonkar [19], in the case of system identification, "entities" are the hypothesis assumed and the parameters introduced for the creation of the model. Therefore, a study will be carried out to find what the minimum number of parameters for system identification of aircraft is.

For the identification of Elektra 1 Solar in particular, the discarded phugoid from the realized identification maneuvers will be added to the identification set. Lee [15] originally dropped this because the maneuver was cut short, being stopped in its middle, but adding it to the process has provided better results overall, probably because only having one maneuver for identification is too restrictive.

Finally, for the identification of Elektra 2 Solar, data from different IMUs will be used. In particular, among all the available ones, two were chosen for this process, for containing less noise and drift than the others and having overall a good agreement (an estimated 10% average difference across states, accelerations, and rates). The identification process will be done three times: once with the data from each IMU independently, and a third time with an average of the data from both. This will allow for an investigation of the consistency of the model structure chosen, where it is expected that, with similar data, the final identified parameters are also similar among them. Lastly, for the longitudinal velocity u, data from a sensor attached to the aircraft with estimation methods from Balmer [68] will be used instead of GPS data.

3.3 Methodology

For the identification of all the models in the following, the Two Step Method will be used, due to its flexibility in changing the model structure, which is a very important benefit when one of the goals is finding a minimal set of parameters. For the data compatibility check, OEM will be used to determine biases in accelerations and rates, due to lack of information on noise statistics and normal sensor biases of Elektra 2 Solar especially.

On the subject of finding minimal parameters, for this step, identifications of Penguin BE and Elektra 1 Solar will be used. Both these aircraft have shown good results before, and serve as an excellent comparison. For the criteria, a model will be considered adequate when it fulfills the $TIC < 0.3$ threshold suggested by Jategaonkar [19] for all states (so, in this case of longitudinal identification, longitudinal velocity u, vertical velocity w, pitch rate q and pitch angle θ). This will be done through extensive analysis of the identification process. In terms of order of testing and priority of the considered terms, again Ockham's Razor is used, and for simplicity the order will follow Pascal's expansion for polynomials, in other words, first will come constant terms, then linear terms, then cross-products of linear terms, then quadratic terms, and so on.

Once a minimal set of parameters has been found, the identification process will then be applied for Elektra 2 Solar. Data from two different IMUs will be used, hereby referred to as IMU 1 and IMU 2. The identification with IMU 1 and IMU 2 will be done independently, as well as an identification with data averaged from the both IMUs. Relative differences from IMUs 1 and 2 will be analyzed, and parameters from the averaged set will be checked to see if they remain inside the "boundaries" determined by the two original sets. Finally, the model response from the three identification processes will be checked against the FAA's standards of high fidelity, shown in Table 2.2.

3.4 Results

3.4.1 Identification of Penguin BE and Elektra 1 Solar

After extensive investigation, it was concluded the minimal set of parameters for system identification are those shown in equations 3.1 to 3.3.

$$X = X_0 + X_u \cdot u + X_w \cdot w \tag{3.1}$$
$$Z = Z_0 + Z_u \cdot u + Z_w \cdot w + Z_q \cdot q \tag{3.2}$$
$$M = M_0 + M_u \cdot u + M_w \cdot w + M_q \cdot q + M_{\delta e} \cdot \delta e \tag{3.3}$$

In other words, the minimal system is a linear model, which also removes the terms X_q, $X_{\delta e}$ and $Z_{\delta e}$. The results of the identification process using these equations for Penguin BE and Elektra 1 Solar are shown in Figures 3.2 and 3.3 respectively, while Tables 3.16 and 3.18 show the identified parameters and Tables 3.17 and 3.19 show the statistical measures.

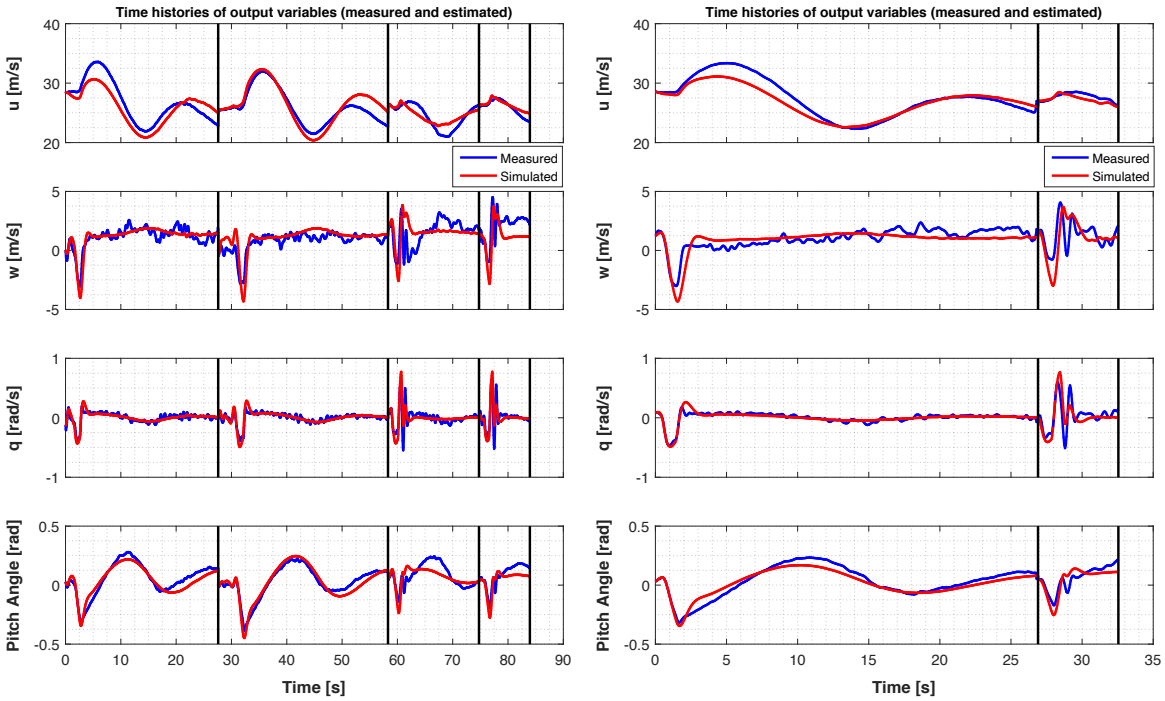

(a) Identification set. **(b)** Validation set.

Figure 3.2: Model validation of Penguin BE with minimal set of parameters using a forward simulation.

Term	Value	Term	Value	Term	Value
X_0	44.9263	Z_0	-17.0724	M_0	-0.2073
X_u	-2.3195	Z_u	-5.3911	M_u	0.0444
X_w	2.8826	Z_w	-17.4668	M_w	-0.7559
		Z_q	-151.9211	M_q	-7.7350
				$M_{\delta e}$	-59.7098

Table 3.16: Penguin BE aerodynamic derivatives with minimal set of parameters.

	Identification Set				Validation Set			
Coefficient	u	w	q	θ	u	w	q	θ
GOF	0.7638	0.3395	0.6394	0.8250	0.8391	0.2478	0.6647	0.8607
TIC	0.0275	0.2716	0.2865	0.1998	0.0215	0.2830	0.2811	0.1956

Table 3.17: Averaged statistical measures for the states in model validation of Penguin BE with minimal set of parameters.

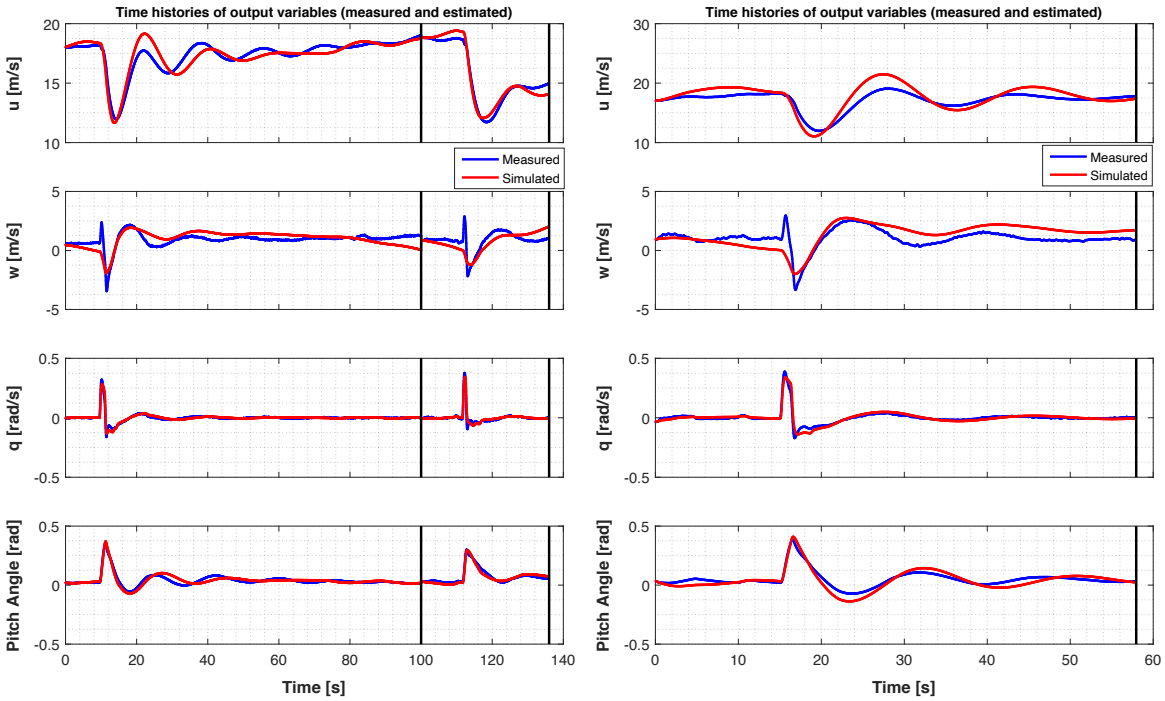

(a) Identification set. **(b)** Validation set.

Figure 3.3: Model validation of Elektra 1 Solar with minimal set of parameters using a forward simulation.

Term	Value	Term	Value	Term	Value
X_0	-177.6970	Z_0	-2768.3943	M_0	-414.8300
X_u	-30.9665	Z_u	-10.2889	M_u	15.6216
X_w	19.5888	Z_w	5.6317	M_w	0.5521
		Z_q	-6415.8238	M_q	-1388.0630
				$M_{\delta e}$	-6158.6482

Table 3.18: Elektra 1 Solar aerodynamic derivatives with minimal set of parameters.

	Identification Set				Validation Set			
Coefficient	u	w	q	θ	u	w	q	θ
GOF	0.9111	0.1807	0.9226	0.8890	0.4298	0.0651	0.8949	0.7554
TIC	0.0164	0.2535	0.1393	0.1251	0.0333	0.2612	0.1555	0.1869

Table 3.19: Averaged statistical measures for the states in model validation of Elektra 1 Solar with minimal set of parameters.

Overall, improvements are seen across the board in the statistical measures for Penguin BE, comparing to both results from Coelho [21] and Lee [15]. That is true even considering the identification using OEM with engine dynamics, making these the best results yet for this aircraft. For Elektra 1 Solar, the statistical measures are quite similar to each other, comparing both to the linear and nonlinear models of Lee [15].

From all cases, it can be seen that the vertical velocity w is the state that has the worst results. Coelho [21] and Lee [15] both agree this is due to GPS data not being sufficiently accurate.

3.4.2 Identification of Elektra 2 Solar

With the minimal set of parameters found, the system identification process was used for Elektra 2 Solar with data from IMU 1 first. The aerodynamic derivatives are in Table 3.20, the statistical measures of states, forces and moments are in Tables 3.21 and 3.22, and Figures 3.4 and 3.5 illustrate the model validation results for all states.

Term	**Value**	**Term**	**Value**	**Term**	**Value**
X_0	300.2103	Z_0	-3233.6376	M_0	-540.0559
X_u	-47.3480	Z_u	-76.6415	M_u	15.6499
X_w	26.9232	Z_w	-124.1343	M_w	-12.0922
		Z_q	-8582.7234	M_q	-1747.1684
				$M_{\delta e}$	-5309.2060

Table 3.20: Elektra 2 Solar aerodynamic derivatives using data from IMU 1.

	Identification Set				**Validation Set**			
Coefficient	u	w	q	θ	u	w	q	θ
GOF	0.7923	0.2647	0.8240	0.7123	0.8764	0.4040	0.8790	0.8475
TIC	0.0265	0.1307	0.1900	0.1382	0.0197	0.1066	0.1631	0.0943

Table 3.21: Averaged statistical measures for the states in model validation of Elektra 2 Solar using data from IMU 1.

	Identification Set			**Validation Set**		
Coefficient	X	Z	M	X	Z	M
R^2	0.6636	0.7060	0.5256	0.7371	0.7185	0.5638
$RMSE$	101.9982	307.6397	41.2157	84.9140	295.2983	40.6272
$NRMSE$	0.1293	0.0674	0.0533	0.1178	0.0688	0.0500

Table 3.22: Averaged statistical measures for the forces and moment in model validation of Elektra 2 Solar using data from IMU 1.

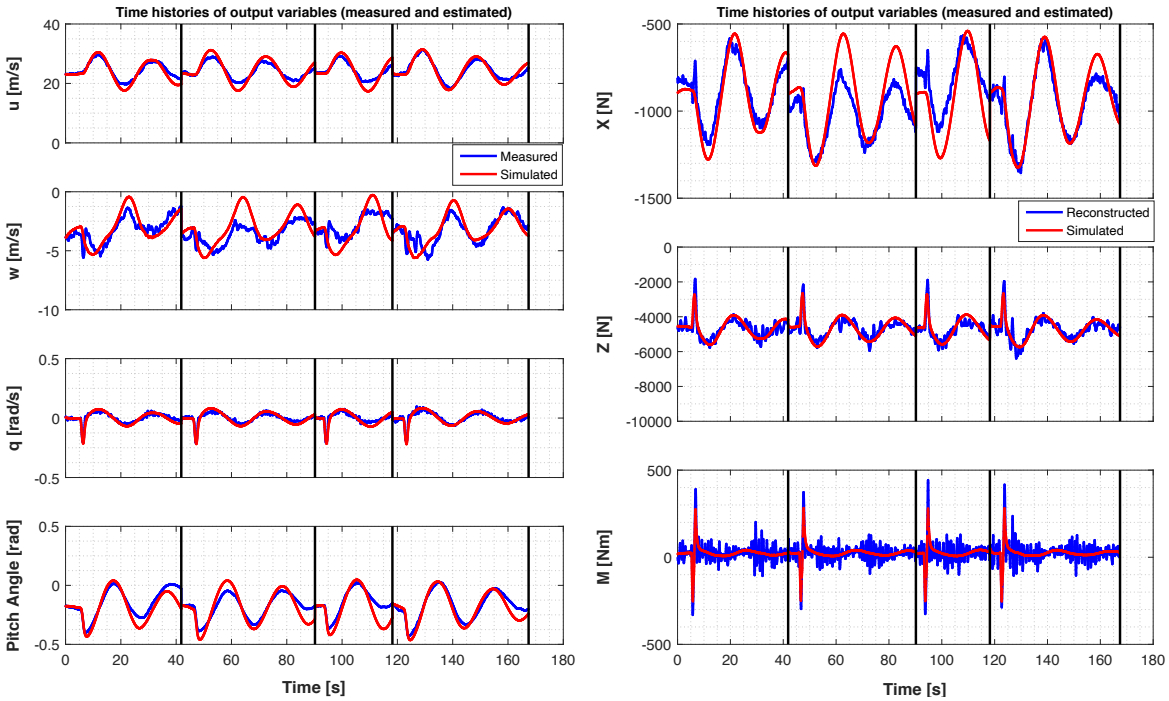

(a) States. **(b)** Forces and moment.

Figure 3.4: Model validation of the identification set of Elektra 2 Solar using a forward simulation.

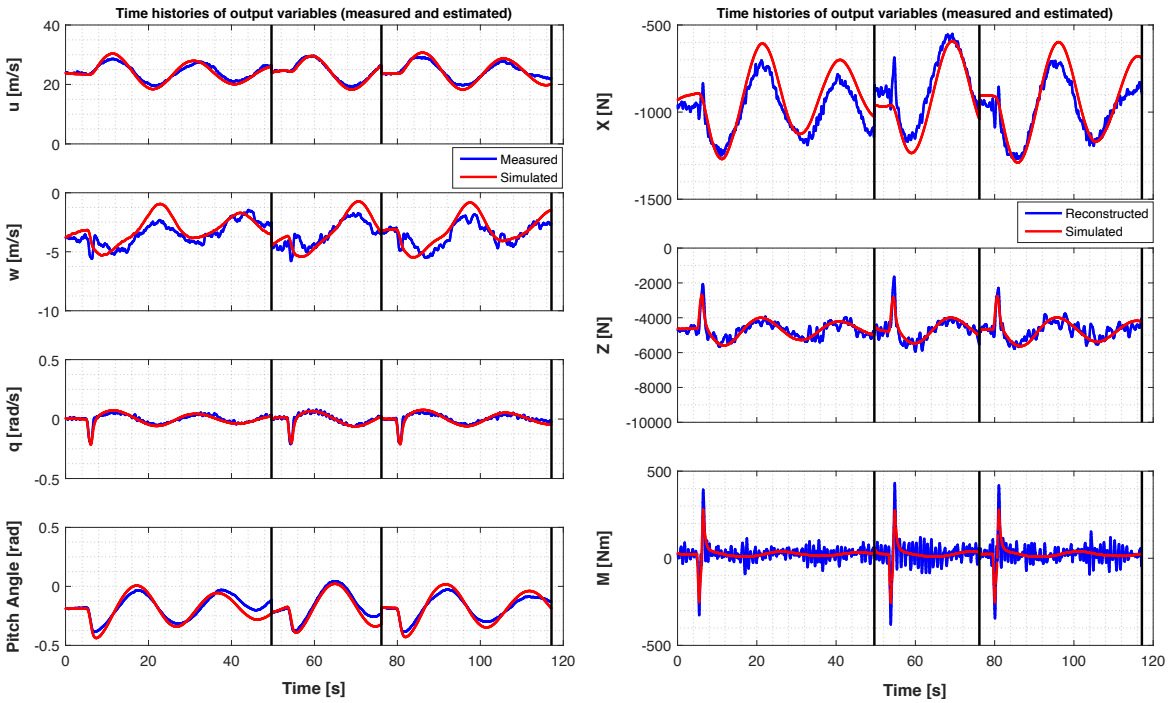

(a) States. **(b)** Forces.

Figure 3.5: Model validation of the validation set of Elektra 2 Solar using a forward simulation.

Overall, all TIC are below 0.2, complying to the established threshold of 0.3, and all the measures suggest a good agreement between the simulated data and the real data. Furthermore, from Table 3.23, it can be seen that, since the period error is less than 10% and the damping error is less than 0.02, the model can be considered high fidelity by FAA's standards [55].

Criteria	**Identified Model**	**Experiment**	**Error (Abs.)**	**Error (Rel.)**
Period	19.75s	20.61s	0.86s	4.1727%
Damping	0.0599	0.0663	0.0064	9.6531%

Table 3.23: Comparison of phugoid characteristics between the identified model and average of flight experiments.

Tables 3.24 and 3.25 show the aerodynamic derivatives of Elektra 2 Solar using data from IMU 2 and the averaged data respectively. Between IMUs 1 and 2, the mean average difference between parameters is 14.82%, with the maximum error being in X_w, where the difference is 43.51%, while all other errors are lower than 25%. Comparing the parameters from the average of the data to the average of the parameters from both data, the difference has a mean value of 1.41%, with the maximum also being in X_w, with 5.06%. The only parameters from the identification of the averaged data to not stay within the values of the same parameters from the individual identifications are Z_w and M_w, going over their closest boundaries by 0.72% and 0.51% respectively.

Term	**Value**	**Term**	**Value**	**Term**	**Value**
X_0	258.5348	Z_0	-3084.4334	M_0	-453.4846
X_u	-40.4951	Z_u	-82.4015	M_u	12.7566
X_w	47.6642	Z_w	-122.2783	M_w	-11.8109
		Z_q	-8280.1570	M_q	-1507.1400
				$M_{\delta e}$	-4727.7932

Table 3.24: Elektra 2 Solar aerodynamic derivatives using data from IMU 2.

Term	**Value**	**Term**	**Value**	**Term**	**Value**
X_0	285.0892	Z_0	-3156.1453	M_0	-496.5808
X_u	-44.4189	Z_u	-79.8533	M_u	14.1648
X_w	35.4966	Z_w	-125.0361	M_w	-12.1543
		Z_q	-8435.2024	M_q	-1629.5471
				$M_{\delta e}$	-5025.0314

Table 3.25: Elektra 2 Solar aerodynamic derivatives using averaged data from IMU 1 and IMU 2.

Tables 3.26 and 3.27 show the statistical measures of the identified system with data from IMU 2, and Tables 3.28 and 3.29 do the same for the identified system with averaged data, both of which have all TIC values are within the established threshold of 0.3. Furthermore, Tables 3.30 and 3.31 show the phugoid characteristics of each system, and it can be seen that both are also high fidelity models by FAA's standards [55].

Overall, like for Penguin BE and Elektra 1 Solar, all measures related to w seem to be where the biggest issues arise, which, as already mentioned, is likely due to the inaccuracy of GPS data. As explained in Section 3.2, one change made for the system identification of Elektra 2 Solar here was the use of an accurate estimate as data of longitudinal velocity u; Table 3.32 shows the statistical measures of the same identification process using IMU 1, but with GPS data instead for u. As can be seen, the results are considerably worse.

	Identification Set				**Validation Set**			
Coefficient	u	w	q	θ	u	w	q	θ
GOF	0.7902	0.2299	0.7882	0.6944	0.8958	0.4087	0.8566	0.8386
TIC	0.0266	0.1383	0.2118	0.1491	0.0181	0.1087	0.1812	0.1026

Table 3.26: Averaged statistical measures for the states in model validation of Elektra 2 Solar using data from IMU 2.

	Identification Set			**Validation Set**		
Coefficient	X	Z	M	X	Z	M
R^2	0.5448	0.7098	0.4171	0.6148	0.7274	0.4530
$RMSE$	126.3549	306.2740	48.8581	108.0324	290.9920	48.7621
$NRMSE$	0.1388	0.0665	0.0621	0.1409	0.0675	0.0604

Table 3.27: Averaged statistical measures for the forces and moment in model validation of Elektra 2 Solar using data from IMU 2.

	Identification Set				**Validation Set**			
Coefficient	u	w	q	θ	u	w	q	θ
GOF	0.7952	0.2535	0.8096	0.7086	0.8909	0.4165	0.8717	0.8504
TIC	0.0263	0.1336	0.1992	0.1421	0.0185	0.1066	0.1697	0.0960

Table 3.28: Averaged statistical measures for the states in model validation of Elektra 2 Solar using data averaged from IMUs 1 and 2.

	Identification Set			**Validation Set**		
Coefficient	X	Z	M	X	Z	M
R^2	0.6200	0.7106	0.4734	0.6897	0.7264	0.5113
$RMSE$	110.7495	305.4791	44.7321	94.2279	291.2510	44.3232
$NRMSE$	0.1305	0.0668	0.0573	0.1273	0.0677	0.0548

Table 3.29: Averaged statistical measures for the forces and moment in model validation of Elektra 2 Solar using data averaged from IMUs 1 and 2.

Criteria	**Identified Model**	**Experiment**	**Error (Abs.)**	**Error (Rel.)**
Period	21.93s	20.61s	1.32s	5.40%
Damping	0.0795	0.0663	0.0132	19.91%

Table 3.30: Comparison of phugoid characteristics between the identified model and average of flight experiments using data from IMU 2.

Criteria	**Identified Model**	**Experiment**	**Error (Abs.)**	**Error (Rel.)**
Period	19.67s	20.61s	0.94s	4.5609%
Damping	0.0715	0.0663	0.0052	7.8431%

Table 3.31: Comparison of phugoid characteristics between the identified model and average of flight experiments using data averaged from IMUs 1 and 2.

	Identification Set				**Validation Set**			
Coefficient	u	w	q	θ	u	w	q	θ
GOF	0.3821	-0.0780	0.6536	0.4744	0.3800	0.1024	0.7529	0.5944
TIC	0.0495	0.1583	0.2487	0.1806	0.0466	0.1307	0.2183	0.1496

Table 3.32: Averaged statistical measures for the states in model validation of Elektra 2 Solar using data from IMU 1 and only GPS data for u.

Controller Tuning and Landing Analysis of Elektra 2 Solar

4.1 Previous Work

The control system has in general been explained in Section 2.4. Muskardin [11] made a very comprehensive analysis of the landing procedure on mobile platforms using a demonstrator setup with a small UAV, and his work largely serves as a basis for what is developed in this chapter. While the system has been designed with HALE aircraft in mind, the only tests, even in simulation, that have been done up to this point have only used Penguin BE as the reference aircraft, and as such, this thesis is the first time the strategy will be analyzed with its actual target user.

4.2 Proposed Changes

During the development of this work, one of the problems found was related to the modeling of the vehicles inside of the MPC. Figure 4.1 shows the relative distances of a nominal landing procedure using the performance-based approach as it has been used so far. During the point of this testing, the vehicle controllers had already been tuned, and the time constants updated accordingly. Yet, as can be clearly observed, the system does not behave optimally, especially in the lateral direction. The landing was still successful, but this behavior is not what is expected of an optimal controller. While altering the weights used could somewhat improve this, the better solution in this case is to improve the prediction capabilities of the MPC by using more sophisticated vehicle models.

The solution presented in this work is to change the system models of the vehicles inside of the MPC to second order system approximations, instead of first order. In other words, rather of using only time constants to describe the individual vehicle responses to given setpoints, both natural frequency and damping factor will be considered instead. The models can then be written as:

$$\dot{x}_a = V_{k,a} \tag{4.1}$$
$$\dot{y}_a = \overline{V_K} \cdot \chi_a \tag{4.2}$$
$$\dot{V}_{k,a} = a_a \tag{4.3}$$
$$\dot{a}_a = (V_{k,a}^{des} - V_{k,a}) \cdot \omega_{V,a}^2 - 2 \cdot \xi_{V,a} \cdot \omega_{V,a} \cdot a_a \tag{4.4}$$
$$\dot{\chi}_a = \dot{\chi}_a \tag{4.5}$$
$$\ddot{\chi}_a = (\chi_a^{des} - \chi_a) \cdot \omega_{\chi,a}^2 - 2 \cdot \xi_{\chi,a} \cdot \omega_{\chi,a} \cdot \dot{\chi}_a \tag{4.6}$$
$$\dot{h}_a = \overline{V_K} \cdot \gamma_a \tag{4.7}$$
$$\dot{\gamma}_a = \dot{\gamma}_a \tag{4.8}$$
$$\ddot{\gamma}_a = (\gamma_a^{des} - \gamma_a) \cdot \omega_{\gamma,a}^2 - 2 \cdot \xi_{\gamma,a} \cdot \omega_{\gamma,a} \cdot \dot{\gamma}_a \tag{4.9}$$

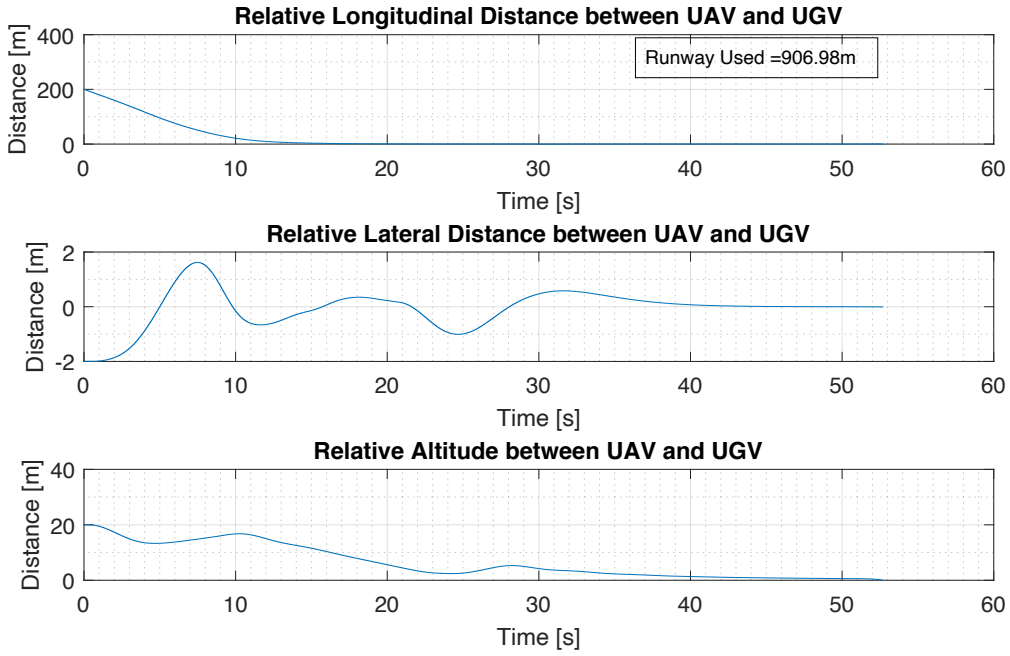

Figure 4.1: Nominal landing using first order system vehicle models inside of MPC.

$$\dot{x}_g = V_{k,g} \tag{4.10}$$
$$\dot{y}_g = \overline{V_K} \cdot \chi_g \tag{4.11}$$
$$\dot{V}_{k,g} = a_g \tag{4.12}$$
$$\dot{a}_g = (V_{k,g}^{des} - V_{k,g}) \cdot \omega_{V,g}^2 - 2 \cdot \xi_{V,g} \cdot \omega_{V,g} \cdot a_g \tag{4.13}$$
$$\dot{\chi}_g = \dot{\chi}_g \tag{4.14}$$
$$\ddot{\chi}_g = (\chi_g^{des} - \chi_g) \cdot \omega_{\chi,g}^2 - 2 \cdot \xi_{\chi,g} \cdot \omega_{\chi,g} \cdot \dot{\chi}_g \tag{4.15}$$

where $\omega_V, \omega_\chi, \omega_\gamma$ and $\xi_V, \xi_\chi, \xi_\gamma$ are the natural frequencies and dampening of velocity, course angle and flight path angle respectively. Note that the system of equations is still linear, but compared to before, 3 states were added, those being $\dot{\chi}_a$, $\dot{\gamma}_a$ and $\dot{\chi}_g$, which brings the total number of states to 15 from the previous 12 ($x_a, y_a, V_{k,a}, a_a, \chi_a, h_a, \gamma_a, x_g, y_g, V_{k,g}, a_g, \chi_g$).

In very general terms, the advantage of using a second order system model approximation over a first order one is the capability of representing overshoots. Much of the control literature references "optimal" strategies as those with a closed-loop response damping factor of 0.7, which has a low overshoot and much faster response time than what could be had with no overshoot at all [34; 63–65]. Being able to better represent such a case, therefore, can possibly increase the performance of applications of the MPC, hence why such a change is important not only to this case but also future works.

4.3 Methodology

For the UAV model, the longitudinal aerodynamics will use the high fidelity model developed in Chapter 3, the lateral aerodynamics will use parameters of a VLM-based model previously available, and the propulsion will use the provided model.

For the tests executed here, a couple of things are carried over from Muskardin's work [11]. First, the same slow actuation ground vehicle model and a geometrical limit of $80cm$ from the center of the vehicle for landing the UAV is used. This would be unreasonable for a real application, but it is enough for this initial investigation on the feasibility of this strategy. Furthermore, it will allow for direct comparison with the demonstrator setup used by Muskardin [11] and Muskardin et al. [24; 28], which can grant insight into how the results of a test with a small UAV can be translated to HALE aircraft. For a complete analysis, there are five important steps that need to be taken.

First, a controller tuning for the UAV and UGV must be done. A time domain design will be used with optimization based tuning, as presented in Section 2.5. In all cases, appropriate steps in setpoint will be given. The costs for each optimization can be summarized as follows:

- UAV TECS controller gains: IAE, settling time and overshoot of airspeed and altitude; ISCD of elevator and throttle.
- UAV lateral controller gains: IAE, settling time and overshoot of course angle; ISCD of aileron.
- UGV velocity control: IAE, settling time and overshoot of velocity; ISCD of engine.
- UGV lateral control: IAE, settling time and overshoot of course angle; ISCD of steering wheel.

As initial guesses, for the UAV, the gains used in-flight for Elektra 2 Solar in experiments will be used; those are in Table 4.1. For the UGV, the initial guess will be the gains used in Muskardin [11], reproduced in Table 4.2. Finally, the algorithm of choice to solve the optimization problem was based on the Nelder-Mead method [66].

Second, the cooperative horizontal synchronization controller gains must be tuned, for both the safety and performance based approaches. For setup, the aircraft will begin the simulation $5m$ behind and $5m$ to the left of the UGV, with both having the same groundspeed of $21m/s$, constituting an initial phase of the optimization of compensating for initial displacement. At $50s$, a wind gust which is $5m/s$ headwind and $5m/s$ crosswind hits the aircraft, marking the start of the disturbance rejection phase, which also lasts $50s$. For the entire duration, a communication time delay between aircraft and ground vehicle of $100ms$ will be used; this value comes from an investigation conducted by Muskardin [11], where the time delayed stayed between values of $50ms$ and $300ms$, with an average around $100ms$. As costs, IAE, settling time and overshoot of longitudinal and lateral errors for both initial displacement and disturbance rejection phases will be used. The same weights will be used for the optimizations of both safety and performance based approaches. For initial guesses, an

Parameter	Value	Parameter	Value
K_θ	0.2	K_{thr}	1
$K_{i,\theta}$	0	$K_{i,thr}$	2
K_q	0.36	K_{FF}	1
K_h	0.5	K_{Va}	0.5
KEP	1	KTP	1
KEI	1	KTI	1

(a) TECS gains.

Parameter	Value
K_p	0.503
K_ϕ	4.042
$K_{i,\phi}$	0
K_χ	0.1636
$K_{i,\chi}$	0

(b) Lateral controller gains.

Table 4.1: Controller gains used in-flight for Elektra 2 Solar.

Parameter	Value	Parameter	Value
K_T	0.7894	K_χ	0.895
$K_{i,T}$	0.1084	$K_{i,\chi}$	0

Table 4.2: Initial guess for UGV controller gains. Adapted from: [11].

investigation is first made with second-order system approximations across thousands of possible values (generated randomly) and the best result is kept as an initial guess for the optimization with the better model. Again, the Nelder-Mead algorithm is used.

Once the optimal gains of the horizontal synchronization controllers have been found, an analysis must be conducted. First the results will be directly compared across different communication time delays, to see the limits of stability of the performance-based approach. Then, their capabilities of wind rejection will be evaluated in a direct comparison where the strongest wind gusts that can hit the aircraft from all four main directions without causing a retry of the landing procedure will be found. Lastly, a stochastic analysis will be performed, using a Monte Carlo approach with wind gust intensity, angle and duration, as well as communication time delay, as randomly generated inputs, and from that, the disturbance rejection capabilities of both approaches will be evaluated. For more on Monte Carlo analysis, the reader is referred to Fishman [69]. A total of 1000 iterations will be made.

The focus then shifts briefly to the new modeling of the vehicles inside of the MPC. For the weights, they will be the same as the adaptive weights suggested by Pavani [30], which were also used to generate the response from Figure 4.1. Once tested, the trajectory will then be compared to the previous one to study the advantages and disadvantages of the new approach.

Afterward, the nominal landing can be studied. For the safety-based approach, no additional tuning is necessary at this point. For the performance-based approach, however, one last optimization can be done on the weights of the MPC. As costs, the time and runway used to trigger the flare state, as well as the positional error and velocity error when that occurs, can be considered. For initial guesses, the weights from Pavani [30] are used, as well as additional 0.1 constant and linear weights to the

new states $\dot{\chi}_a$ and $\dot{\chi}_g$, as well as constant weight 0.1 for $\dot{\gamma}_a$. Then, both approaches can be directly compared, both in qualitative ways, and using their most important metrics, which are the total runway used and total time to complete the landing.

Finally, a stochastic analysis of the landing can be done. Once again, Monte Carlo is used for such, and as variable inputs, the initial position and velocity of the aircraft, as well as communication time delay and background wind, are chosen. As outputs, the terminal position errors and velocity errors are considered together with runway used and time elapsed to touchdown. A total of 1000 iterations will be made once more.

4.4 Results

4.4.1 Controller Tuning of Elektra 2 Solar and Ground Vehicle

The optimal controller gains for Elektra 2 Solar can be found on Table 4.3, and the system response with the initial gains and optimized gains can be see in Figure 4.2. The response with optimal parameters presents an overshoot of $0.19m/s$ and a settling time of $21.4s$ for the airspeed, with no overshoot and $15.36s$ of settling time for altitude. Overall, gain margins of $11.8dB$ and $9.55dB$ and phase margins of 141° and 178° for airspeed and altitude respectively can be found on the linearized system as well, proving its stability.

For the lateral control, as illustrated in Figure 4.3, no overshoot is observed, and the settling time is $12.68s$; a gain margin of $20.4dB$ and phase margin 176° can be found, which is also stable.

Parameter	Value	Parameter	Value
K_θ	0.3396	K_{thr}	1.1065
$K_{i,\theta}$	0.0045	$K_{i,thr}$	1.7824
K_q	0.3801	K_{FF}	1.1366
K_h	0.2285	K_{Va}	0.2465
K_{EP}	1	K_{TP}	1
K_{EI}	1.6179	K_{TI}	1.6179

(a) TECS gains.

Parameter	Value
K_p	0.463
K_ϕ	3.2885
$K_{i,\phi}$	0.0598
K_χ	0.1513
$K_{i,\chi}$	0.0001

(b) Lateral controller gains.

Table 4.3: Controller gains for Elektra 2 Solar found with the optimization procedure.

For the UGV, the optimal control gains can be found on Table 4.4, and the system response for steps in setpoints of velocity and course angle can be seen in Figures 4.4b and 4.5. For velocity, the overshoot is $0.5102m/s$ and the settling time is 3.02, while for the course angle no overshoot is seen and the settling time is $3.89s$. The velocity control has a phase margin of 146° and the steering control has a phase margin of 179°.

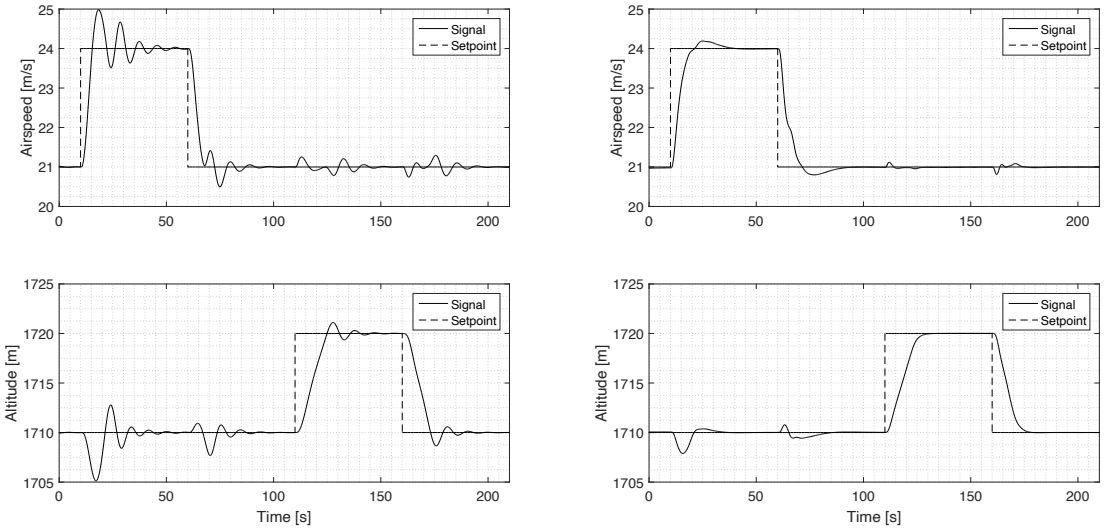

(a) Flight gains. **(b)** Optimized gains.

Figure 4.2: Aircraft response to steps in setpoint of both airspeed and altitude using the same gains used in-flight and optimized gains.

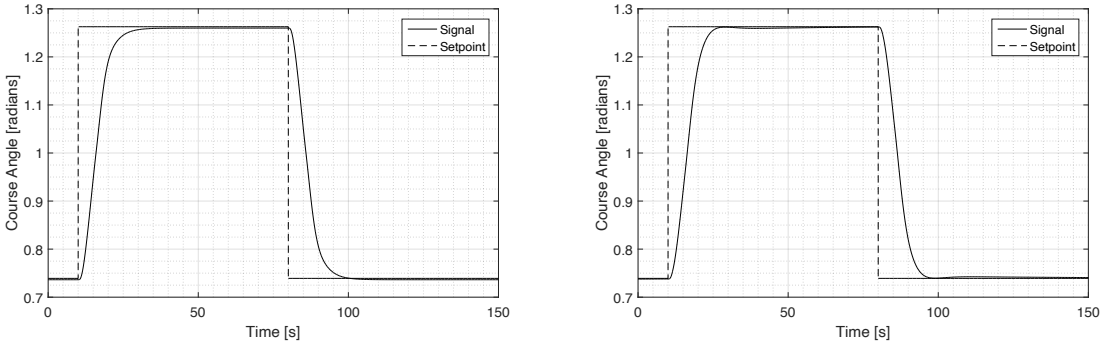

(a) Flight gains. **(b)** Optimized gains.

Figure 4.3: Aircraft response to steps in setpoint of course angle using the same gains used in-flight and optimized gains.

Parameter	Value	Parameter	Value
K_T	0.3699	K_χ	1.5801
$K_{i,T}$	0.0201	$K_{i,\chi}$	0.0001

Table 4.4: Initial guess for UGV controller gains. Adapted from: [11].

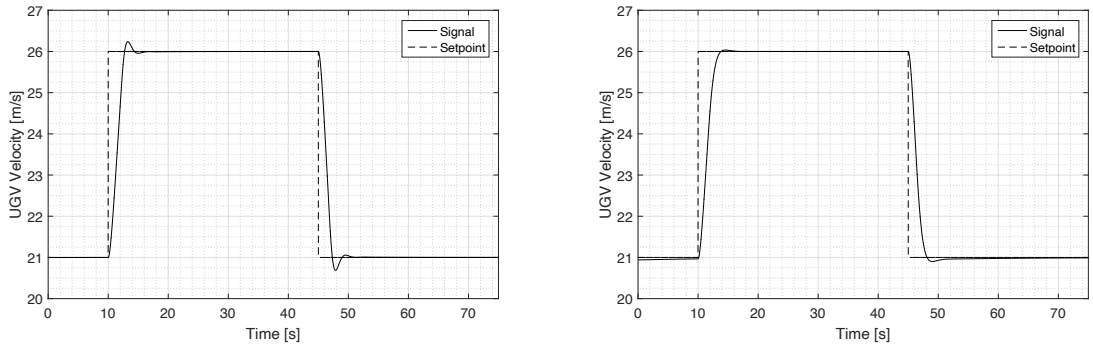

(a) Initial gains. **(b)** Optimized gains.

Figure 4.4: Ground vehicle response to steps in setpoint of groundspeed using initial gains and optimized gains.

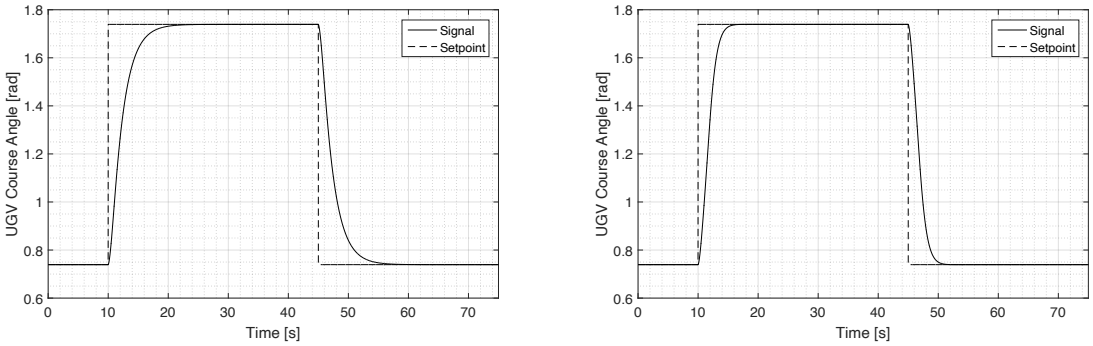

(a) Initial gains. **(b)** Optimized gains.

Figure 4.5: Ground vehicle response to steps in setpoint of course angle using initial gains and optimized gains.

4.4.2 Controller Tuning of Cooperative Control

Results for both the safety-based approach and performance-based approach can be found in Figure 4.6 and the controller gains can be found in Tables 4.5 and 4.6 for safety-based and performance-based respectively. For the settling time here, the limit criteria is $20cm$ of error in the considered direction. For the overshoot during disturbance rejection, the maximum peak is considered.

The safety-based approach has a settling time of $9.7s$ and $33.85s$ for longitudinal and lateral directions respectively during the initial displacement phase, and $18.2s$ and $29.4s$ during disturbance rejection. In the same order, it presents overshoots of $1.49m$, $0m$, $3.10m$ and $3.12m$.

The performance-based approach has a settling time of $23.85s$ and $7.75s$ for longitudinal and lateral directions respectively during the initial displacement phase, and $11.75s$ and $17.3s$ during disturbance rejection. In the same order, it presents overshoots of $2.08m$, $0.01m$, $1.93m$ and $0.89m$. Compared to the safety-based approach, during disturbance rejection, the settling time in longitudinal direction is 54% better, and on

Vehicle	Parameter	Value
UGV	$K_{p,XG}$	-0.7404
	$K_{i,XG}$	-0.1805
	$K_{v,XG}$	-0.2623
UAV	$K_{p,YA}$	0.2191
	$K_{i,YA}$	0.0007
	$K_{v,YA}$	1.4613

Table 4.5: Optimized controller gains for the safety-based horizontal synchronization control.

the lateral direction the time is almost half of the safety-based one. Overshoots show improvement of 60.6% and 250.56% in longitudinal and lateral directions.

	Longitudinal		Lateral	
Vehicle	**Parameter**	**Value**	**Parameter**	**Value**
UGV	$K_{p,XG}$	-0.7370	$K_{p,YG}$	-0.2917
	$K_{i,XG}$	-0.0002	$K_{i,YG}$	-0.0002
	$K_{v,XG}$	-1.0522	$K_{v,YG}$	-0.0020
UAV	$K_{p,XA}$	0.9818	$K_{p,YA}$	0.0564
	$K_{i,XA}$	0.0217	$K_{i,YA}$	0.0001
	$K_{v,XA}$	0.2310	$K_{v,YA}$	0.1252

Table 4.6: Optimized controller gains for the performance-based horizontal synchronization control.

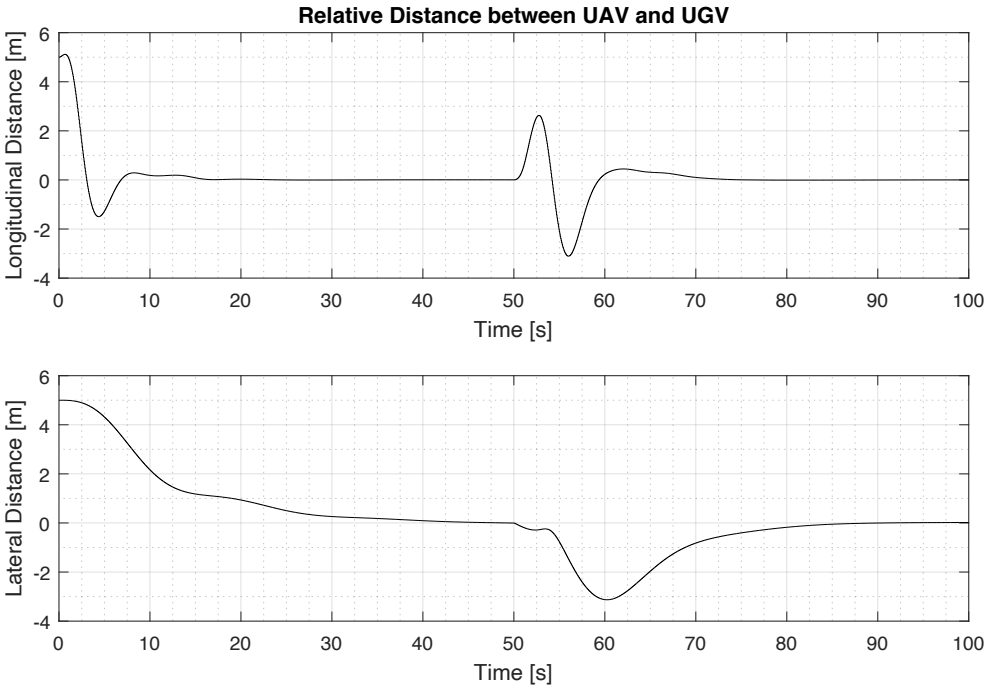

(a) Safety-based controller.

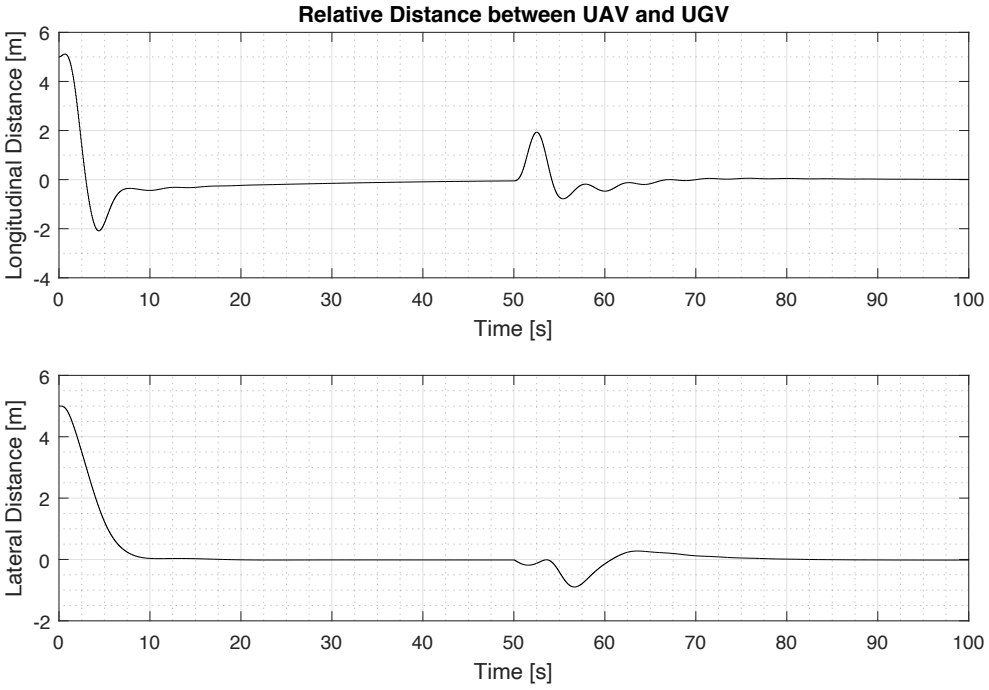

(b) Performance-based controller.

Figure 4.6: System response to an initial displacement and disturbance, nominal case.

4.4.3 Analysis of Cooperative Control

Figure 4.7 shows the system response to a wind disturbance given different values of communication time delay. As can be observed, the safety-based approach is stable through all values of delay, from $0ms$ to $900ms$. The performance-based approach, however, starts to show oscillations around $500ms$ of delay, and is already unstable at $700ms$. This illustrates the advantage the safety-based approach has over the performance one. For the purposes of this work, however, the delay will be bound between $0ms$ and $300ms$, as explained before, and therefore, this will have no effect on the next results.

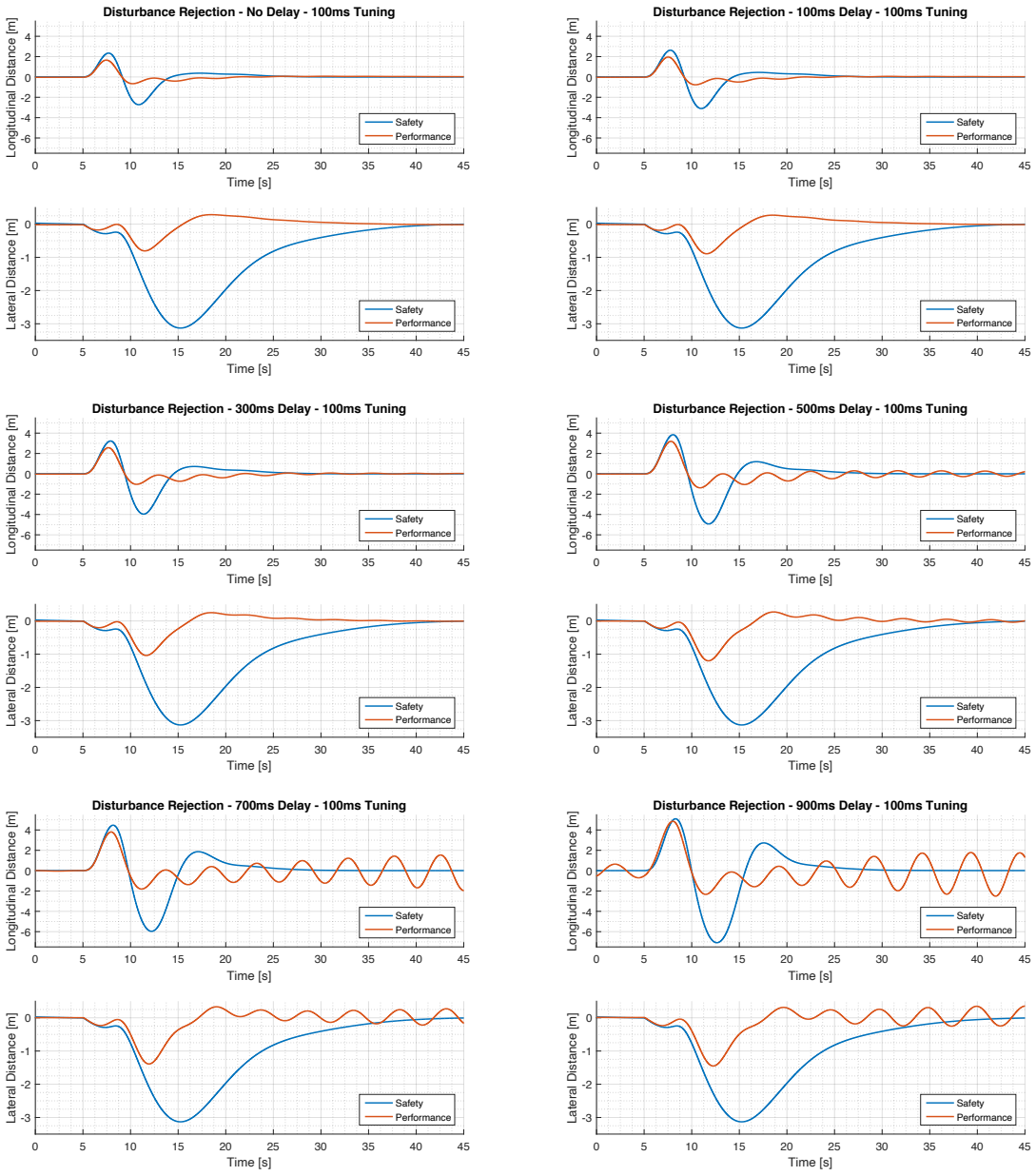

Figure 4.7: Comparison of the safety-based controller and the performance-based controller with increasing communication time delay.

Next, the performance limits are analyzed. These results are in Figure 4.8, for both the nominal case of delay (100ms) and the worst-case (300ms). As can be observed, only marginal enhancements are really seen in the longitudinal direction between different architectures, but on the lateral direction, the improvements are much more pronounced, with the performance-based approach being able to reject winds of intensity three times as strong in the nominal worst cases.

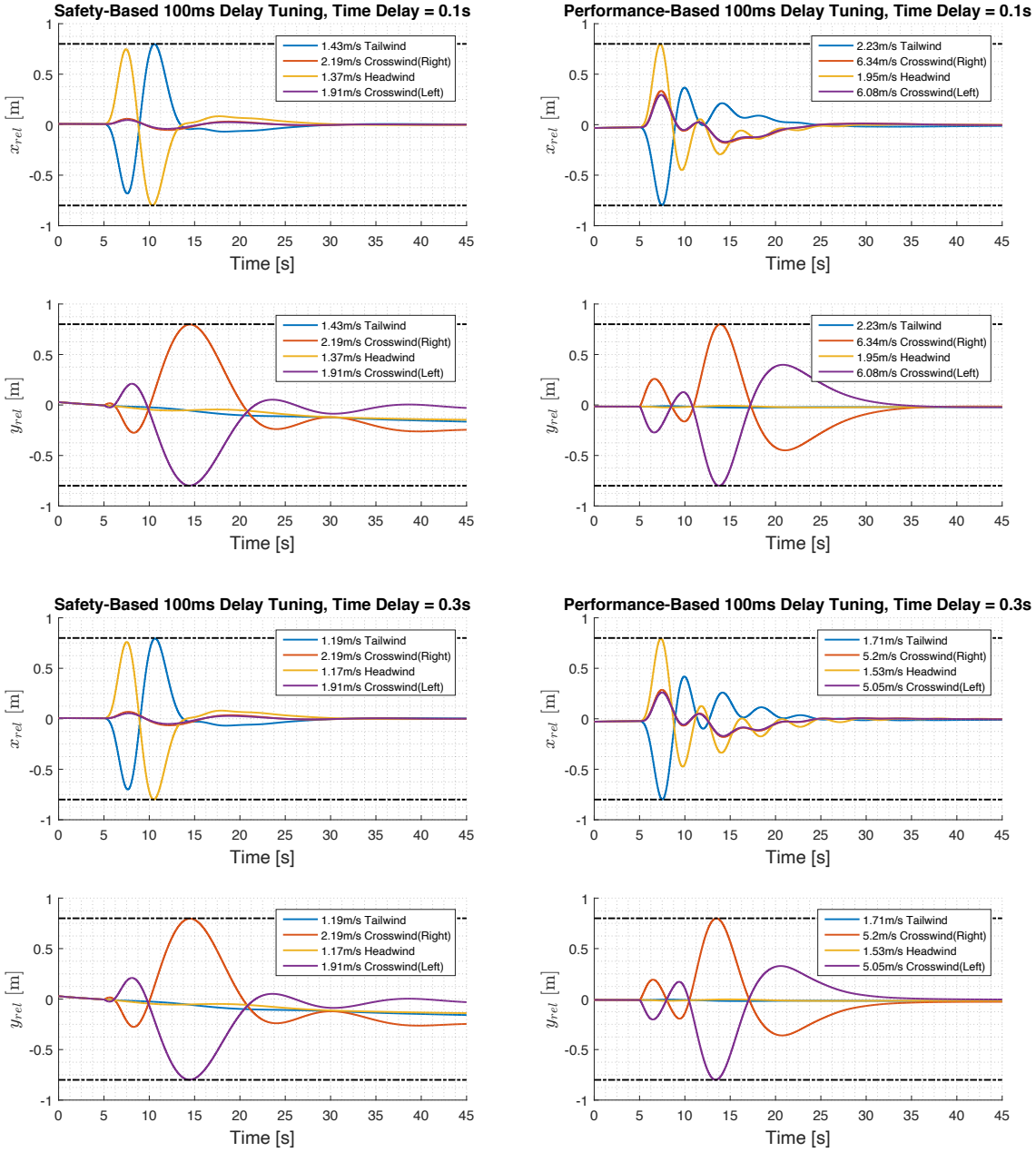

Figure 4.8: Maximum wind in each principal direction to cause a retry on the maneuver for nominal and worst-case values of communication time delay.

Finally, the stochastic analysis was performed. The generated inputs are shown in Figure 4.9 and the outputs for both architectures is shown on Figure 4.10.

In summary for the inputs, the time delay had a mean value of $0.1s$ and a standard deviation of $0.05s$, and the wind had an average intensity of $5m/s$ for $10s$, with standard deviations of $1m/s$ and $3s$ respectively.

As for the outputs, the performance-based approach shows the best statistics across the board. For overshoot, both mean value and standard deviation of the performance-based approach were smaller than those of the safety-based by about 33% on the longitudinal case and 66% on the lateral one. Settling time showed considerable variance for both, with 96% of the data from the safety-based approach staying between $7.55s$ and $32.7s$ for the longitudinal case and $3.95s$ and 46.9 for the lateral one, while the performance-based approach had boundaries of $0s$ and $28.35s$ and $0s$ and $33.3s$ respectively, which are 13.3% and 29% of improvement in the worst cases respectively. Note here that a settling time of zero means the position error never got higher than $0.2m$ in that particular case. Finally, for IAE, while in the longitudinal the difference is not as considerable, in the lateral direction, there's a 71.4% improvement on average, while also having considerably smaller boundaries to fit 96% of the data, going from 19.9 and 112.6 to 4.2 and 33.0.

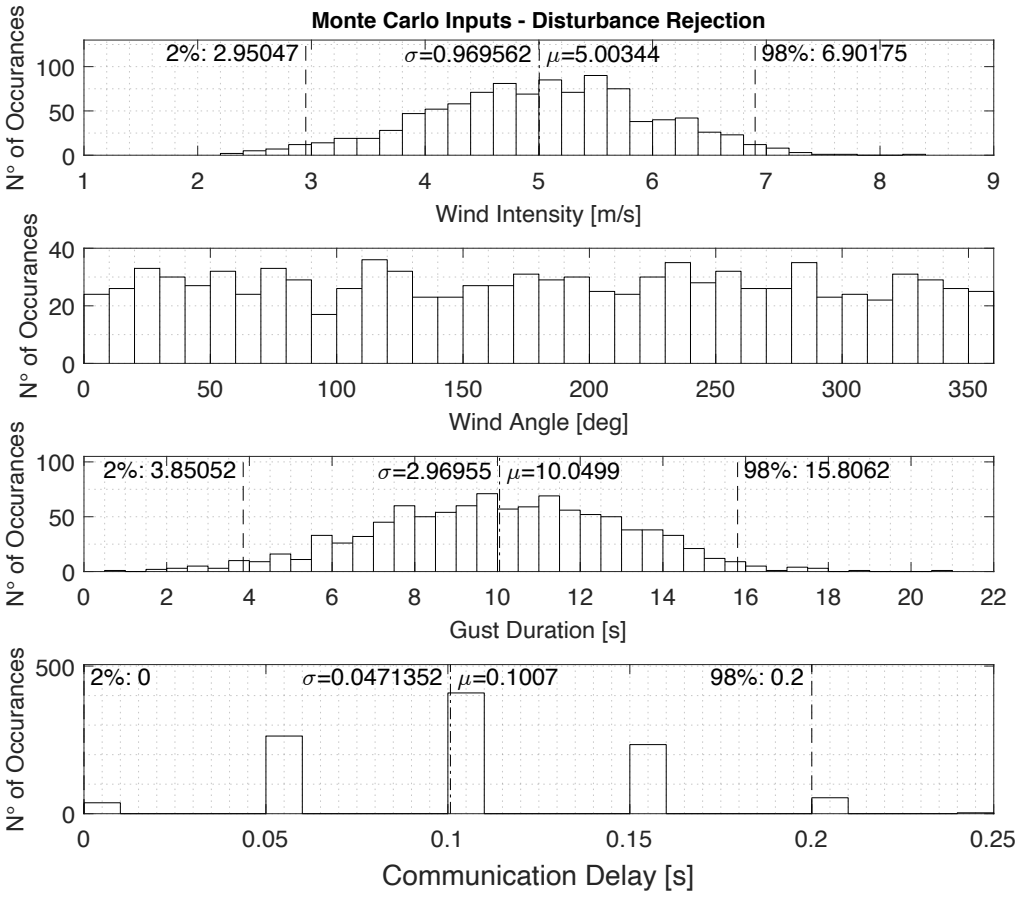

Figure 4.9: Randomly generated inputs for Monte Carlo analysis for landing.

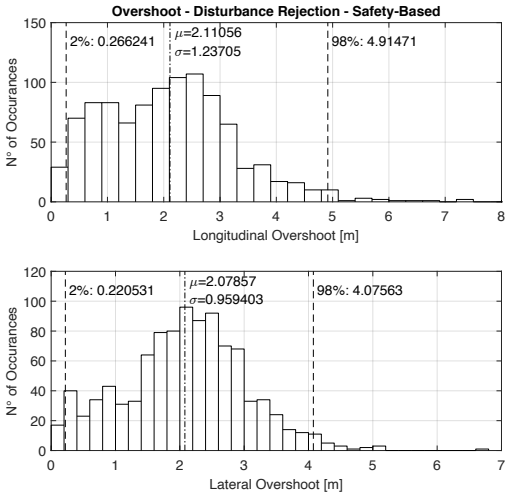

(a) Overshoot (safety).

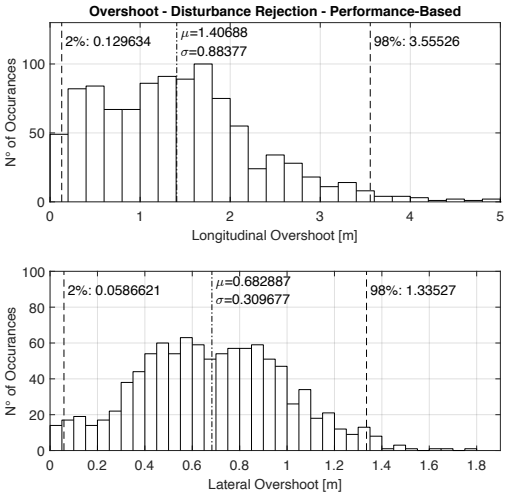

(b) Overshoot (performance).

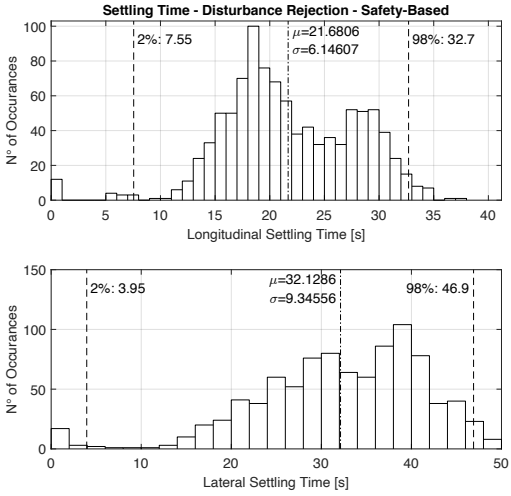

(c) Settling time (safety).

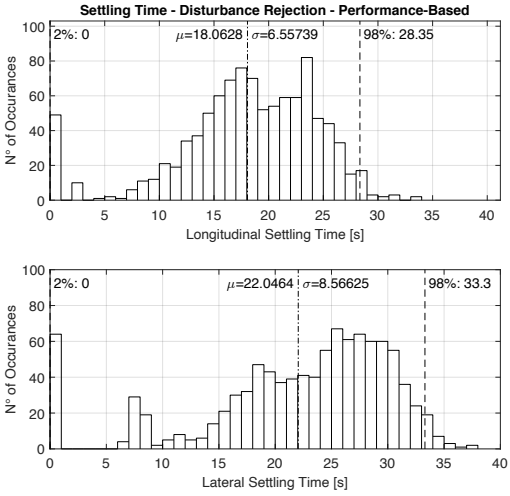

(d) Settling time (performance).

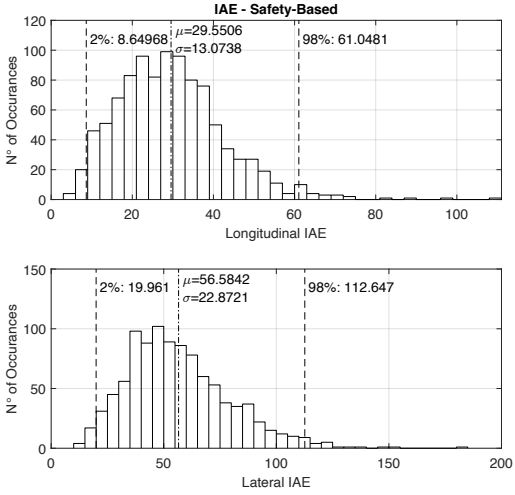

(e) IAE (safety).

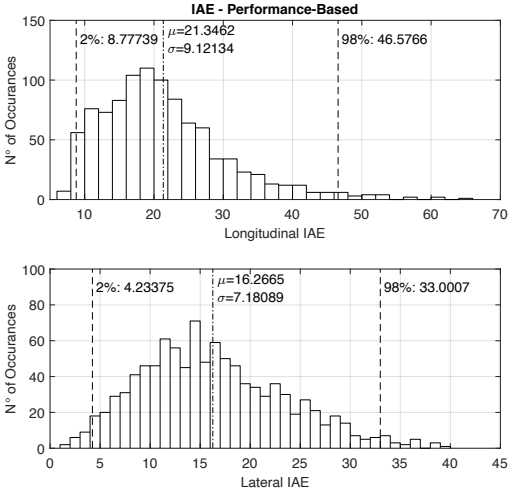

(f) IAE (performance).

Figure 4.10: Outputs of the Monte Carlo analysis for disturbance rejection.

4.4.4 Second Order System Modeling for Model Predictive Control

First, the time constants, natural frequencies and damping of the optimized closed-loop control of Elektra 2 Solar when modeled as first and second order systems were found. They are shown in equations 4.16 to 4.20.

$$\tau_{\gamma,a} = 1.82s \qquad \omega_{\gamma,a} = 0.99rad/s \qquad \xi_{\gamma,a} = 0.60 \tag{4.16}$$
$$\tau_{V,a} = 4.46s \qquad \omega_{V,a} = 0.38rad/s \qquad \xi_{V,a} = 0.78 \tag{4.17}$$
$$\tau_{\chi,a} = 6.94s \qquad \omega_{\chi,a} = 0.25rad/s \qquad \xi_{\chi,a} = 0.78 \tag{4.18}$$
$$\tau_{V,g} = 1.59s \qquad \omega_{V,g} = 1.03rad/s \qquad \xi_{V,g} = 0.75 \tag{4.19}$$
$$\tau_{\chi,g} = 1.92s \qquad \omega_{\chi,g} = 0.93rad/s \qquad \xi_{\chi,g} = 0.85 \tag{4.20}$$

The presented time constants were used to produce the results of the first order system approximation MPC shown in Figure 4.1. After making the necessary changes, the results from a nominal landing with the MPC using second order systems approximations is shown in Figure 4.11

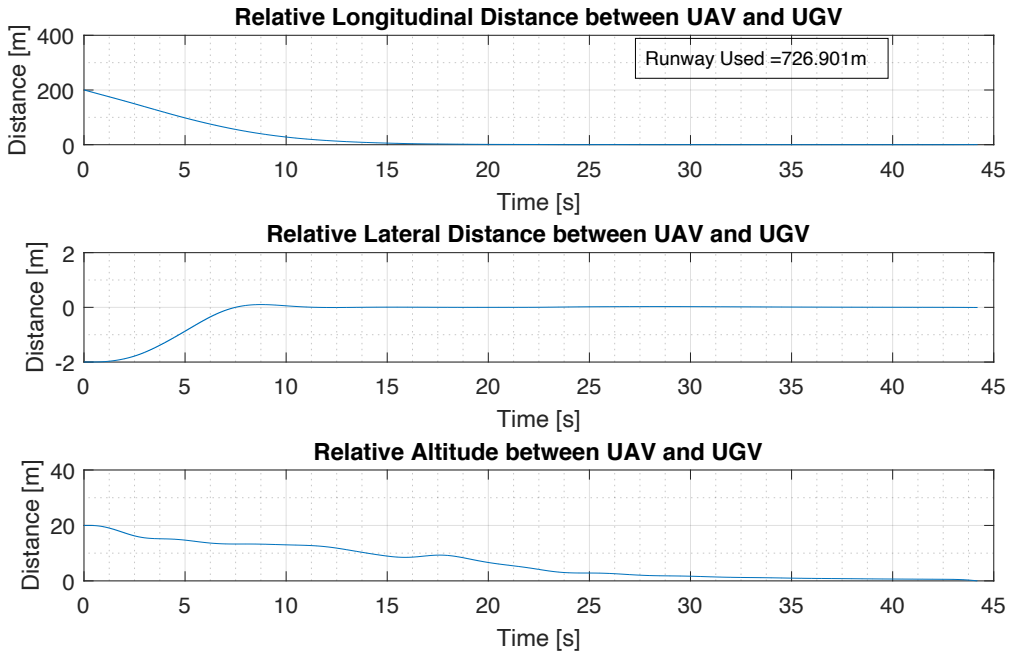

Figure 4.11: Nominal landing using second order system vehicle models inside of MPC.

With this change alone compared to the results of Figure 4.1, the oscillations in lateral direction are completely gone, and the runway used to complete the landing was reduced from $906.9m$ to $728.9m$.

As expected, however, inserting more states comes at a computational performance cost. In the author's computer, with first order system models, the simulation took in

total an average of 36.93s of real-world time for 53.5s of simulation, while with second order system models, the simulation took in total an average of 40.94s of real-world time for a 44.3s of simulation. In other words, for one second of simulation, the first order system model MPC requires 0.69s of real-world time and the second order system model MPC requires 0.92s, making it about 33.3% more computationally expensive in comparison. In practical applications, it is important to keep the computational limits available in mind. For the purposes of this thesis, however, the landing performance benefits far outweigh the extra computational cost involved, and therefore, the second order system variant of the MPC will be used for all subsequent results.

4.4.5 Nominal Landing

Figures 4.12 and 4.13 show the results of the nominal landing case with the safety-based architecture. A total of 683.2m of runway were used to complete the maneuver in 41.8 seconds. The small descent in altitude during the "hold altitude" state is simply due to the trim condition not being very exact to the initial conditions, as explained in Muskardin [11], and has no impact in the analysis. In figure 4.13b one can see a sudden oscillation in longitudinal direction when the position error is almost 0 for the first time; this is due to the switch between linear acceleration of the UGV and cooperative control. A few different strategies were tested to diminish this effect, and the best one found was making the change when the UAV and UGV are 5 meters apart. A more thorough analysis should be conducted in the future to further reduce this effect, but as is, this has no impact in further analysis. Furthermore, upon entering the "ground lock" state, a sudden displacement of the aircraft can be seen due to engine retardation, which causes it to quickly lose speed. Lastly, a small error can be seen in the lateral direction, which could be due to slow lateral dynamics of the aircraft.

For the MPC, the optimal weights found are:

$$p_x^k = 9.21 \quad p_y^k = 6.30 \quad p_V^k = 10.66 \quad p_a^k = 4.48 \quad p_\chi^k = 2.15 \quad p_{\dot{\chi}}^k = 0.62 \tag{4.21}$$

$$p_x^l = 2.51 \quad p_y^l = 0.00 \quad p_V^l = 97.35 \quad p_a^l = 48.36 \quad p_\chi^l = 1.24 \quad p_{\dot{\chi}}^l = 0.24 \tag{4.22}$$

$$q_{V,a} = 7.48 \quad q_{\chi,a} = 9.79 \quad q_{V,g} = 8.76 \quad q_{\chi,g} = 15.77 \tag{4.23}$$

$$r_{V,a} = 1.06 \quad r_{\chi,a} = 15.67 \quad r_{V,g} = 1.60 \quad r_{\chi,g} = 16.66 \tag{4.24}$$

$$w_{x,g} = 13.56 \quad w_{y,g} = 0.03 \tag{4.25}$$

$$p_h = 5.22 \quad p_\gamma = 1.11 \quad p_{\dot{\gamma}} = 0.08 \tag{4.26}$$

$$q_\gamma = 1.25 \tag{4.27}$$

$$r_\gamma = 16.09 \tag{4.28}$$

Figures 4.14 and 4.15 show the results of the nominal landing case with the performance-based architecture. A total of 592.3m of runway were used to complete the maneuver in 37.5 seconds. This represents an improvement of 90.9m or 13.3% in amount of runway used, and 4.3s or 10.3% in time to touchdown. In arriving at flare, it can be seen both position and velocity errors in the horizontal plane are essentially zero, which highlights a point in which the performance-based controller has a significant advantage besides using less runway.

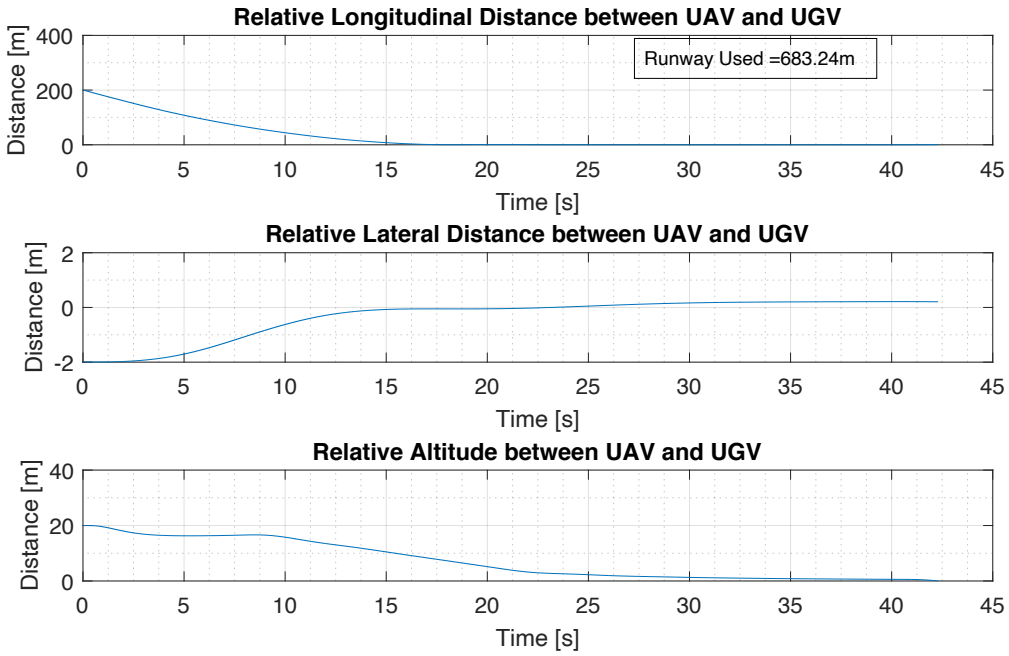

Figure 4.12: Nominal landing with the safety-based approach.

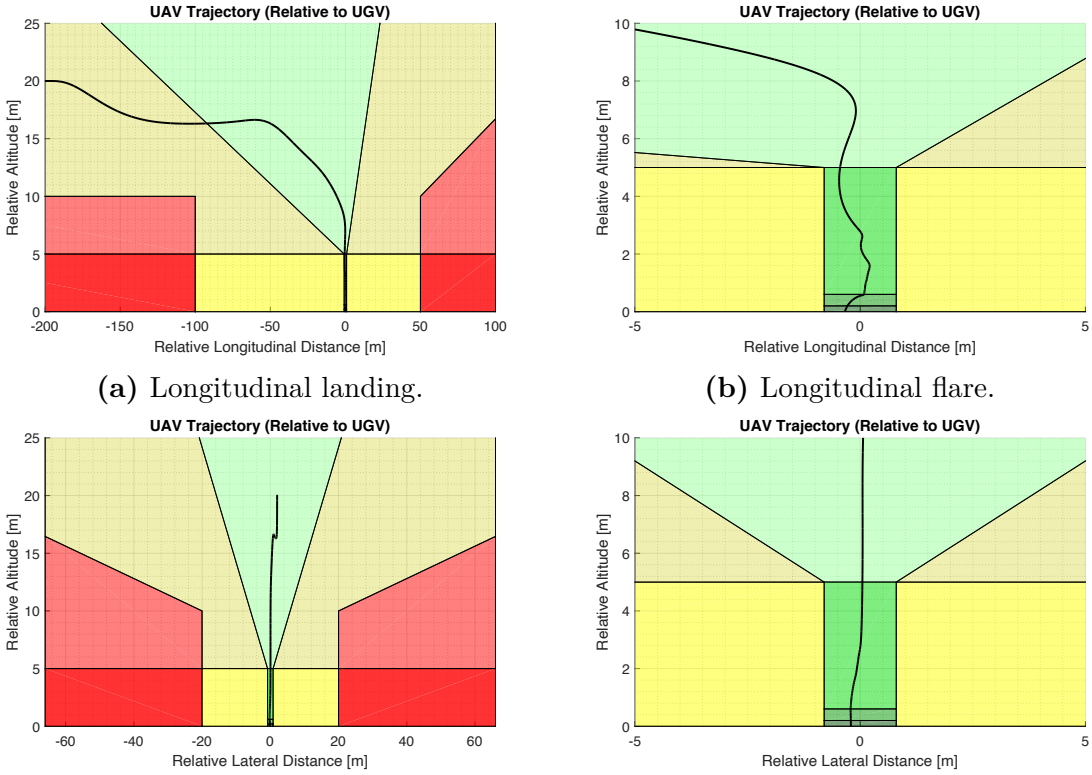

(a) Longitudinal landing.

(b) Longitudinal flare.

(c) Lateral landing.

(d) Lateral flare.

Figure 4.13: Trajectory of a nominal landing with safety-based approach.

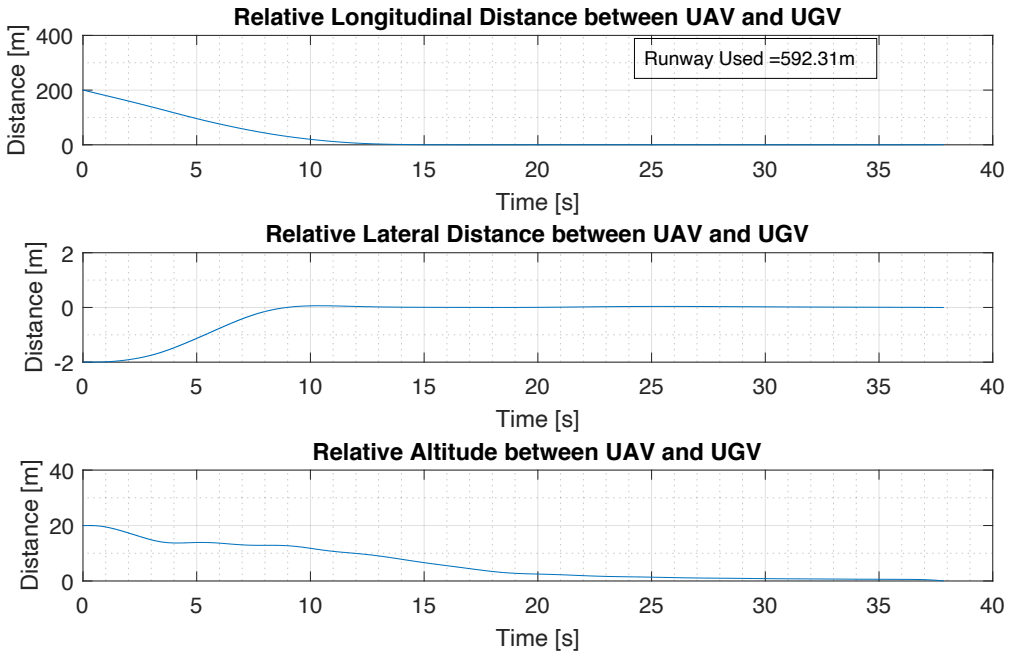

Figure 4.14: Nominal landing with the performance-based approach.

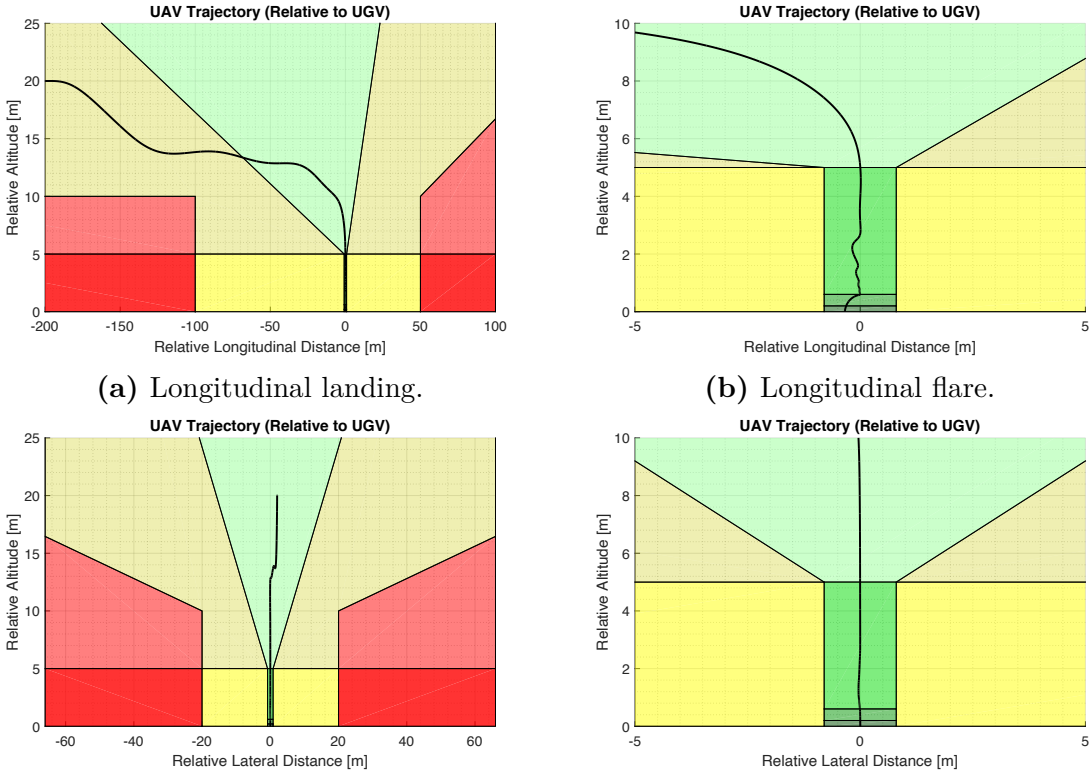

(a) Longitudinal landing.

(b) Longitudinal flare.

(c) Lateral landing.

(d) Lateral flare.

Figure 4.15: Trajectory of a nominal landing with performance-based system.

4.4.6 Stochastic Landing Analysis

Lastly, a stochastic analysis of the landing procedure using both safety-based and performance-based architectures was performed. Figure 4.16 shows the generated inputs, and Figure 4.17 illustrates the results.

While the longitudinal error upon touchdown is similar in both cases due to engine cutoff, the lateral error shows much reduced variance in the performance-based controller. 96% of the results from the safety-based approach are within $-0.36m$ and $0.53m$, while for the performance-based one that is bound between $-0.088m$ and $0.082m$.

In terms of time and runway used, the safety-based controller averages $43.8s$ and $748.9m$, with 96% of the data being between 38.8 and 53.2 seconds and 633.8 and 959.6 meters. The performance-based controller averages $41.2s$ and $687.1m$, with 96% of the data being between 33.7 and 49.4 seconds and 582.9 and 915.2 meters. Both strategies show about the same variance, but the performance-based approach is about 6.3% faster and uses 9.0% less runway on average.

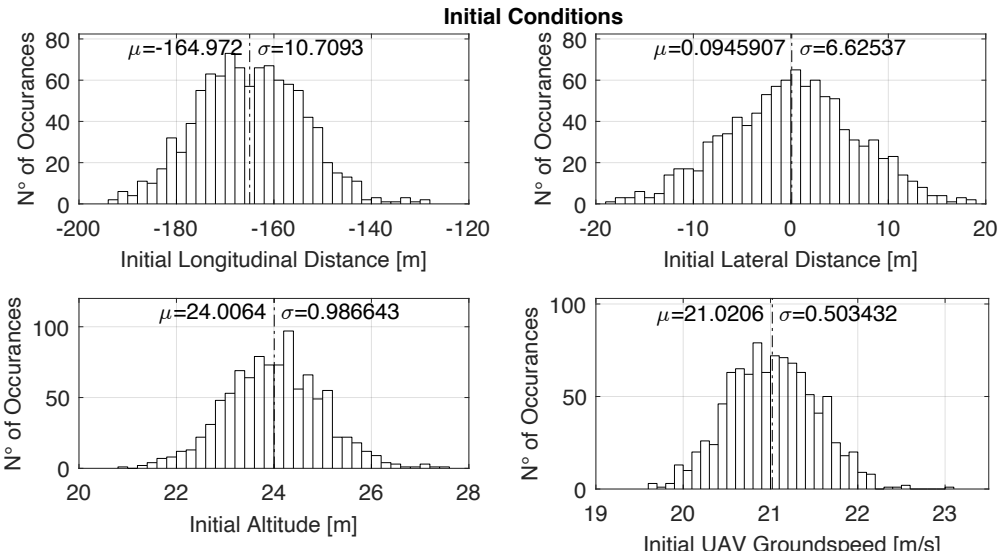

(a) Initial Conditions.

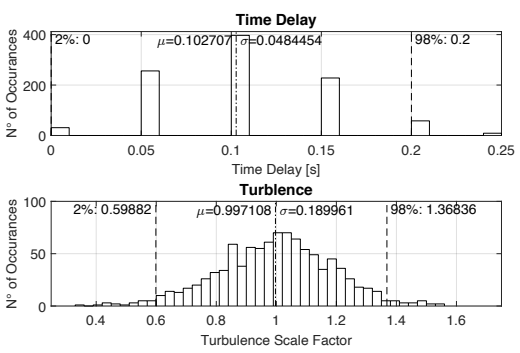

(b) Communication delay and turbulence.

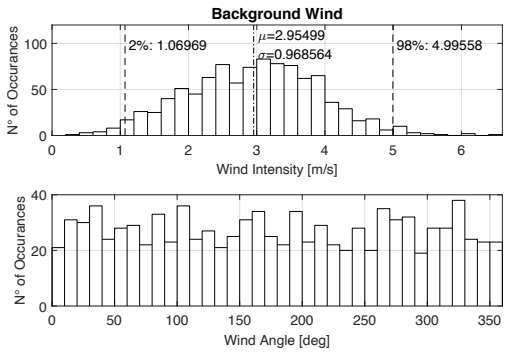

(c) Background wind.

Figure 4.16: Randomly generated inputs for Monte Carlo analysis for landing.

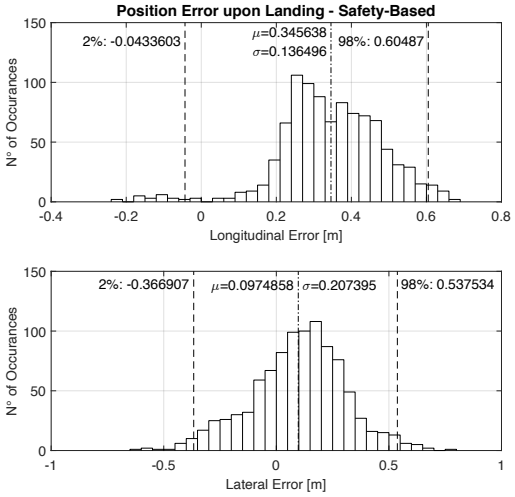

(a) Horizontal position error (safety).

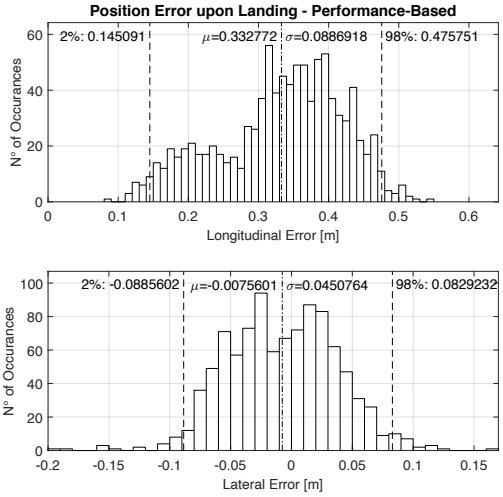

(b) Horizontal position error (performance).

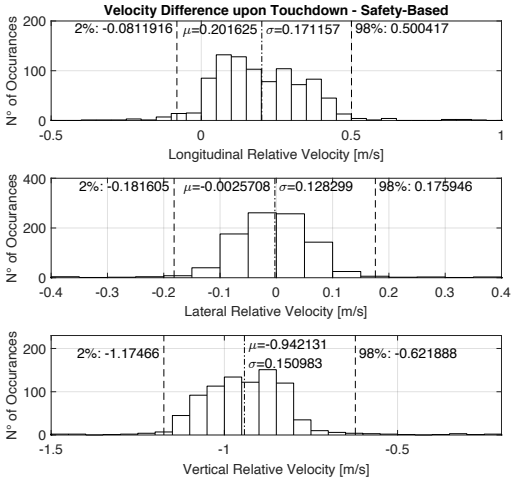

(c) Horizontal velocity error (safety).

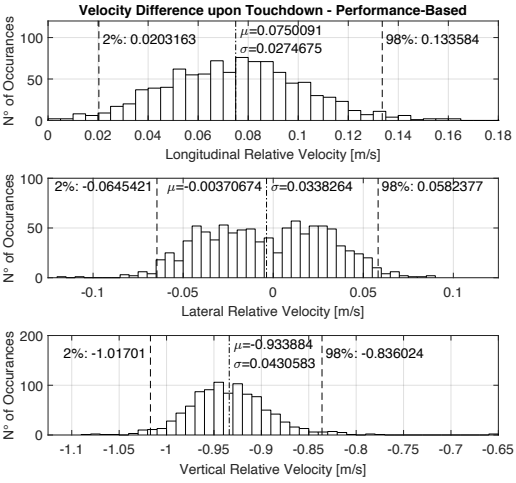

(d) Horizontal velocity error (performance).

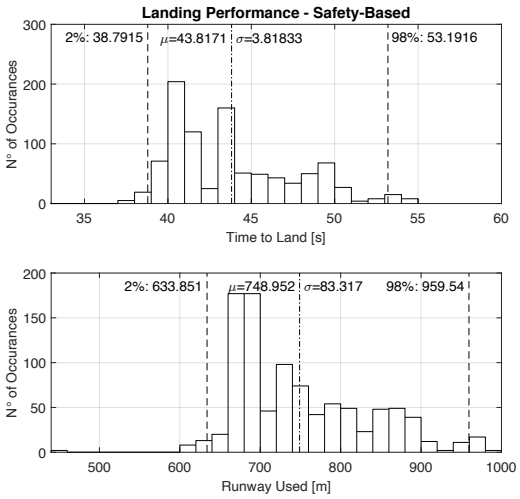

(e) Landing performance (safety).

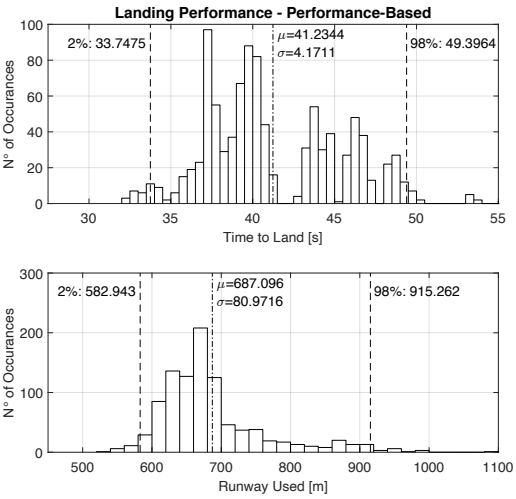

(f) Landing performance (performance).

Figure 4.17: Outputs of the Monte Carlo analysis for landing.

Modeling and Performance Analysis of Elektra 2 Solar at Varying Altitudes

5.1 Preface

In order to analyze the behavior of the Elektra 2 Solar aircraft during its flight to the stratosphere, a dynamic model that gets updated with its current altitude must be created. Since the system identification data is only available for a single point of its entire envelope at this point, no extrapolation from it can be made, as would be suggested by Lee et al. [4]. Therefore, a model based purely on the aircraft's geometry and information from the flight envelope will be developed using VLM. At this point, it is important to set the correct expectations for this step: VLM naturally is not able to produce high fidelity models, such as the system identification process shown in Chapter 3, but it should still serve as a close enough approximation for an initial analysis, which can still provide useful insight into the system behavior with such a wide range of operating conditions.

For the atmospheric data necessary, the standard atmosphere model will be used. Values of relevant quantities used by this model are presented in Figure 5.1a. For missions with Elektra 2 Solar, the calibrated airspeed is controlled, which at sea level is desired to be $20.833 m/s$. This translates to a dynamic pressure of approximately $265.834 Pa$ during the entire flight. Figure 5.1b shows how this translates in terms of true airspeed, Reynolds number and Mach number. To calculate Reynolds number, the mean aerodynamic chord was used as the characteristic dimension. As can be observed in this figure, with this criteria, Mach number has a maximum value of approximately 0.275, and as seen in common literature [31; 32], since this value is lower than 0.3, compressibility effects can be ignored.

First, for the creation of this model, the software packages Athena Vortex Laticce (AVL) [70] and XFLR5 [71] will be used. Once the model has been developed, it will be validated by comparing its performance to that of the data available from the Elektra 2 Solar maneuvers for system identification. Lastly, the model will undergo a detailed analysis of how its parameters change at varying altitudes and what is relevant to be considered for this work and future discussions.

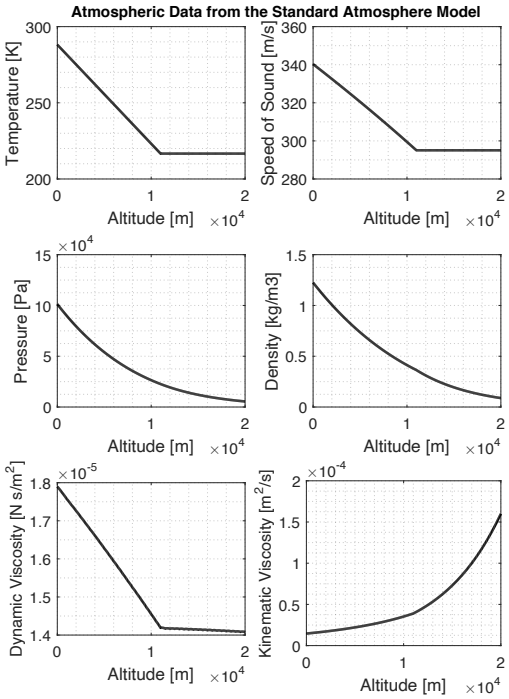

(a) Data from the Standard Atmosphere model.

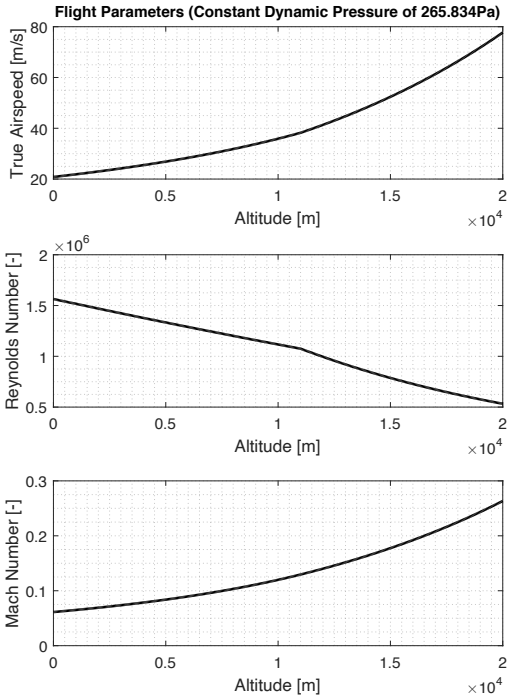

(b) Flight mission envelope conditions.

Figure 5.1: Flight conditions from ground to stratosphere of Elektra 2 Solar.

5.2 Methodology

5.2.1 Model Development

Modeling the aerodynamics of the aircraft using AVL and XFLR5 takes two stages. First, XFLR5 is used to generate the drag polar curves of each airfoil, as well as direct calculation for the airplane of both drag and lift coefficients at the minimum drag condition and lift and pitch moment coefficients at zero angle of attack. After that, with the airfoils' drag polar curves and the same airplane input geometry, AVL is used to calculate the derivatives of the model.

The algebraic equations for the aerodynamic coefficients generated using this method are as follows:

$$C_D = C_{D0} + k_{inddrag} \cdot (C_L - C_{Lmindrag})^2 + C_{D\delta e} \cdot |\delta_e| \tag{5.1}$$

$$C_Y = C_{Y\beta} \cdot \beta + C_{Y\delta a} \cdot \delta a + C_{Y\delta r} \cdot \delta r + \left(\frac{b_{ref}}{2 \cdot V_a}\right) \cdot (C_{Yp} \cdot p + C_{Yr} \cdot r) \tag{5.2}$$

$$C_L = C_{L0} + C_{L\alpha} \cdot \alpha + C_{L\delta e} \cdot \delta e + \left(\frac{c_{ref}}{2 \cdot V_a}\right) \cdot (C_{Lq} \cdot q) \tag{5.3}$$

$$C_l = C_{l\beta} \cdot \beta + C_{l\delta a} \cdot \delta a + C_{l\delta r} \cdot \delta r + \left(\frac{b_{ref}}{2 \cdot V_a}\right) \cdot (C_{lp} \cdot p + C_{lr} \cdot r) \tag{5.4}$$

$$C_m = C_{m0} + C_{m\alpha} \cdot \alpha + C_{m\delta e} \cdot \delta e + \left(\frac{c_{ref}}{2 \cdot V_a}\right) \cdot (C_{mq} \cdot q) \tag{5.5}$$

$$C_n = C_{n\beta} \cdot \beta + C_{n\delta a} \cdot \delta a + C_{n\delta r} \cdot \delta r + \left(\frac{b_{ref}}{2 \cdot V_a}\right) \cdot (C_{np} \cdot p + C_{nr} \cdot r) \tag{5.6}$$

where $k_{inddrag}$ is a constant related to induced drag, calculated as

$$k_{inddrag} = \frac{1}{\pi \cdot \dfrac{b_{ref}^2}{S_{ref}} \cdot osw} \tag{5.7}$$

with osw being Oswald's coefficient.

There are three different types of airfoils present in the Elektra 2 Solar aircraft, which will be hereby referred to simply as Airfoil Type 1, 2 and 3. In terms of the provided geometrical airplane model, it only consists of the wings and the control surfaces; this is done as recommended by both pieces of software, but naturally it leads to less drag than there should be. This error may be lower in HALE aircraft than other types due to the high aspect ratio, but it should still be considered. To compensate for this, in the minimum drag coefficient, an extra factor of 0.033 is added, which was previously estimated by the manufacturer as the resulting drag coefficient of the canopy, gear and other parts of the plane left out of the model.

Aside from geometry, a couple of extra inputs are necessary for each step. Reynolds number must be given for the drag polar curves of airfoil; true airspeed, air density and kinematic viscosity must be given for coefficients at minimum drag and zero angle of attack; and the generated drag polar curves of airfoils and air density must be given for the derivatives. Therefore, by changing these inputs according to their expected values at varying altitudes, as seen in Figure 5.1, one can create separate models for each point of the flight envelope. Using this method, the coefficient derivatives will be calculated for altitudes ranging from $0km$ to $20m$ at steps of $1km$.

5.2.2 Model Validation

The validation of the model can only be done at one point of the flight envelope, that being the one where the system identification maneuvers were done. The model will be allowed to reach a trim point with constant airspeed and altitude equal to that of the experiments, an elevator pulse with the same amplitude and duration of the experiments will be given to initiate a phugoid maneuver, and that response will be compared to the real data. For a quantitative comparison, GOF and TIC will be calculated, as well as phugoid period and damping for the use of FAA's standards [55].

Although this validation can only be done at one point in the lower altitude range, both AVL and XFLR5 generally produce better results at lower Reynolds numbers [70; 71], and since Reynolds number decreases with altitude in this application, one can conclude that, if the model is shown to be adequate at the available validation point, it should remain to be so for higher altitudes.

5.2.3 Model Analysis

A few key points can be analyzed from the resulting model. First, from the control strategy, as altitude increases, so does airspeed, and therefore, in terms of dynamics, the phugoid period should also increase [72]; examining said effect is relevant for future system identification maneuvers, since that information is paramount to data gathering, as explained in Section 2.2. Second, as flight conditions are changing considerably, analyzing how much drag changes is also relevant for future flight missions, since that affects the aircraft's energetic performance, which is a vital point of HALEs considering the required efficiency of them. Finally, system identification can be done on top of the VLM model. This can give insight into how the parameters of the identified model are expected to change as altitude increases, and if there are any important terms which are currently not being taken into consideration.

For the first point, a trim condition must be found for each altitude and airspeed pair; with that, an elevator pulse can be used as input, as any system identification maneuver, and the response can be then analyzed.

For the second point, at each trim condition found, the drag can be directly calculated using the states. Given that the dynamic pressure is constant, the fact that Reynolds number is decreasing with altitude is an indicative that the drag should increase, since Reynolds number essentially represents a ratio between inertial forces and viscous forces, and as such, when it goes down, it means the viscous forces are getting stronger relative to the inertial ones.

Lastly, with the phugoid maneuvers done for the first point, the system identification process can be done just as it normally would with the data from the simulation. Only of note is that since the data comes directly from a simulation itself, the data compatibility check is unnecessary, as there are no biases or drifts already.

5.3 Results

5.3.1 Partial Coefficients

Figures 5.2, 5.3 and 5.4 show the drag and lift coefficients for the airfoil sections of Elektra 2 Solar. Noteworthy are the coefficients of drag at the minimum drag condition, which considerably increase for lower Reynolds numbers; Airfoil Type 1 has a 97.87% increase, Type 2 has a 166.29% increase, and Type 3 has a 154.64% increase. Furthermore, as a symmetric airfoil section, Type 1 has almost identical values of drag coefficient for both negative and positive stall, and almost opposite values for lift coefficient in the same conditions.

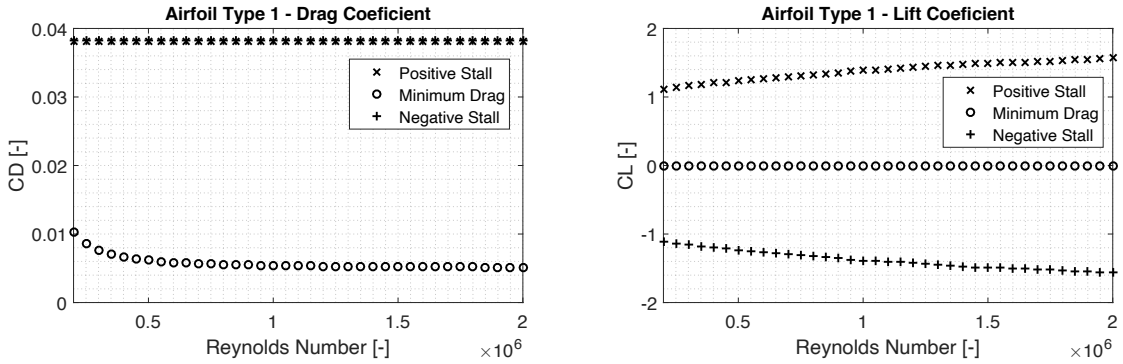

Figure 5.2: Drag and lift coefficients at varying Reynolds Numbers of the Airfoil Type 1 section.

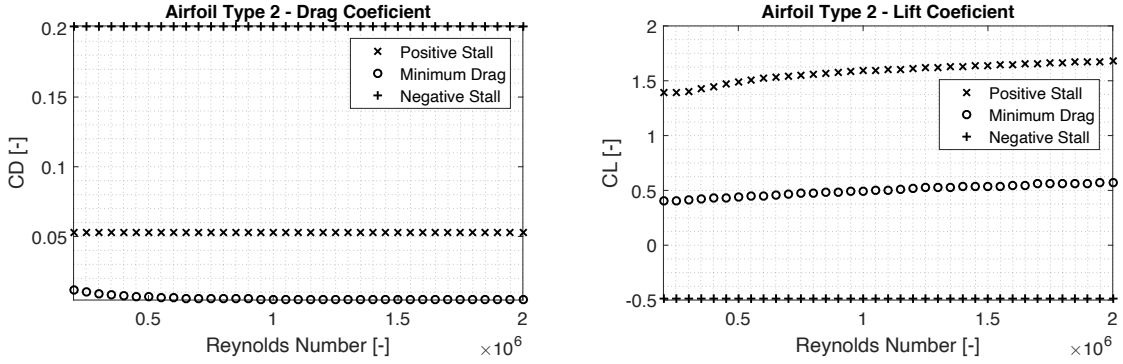

Figure 5.3: Drag and lift coefficients at varying Reynolds Numbers of the Airfoil Type 2 section.

Figure 5.5 shows the results for coefficients at the minimum drag and zero angle of attack conditions. Again of notice are the coefficients at minimum drag, where the drag coefficient increases by 18.52% and the lift coefficient decreases by 11.28%.

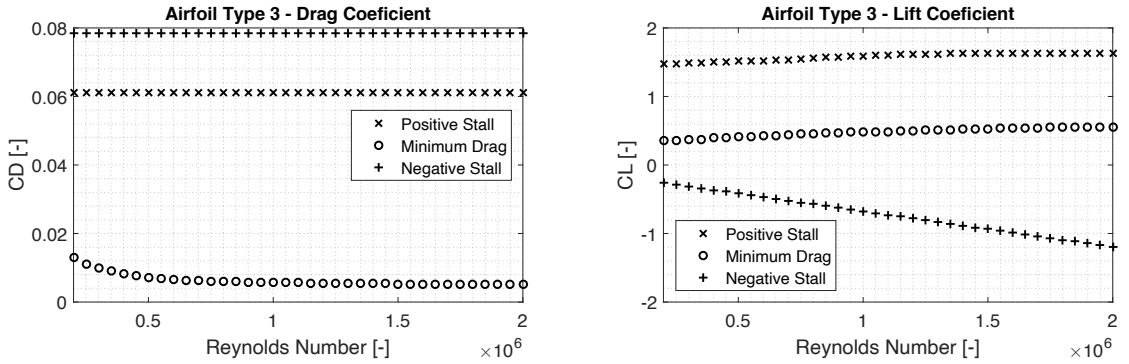

Figure 5.4: Drag and lift coefficients at varying Reynolds Numbers of the Airfoil Type 3 section.

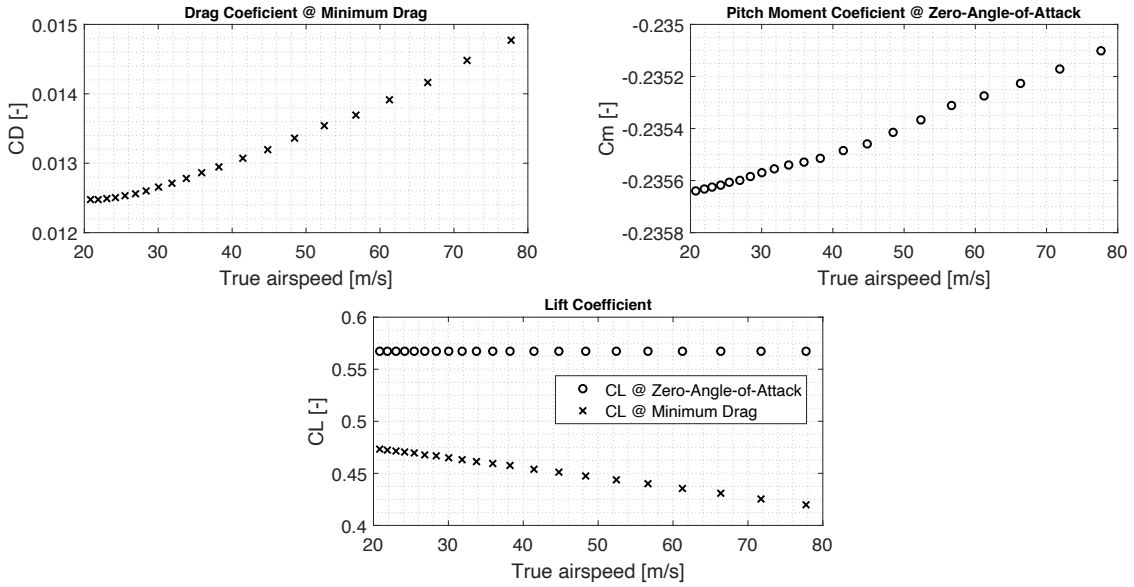

Figure 5.5: Coefficient derivatives from XFLR5 of the plane model.

5.3.2 Resulting Aerodynamic Derivatives

The model derivatives are presented in Figures 5.6 to 5.11, and the results are now represented in terms of altitude. Most derivatives do not change their values considerably at different altitudes, with the ones showing the biggest changes being those related to drag.

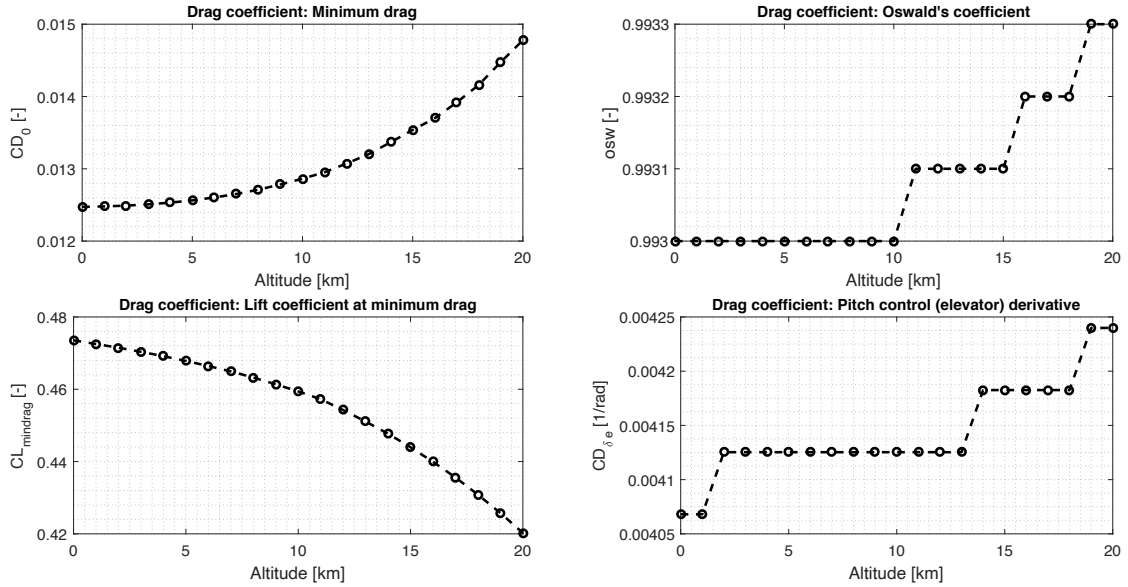

Figure 5.6: Drag derivative coefficients of Elektra 2 Solar.

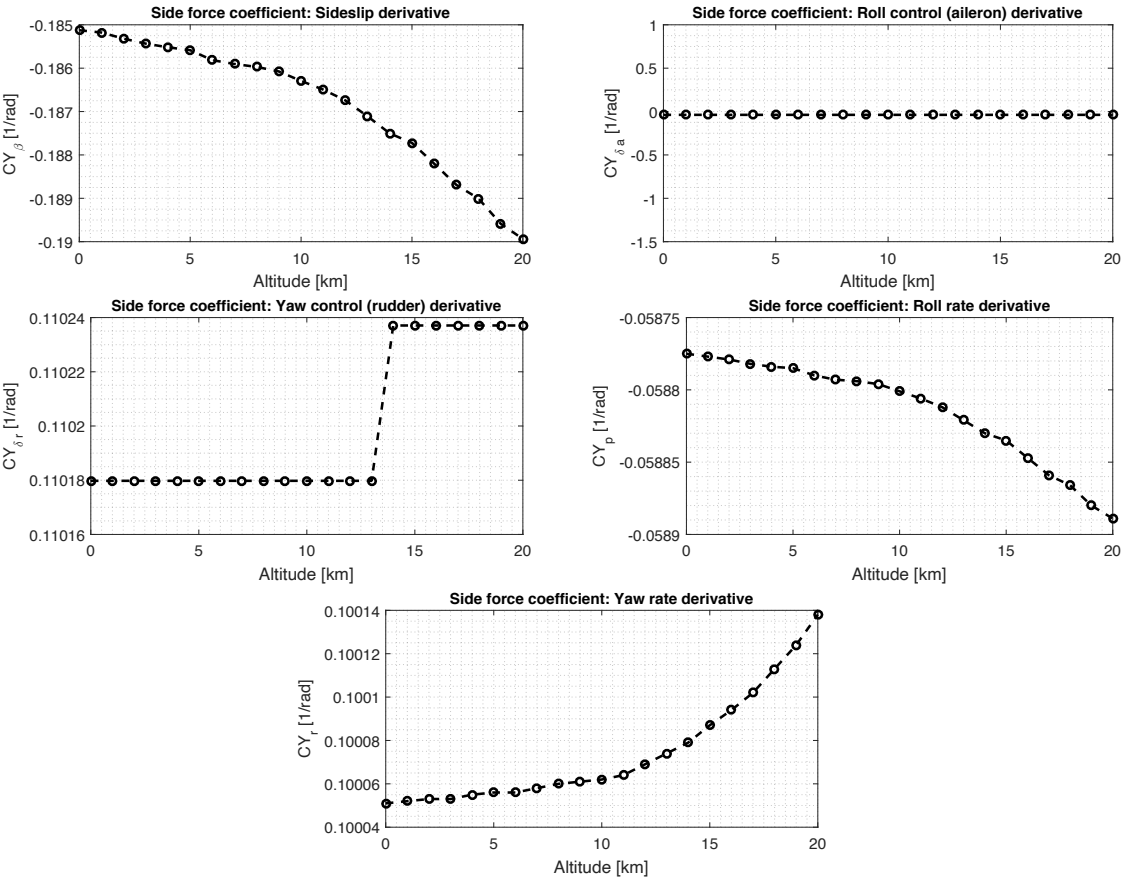

Figure 5.7: Side force derivative coefficients of Elektra 2 Solar.

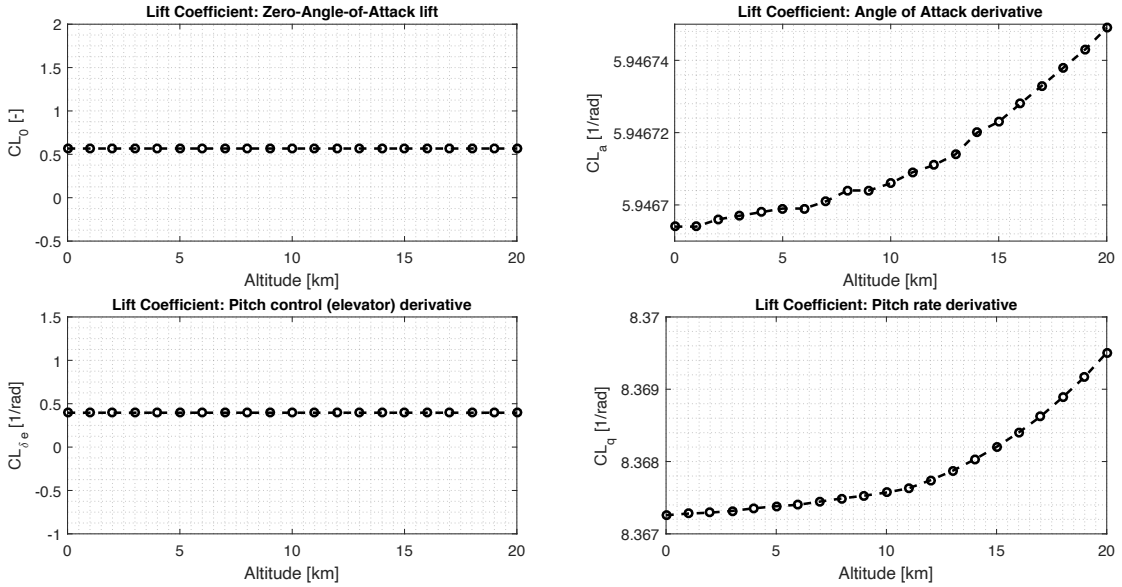

Figure 5.8: Lift derivative coefficients of Elektra 2 Solar.

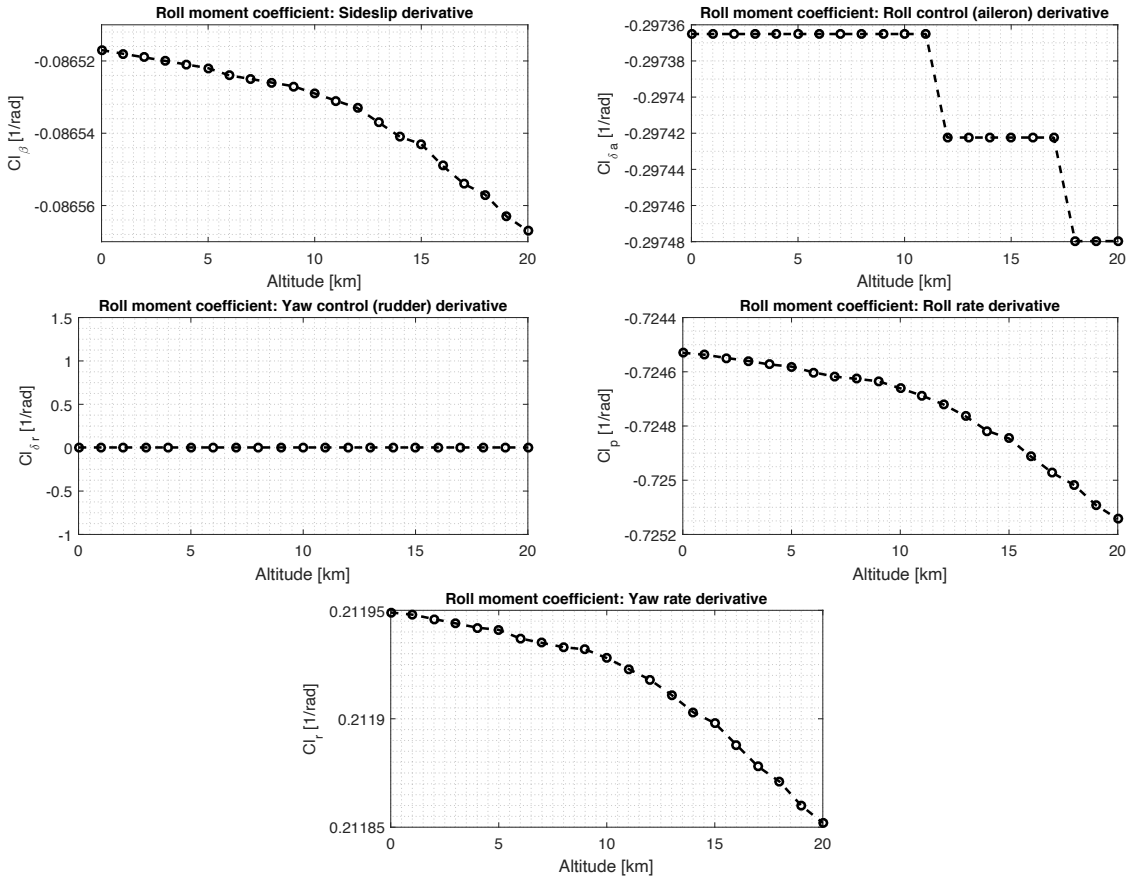

Figure 5.9: Roll moment derivative coefficients of Elektra 2 Solar.

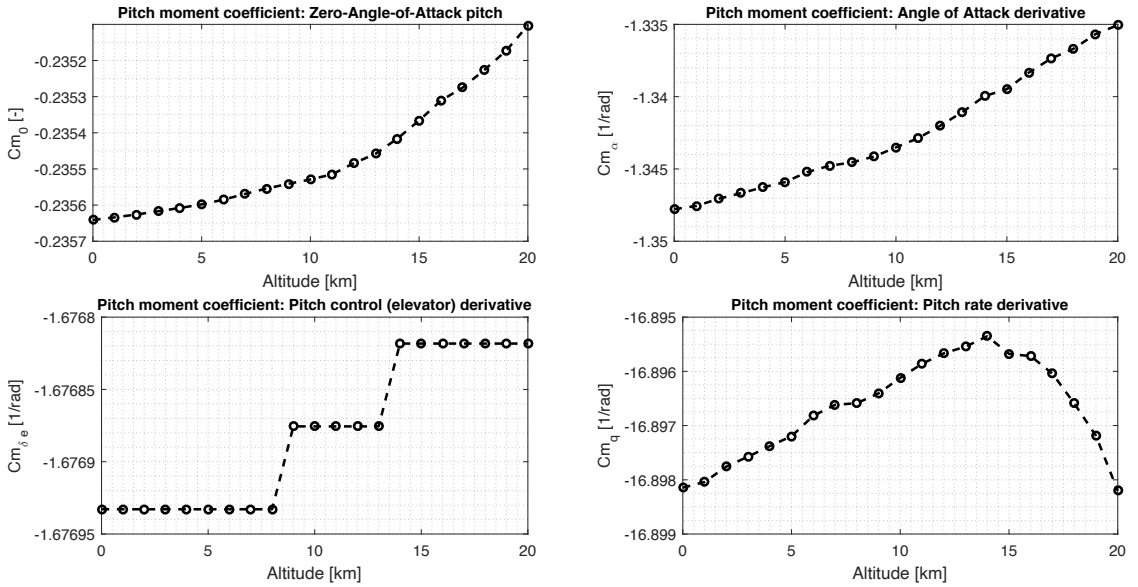

Figure 5.10: Pitch moment derivative coefficients of Elektra 2 Solar.

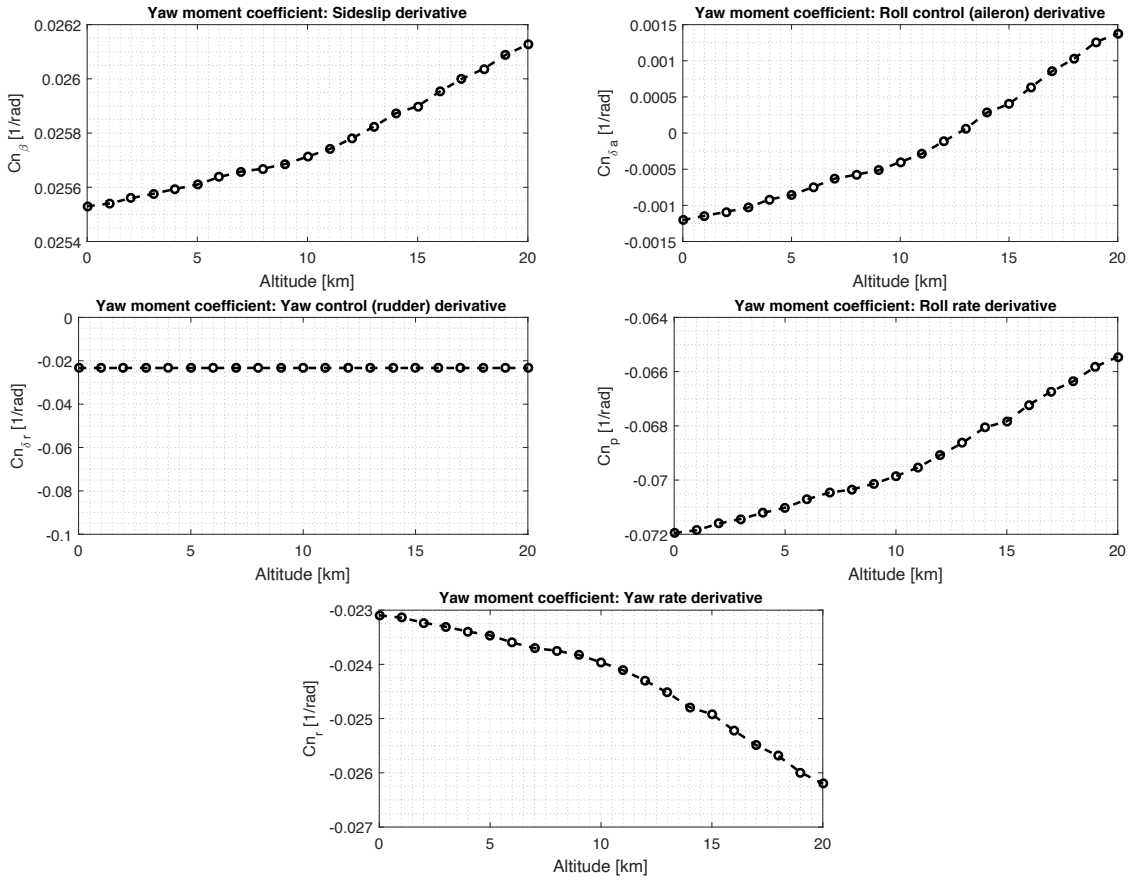

Figure 5.11: Yaw moment derivative coefficients of Elektra 2 Solar.

5.3.3 Validation

Figure 5.12 shows how the phugoid of the VLM model compares to the experiments in terms of airspeed, and Table 5.1 presents the the results in terms of period and dampening.

Criteria	VLM Model	Experiment	Error (Abs.)	Error (Rel.)
Period	15.73s	20.61s	4.88s	23.66%
Damping	0.0372	0.0663	0.0291	43.88%

Table 5.1: Comparison of phugoid characteristics between VLM model and average of flight experiments.

As can be observed, this does not comply with FAA's standards of high fidelity [55], though the amplitude of the observed oscillations is very similar. Overall, this maneuver presents in terms of statistical measures $GOF = -2.2140$ and $TIC = 0.0892$; the low TIC values suggests a good agreement between the data and the model.

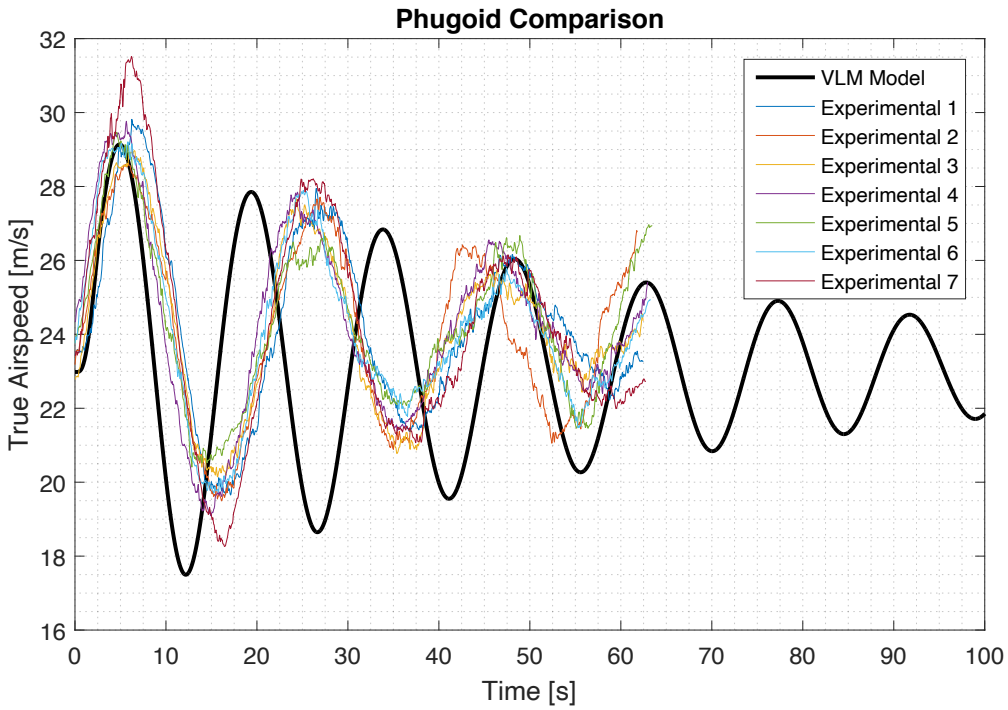

Figure 5.12: True airspeed during phugoid maneuver.

5.3.4 Model Analysis

In terms of the phugoid period, 5.13 shows how it increases almost linearly with the true airspeed of the aircraft. By the time the aircraft arrives at $20km$, the phugoid period is already 2.4 times its initial value.

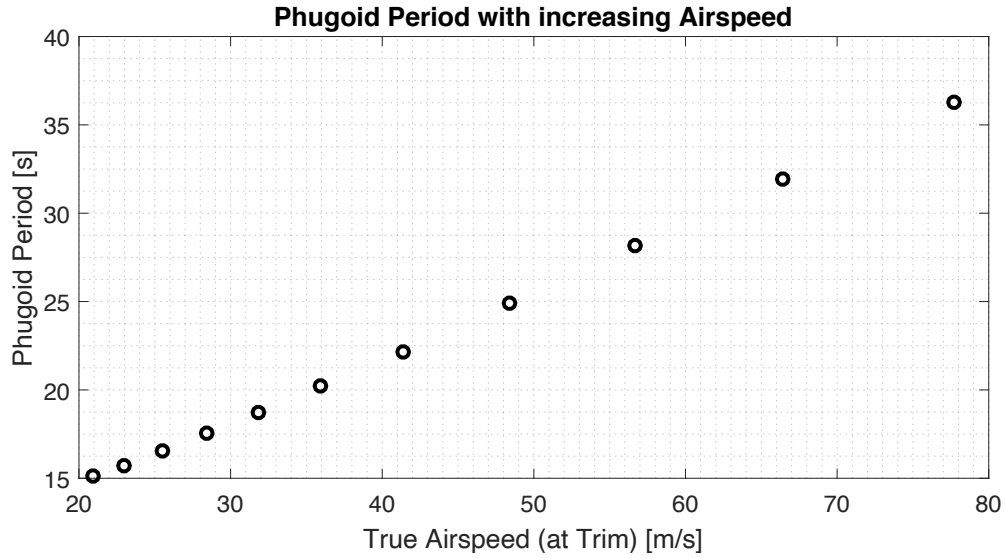

Figure 5.13: Phugoid period with increasing true airspeed.

Figure 5.14 illustrates the increase in drag in higher altitudes. From the initial flight conditions, drag can increase up to 16.56% when going all the way up to $20km$, with said effect becoming more accentuated from $12km$ forward.

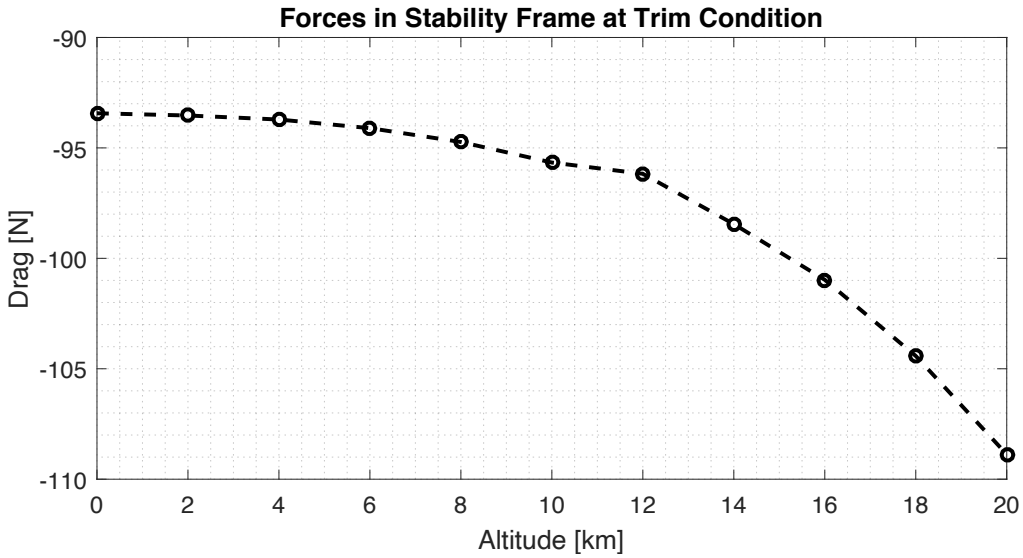

Figure 5.14: Drag force at the trim condition in different altitudes.

In terms of system identification done with the VLM model data for each altitude, it was first done with the proposed minimal linear model from Section 3.4.1. The

results for identified parameters in are shown in Figures 5.15,5.16 and 5.17. However, this presented a couple of problems.

First, in Figure 5.16, one can see the value of Z_q is varying considerably, even changing sign twice along the climb to $20km$. Such variance is generally a sign of over-fitting, and doesn't match it's physical interpretation. Similar comments can be made about X_u, which becomes bigger than zero at $16km$.

Furthermore, the statistical measures can be seen in Figures 5.18 and 5.19, and it is possible to observe all of them start significantly worsening around and after the $12km$ mark. By the $20km$ identification, pitch rate q has a TIC measure of 0.2217, which is already getting close the established threshold of 0.3, and R^2 of the forces in longitudinal direction has a value of 0.4518. This indicates the model may not be accurate enough for higher altitudes, and some terms may need to be added.

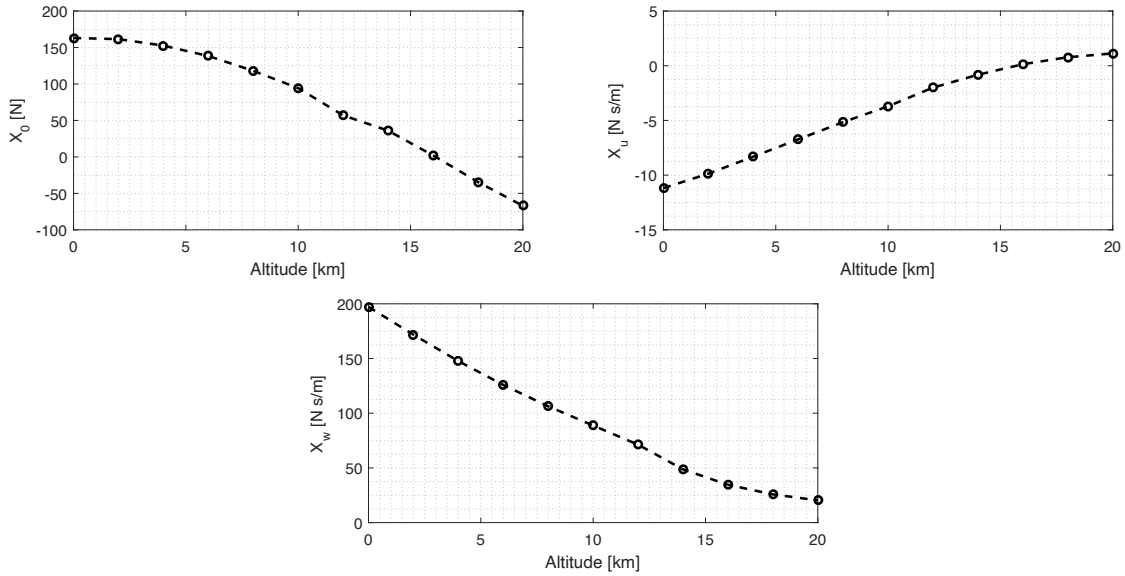

Figure 5.15: Longitudinal aerodynamic derivatives in the linear identification of the VLM model of Elektra 2 Solar.

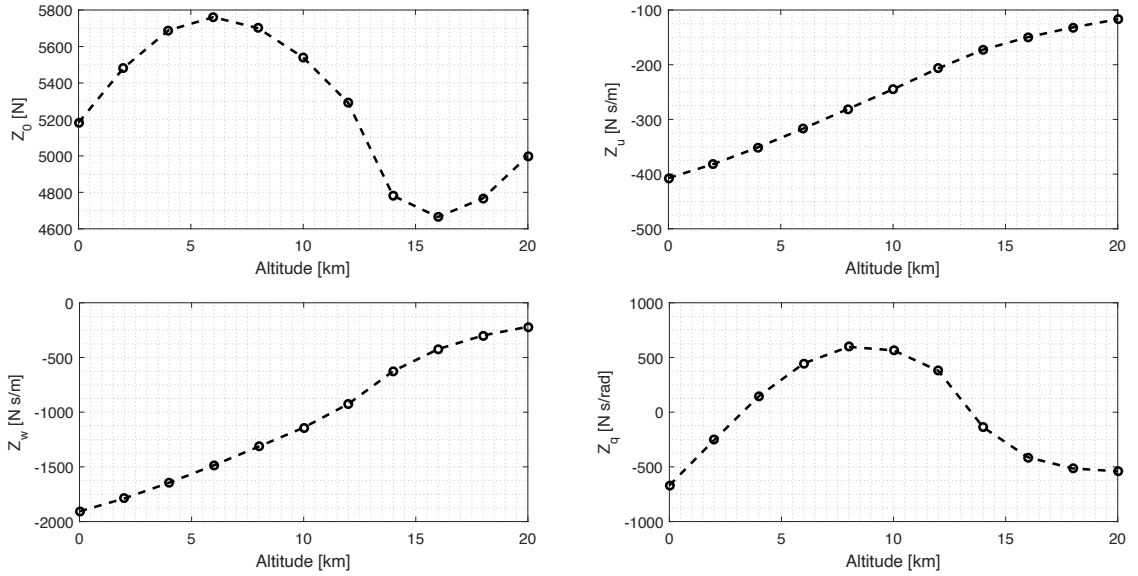

Figure 5.16: Vertical aerodynamic derivatives in the linear identification of the VLM model of Elektra 2 Solar.

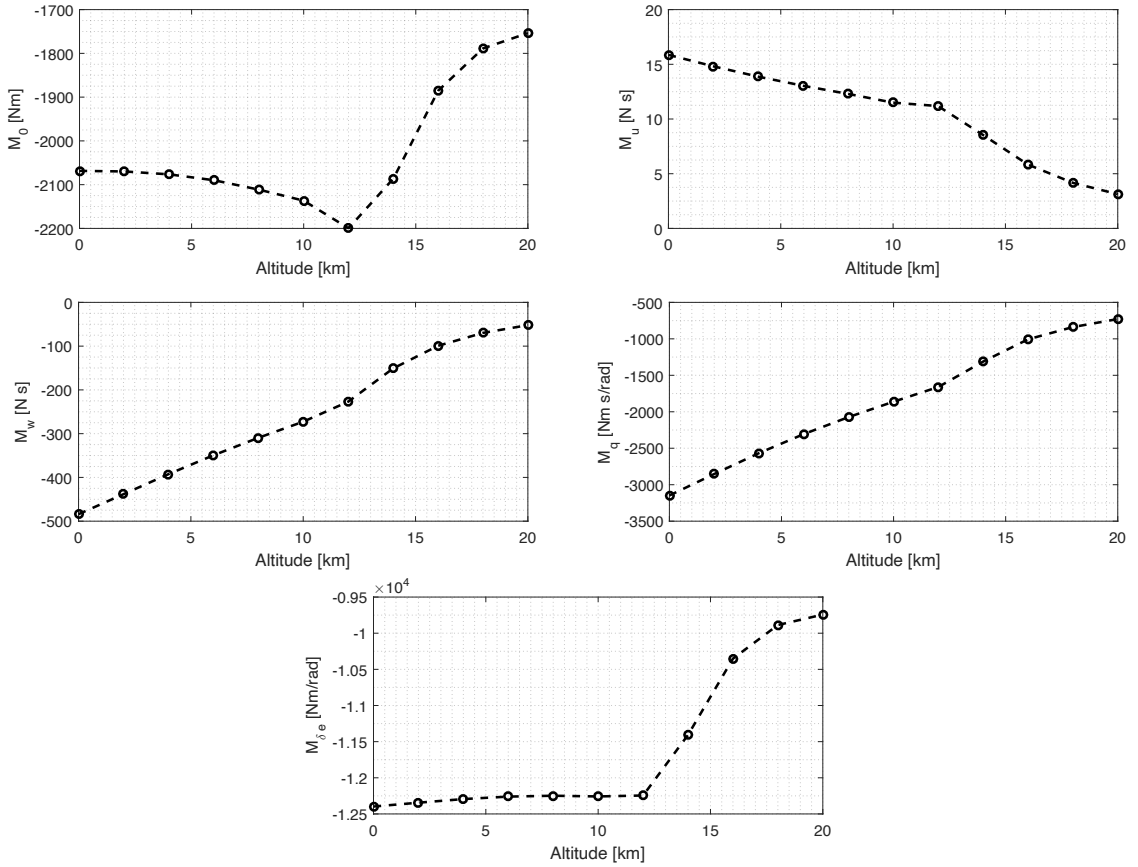

Figure 5.17: Pitch moment aerodynamic derivatives in the linear identification of the VLM model of Elektra 2 Solar.

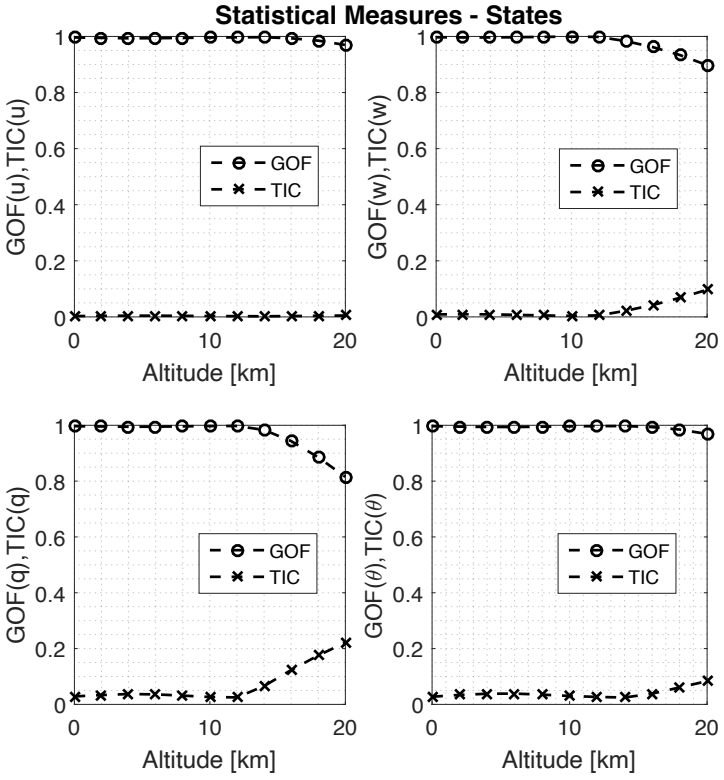

Figure 5.18: Statistical measures for the states in the linear identification of the VLM model of Elektra 2 Solar.

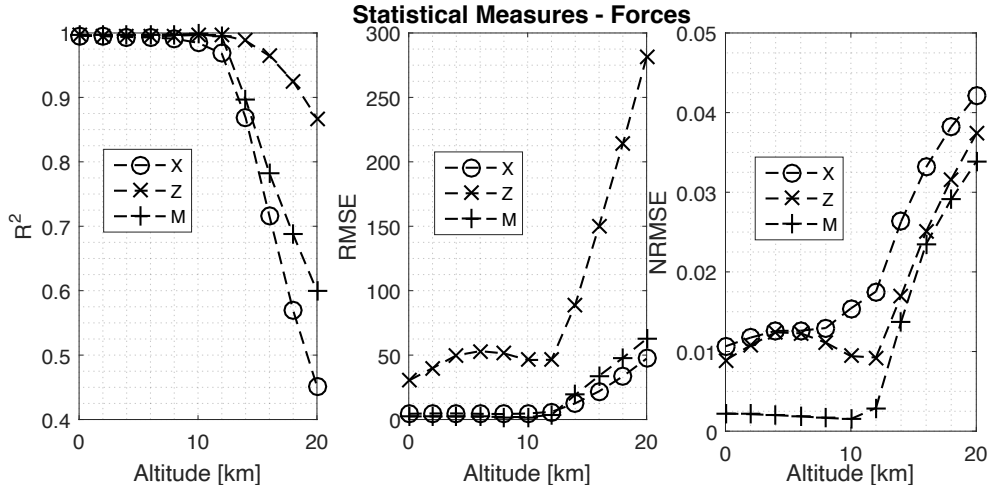

Figure 5.19: Statistical measures for the forces and moment in the linear identification of the VLM model of Elektra 2 Solar.

After analysis, a non-linear system of equations containing terms related to w^2 was chosen, while also dropping the Z_q term. This means the nonlinear equations become:

$$X = X_0 + X_u \cdot u + X_w \cdot w + X_{w^2} \cdot w^2 \tag{5.8}$$
$$Z = Z_0 + Z_u \cdot u + Z_w \cdot w + Z_{w^2} \cdot w^2 \tag{5.9}$$
$$M = M_0 + M_u \cdot u + M_w \cdot w + M_{w^2} \cdot w^2 + M_q \cdot q + M_{\delta e} \cdot \delta e \tag{5.10}$$
$$\tag{5.11}$$

The results from using this nonlinear model are shown in Figures 5.20, 5.21 and 5.22. As can be seen in Figures 5.23 and 5.24, the problems related to the deprecation of results at higher altitudes is eliminated, with TIC values for all states below 0.04 at all points, and and R^2 of 0.89 for the longitudinal forces at $20km$. For heights lower than $10km$, the w^2 terms all show behavior which is characteristic of over-fitting, which is expected, since for these lower altitudes the linear model was clearly enough, but for higher altitudes, their behavior becomes much more standard.

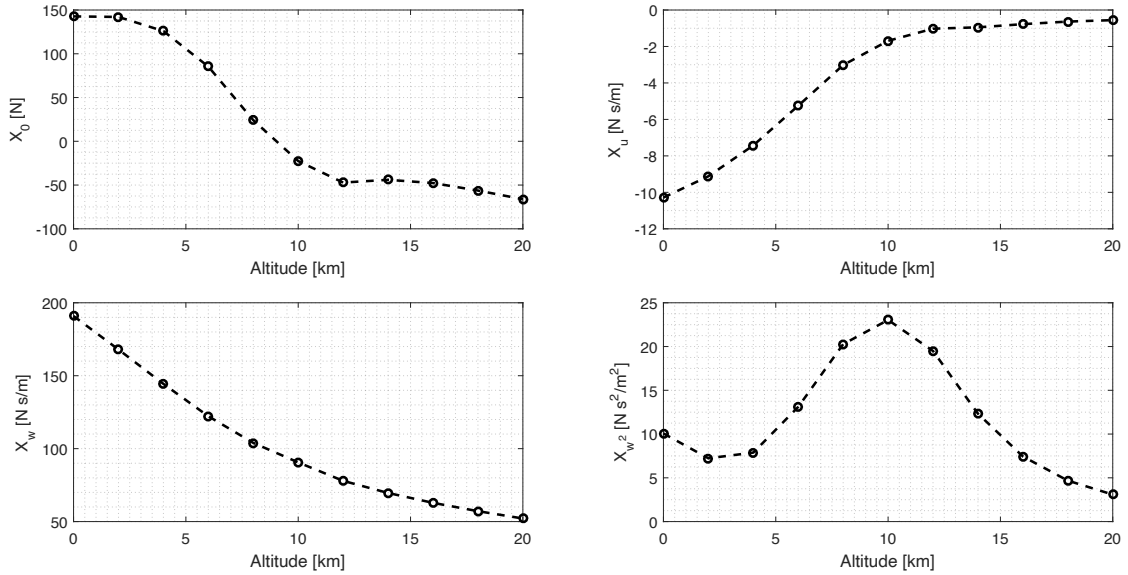

Figure 5.20: Longitudinal aerodynamic derivatives in the nonlinear identification of the VLM model of Elektra 2 Solar.

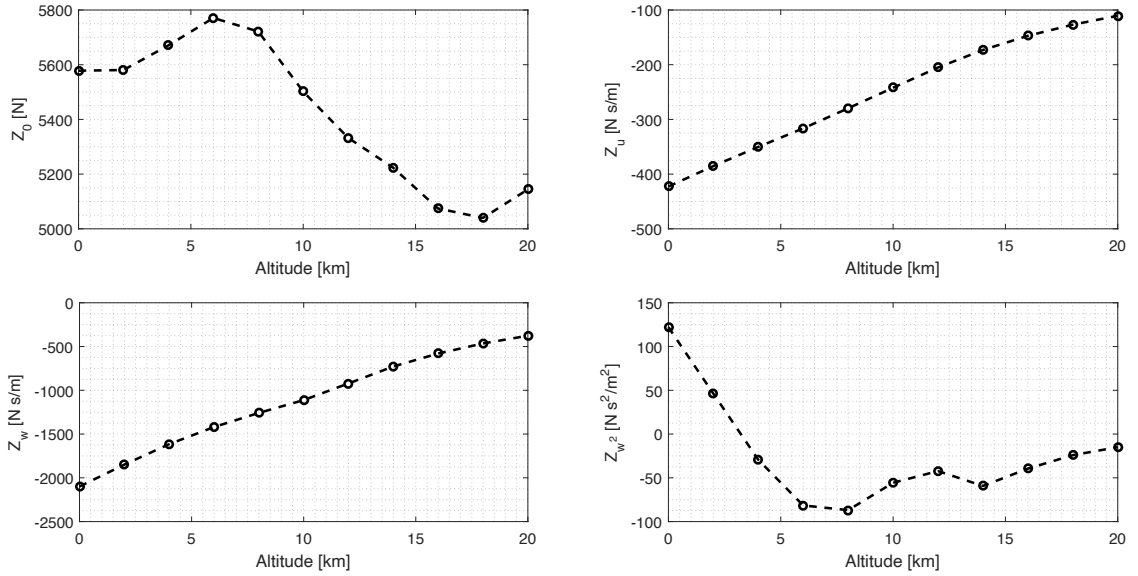

Figure 5.21: Vertical aerodynamic derivatives in the nonlinear identification of the VLM model of Elektra 2 Solar.

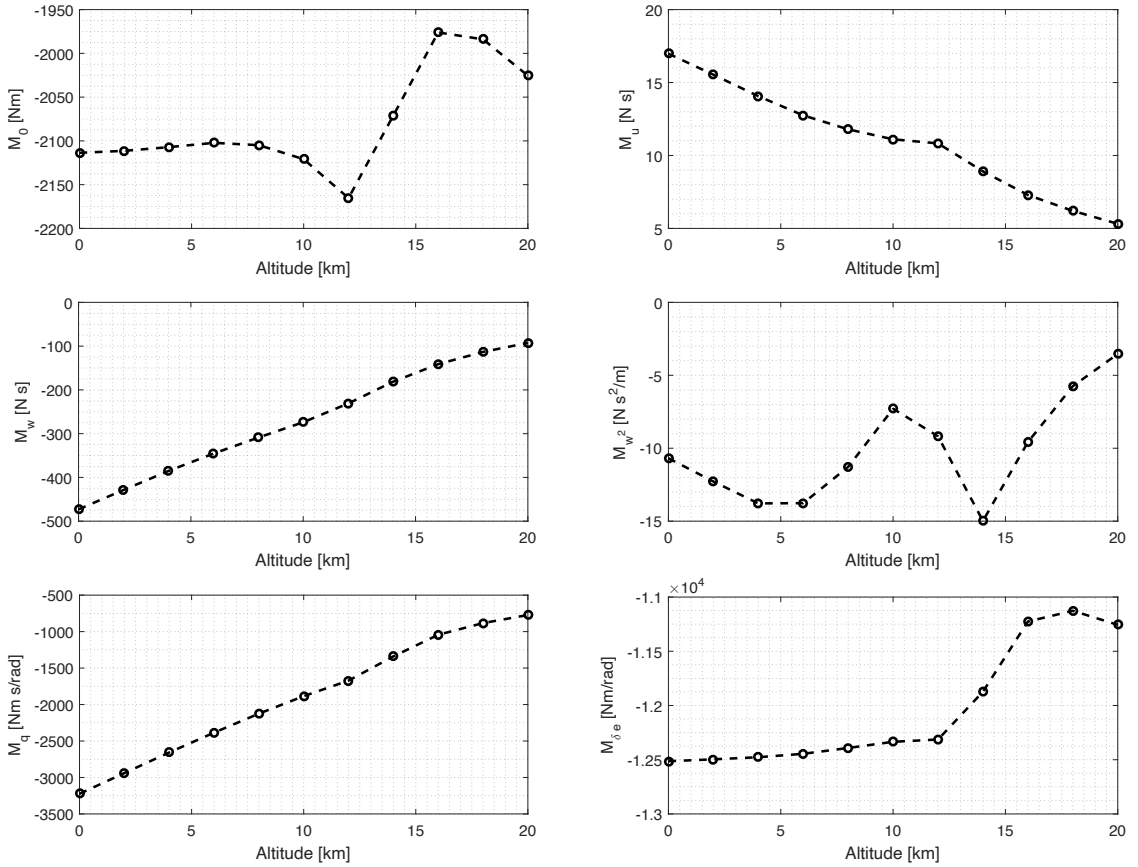

Figure 5.22: Pitch moment aerodynamic derivatives in the nonlinear identification of the VLM model of Elektra 2 Solar.

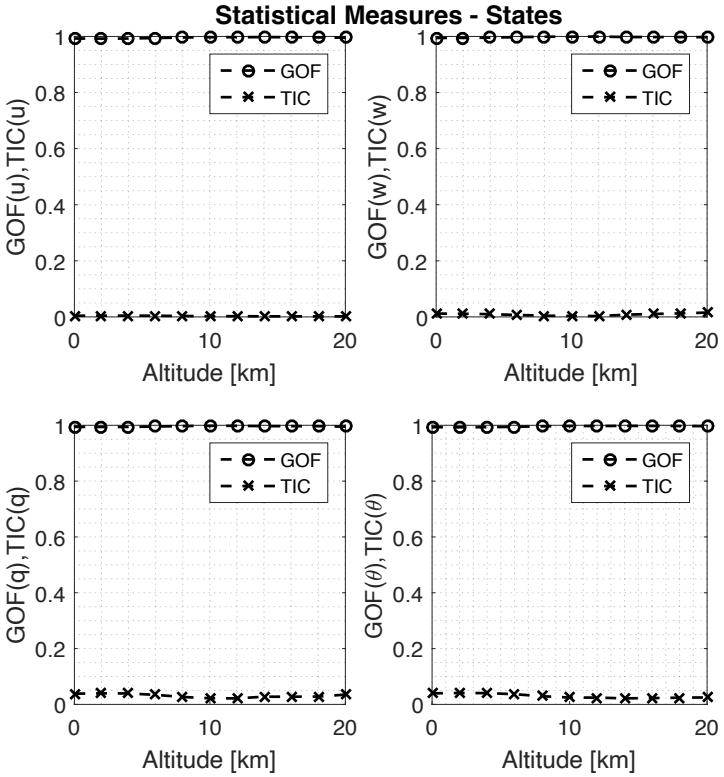

Figure 5.23: Statistical measures of the states in the nonlinear identification of the VLM model of Elektra 2 Solar.

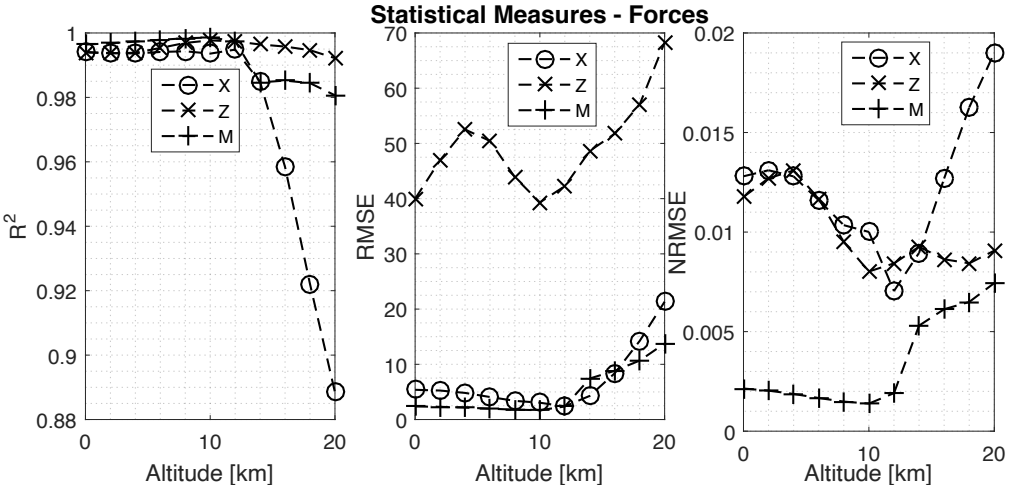

Figure 5.24: Statistical measures of the forces in the nonlinear identification of the VLM model of Elektra 2 Solar.

Gain Scheduling for Stratospheric Flight

6.1 Preface

In control theory, gain scheduling is an approach that involves changing the controller gains when the system changes between different operating conditions, where each set of gains is tuned to provide satisfactory performance at their respective point. According to Astrom et al. [64], this is a common strategy employed in high-performance aircraft, where the controller gains are set to vary depending on factors such as dynamic pressure, Reynolds number and Mach number. Examples for aircraft and missiles can be found on Cook [31] and Zipfel [32]. When it comes to HALE aircraft, Barbosa et al. [73] have successfully taken both linear interpolation and fuzzy gain scheduling approaches to stabilize a flexible X-HALE aircraft after instabilities were observed when varying its velocity during a coordinated turn.

Using the model developed in Chapter 5 and the same TECS controller gains used in the real flight of Elektra 2 Solar, as presented in Table 4.1, one can obtain at lower altitudes the step responses shown in Figure 6.1. The system is stable and shows no apparent issues, even if the performance is not optimal.

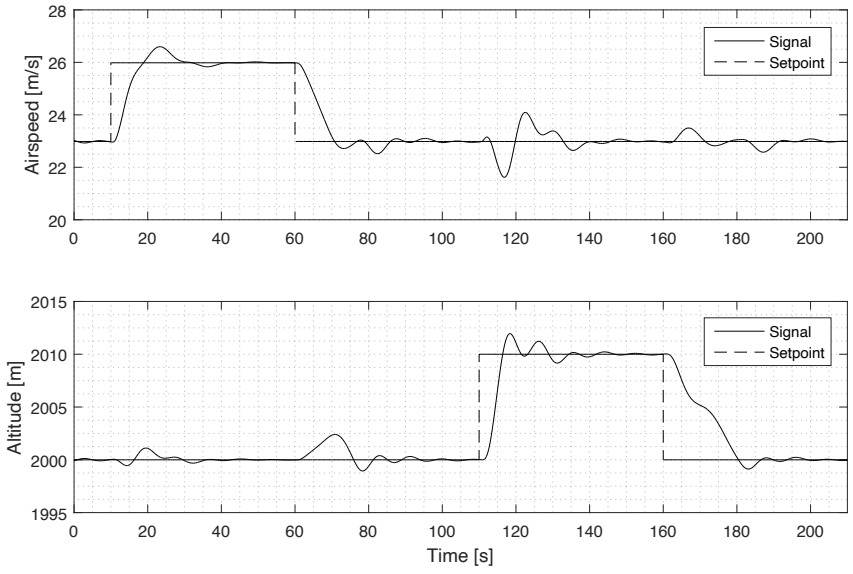

Figure 6.1: System response to steps in airspeed and altitude using flight gains and VLM model.

However, as the aircraft goes higher, the system becomes progressively more unstable, with oscillations starting to be present at around $8km$ and increasing from there. Figure 6.2 illustrates this behavior. For a direct comparison, the pulse given to airspeed and altitude are always of $3m/s$ and $10m$ in amplitude respectively, and the plots are made subtracting the initial state of both airspeed and altitude setpoints,

which will be hereby referenced as a "zero-offset" plot. This allows all responses to be seen together throughout different operating points.

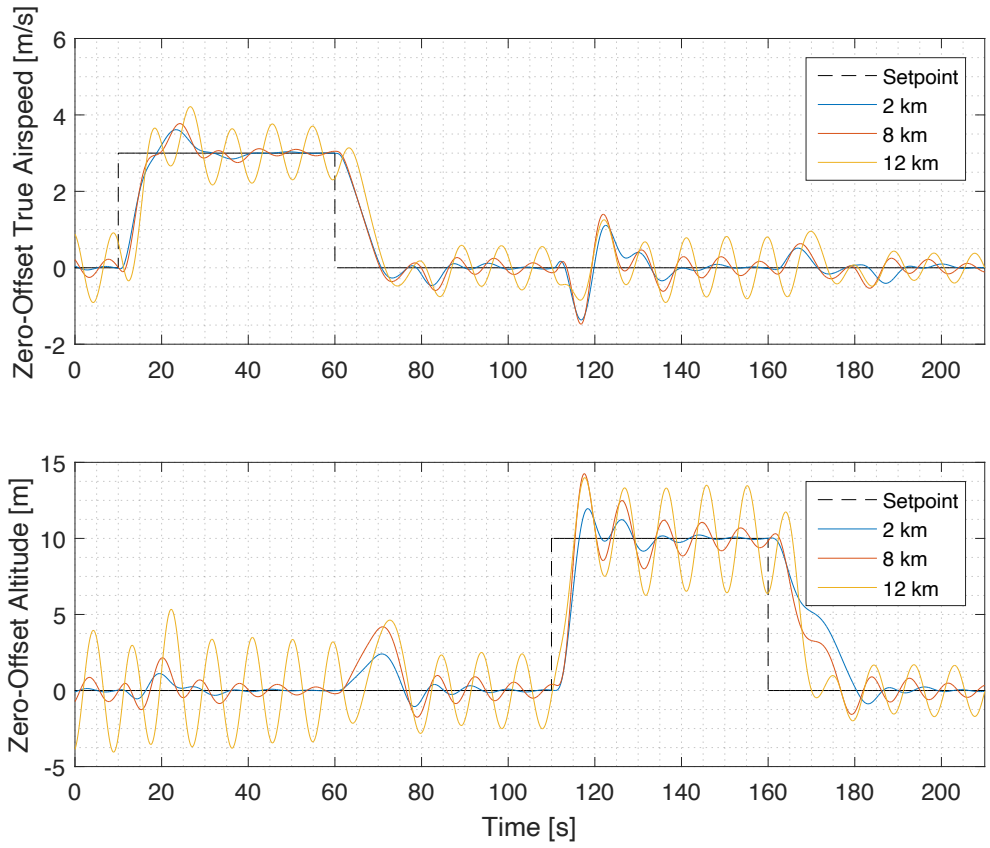

Figure 6.2: System becomes progressively more unstable at higher altitudes with constant controller gains.

To deal with these instabilities, a gain scheduling strategy will now be developed. The controller gains will be analyzed to determine which are the most relevant to suppress the observed unstable behavior, and then an optimization scheme will be defined to automatically find the optimal values of the selected gains for different altitudes.

6.2 Methodology

The developed VLM models of Elektra 2 Solar from Chapter 5 will be used to simulate the aircraft at varying altitudes. One of the most important goals to be achieved here is to be as minimalistic in this approach as possible, and as such, one must first determine a minimal set of controller gains that must be changed from one operating point to another in order to keep the system stable, and then change those gains as little as possible.

To determine the gains that should be scheduled, a sensitivity analysis of all TECS controller gains is done in the altitudes of $10km$ and $20km$, which were chosen for rep-

resenting the middle of the flight envelope and the end goal, and the base controller gains used as reference are the gains used in-flight by Elektra 2 Solar. In the first analysis case, the gains will be individually varied by 25% of their original value, and on the second one, by 50%. With these responses, through a simple qualitative investigation, one can determine which gains to choose as design variables for optimization and scheduling.

Then, for choosing the appropriate values of the gains at each altitude, an optimization scheme must be defined. At every point a pulse of $3m/s$ for $50s$ is commanded in airspeed, followed by a pulse command of $10m$ for $50s$ in altitude, as shown in Figures 6.1 and 6.2. Based on the aircraft response, an objective function is calculated and the optimization can proceed. This process is repeated at each altitude. As for the objective function definition, two different approaches will be considered.

In the first approach, a reference system step response (for both airspeed and altitude) is defined based on the low altitude response, as shown in Figure 6.1, and as cost the IAE between the current step response and the reference one is used. In essence, therefore, this method aims to keep the closed-loop system response as invariable as possible through the flight envelope. Some other alternatives for cost were considered, such as using the poles of the linearized system or using the dynamic parameters (such as time constant, damping, among others) and using as cost function the difference between those and and the reference ones, but the curve matching method was easier to implement and had better results. Furthermore, an additional cost is considered related to the changes of the values of the controller gains; one of the goals is to kept the changes in gains as small as possible, and this cost reflects that. Overall, the cost function for the "constant step response" method can be written as:

$$J = f(IAE(y_{ref}, y), |K_X - K_{X,i-1}|) \tag{6.1}$$

where y represents both airspeed and altitude responses, K_X represents any of the gain chosen as design variable, and $K_{X,i-1}$ represents the value of the optimized gain in the previous altitude.

The second approach instead aims to optimize for performance at all altitudes, following the same costs and criteria as the controller design presented in Section 4.3. The only added cost is the changes in values of the gains between altitudes $|K_X - K_{X,i-1}|$.

6.3 Results

6.3.1 Sensitivity Analysis

First, the analysis at the $10km$ mark was done. The results are shown in Figures 6.3 to 6.11. Overall, K_θ is shown to have the biggest influence, whereby increasing its value significantly improved the results. This is followed by K_q, K_h, KTI and KEI, which resulted in less oscillations by being reduced; the same can be said about K_{Va}, though to a lesser extent. $K_{i,\theta}, K_{thr}, K_{i,thr}, K_{FF}$ are shown to have very little to no influence.

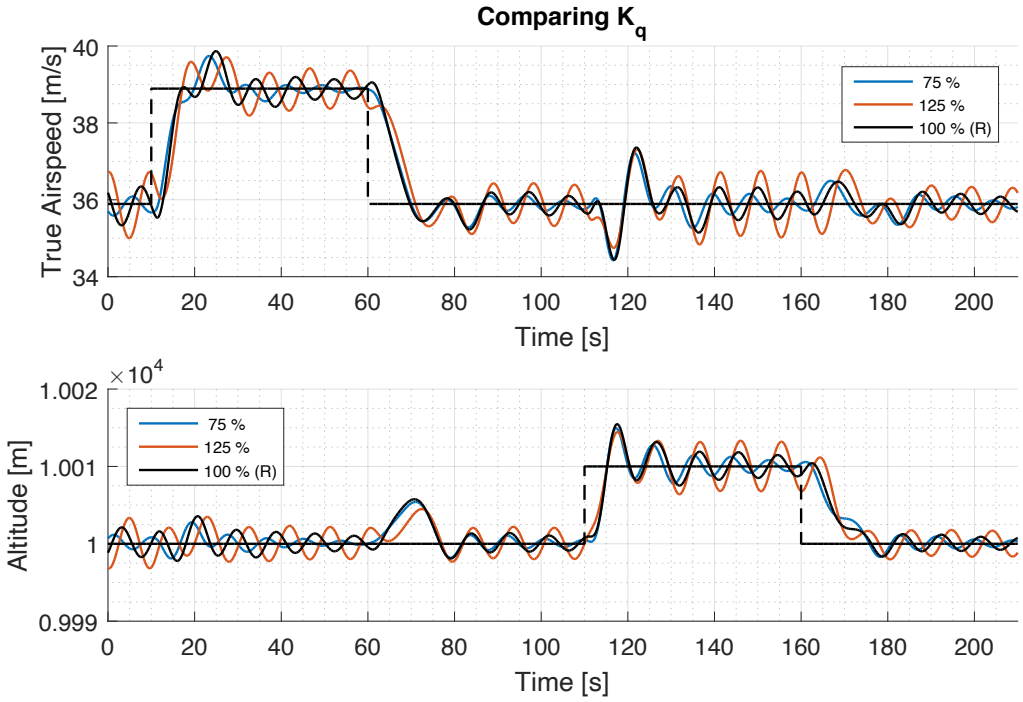

Figure 6.3: Sensitivity Analysis at 10km - K_q.

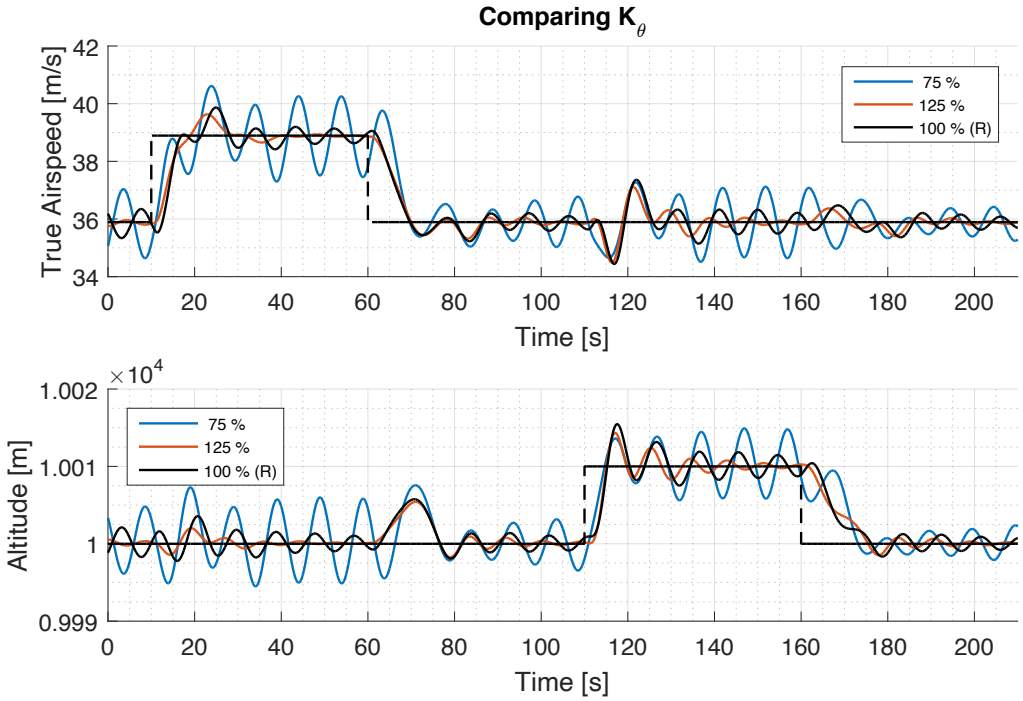

Figure 6.4: Sensitivity Analysis at 10km - K_θ.

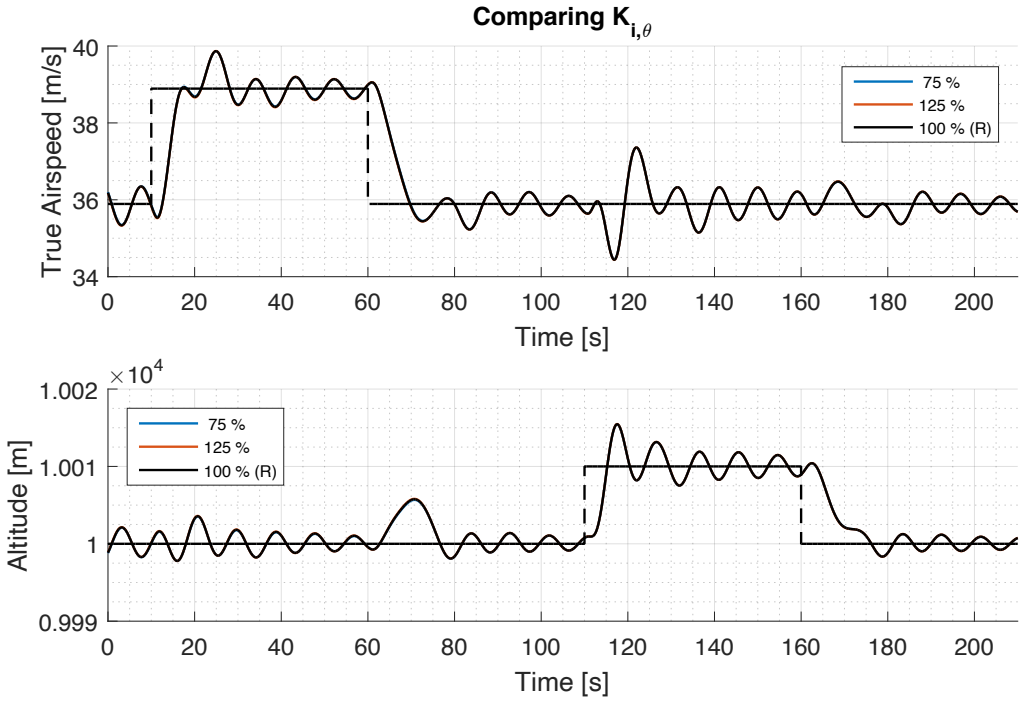

Figure 6.5: Sensitivity Analysis at 10km - $K_{i,\theta}$.

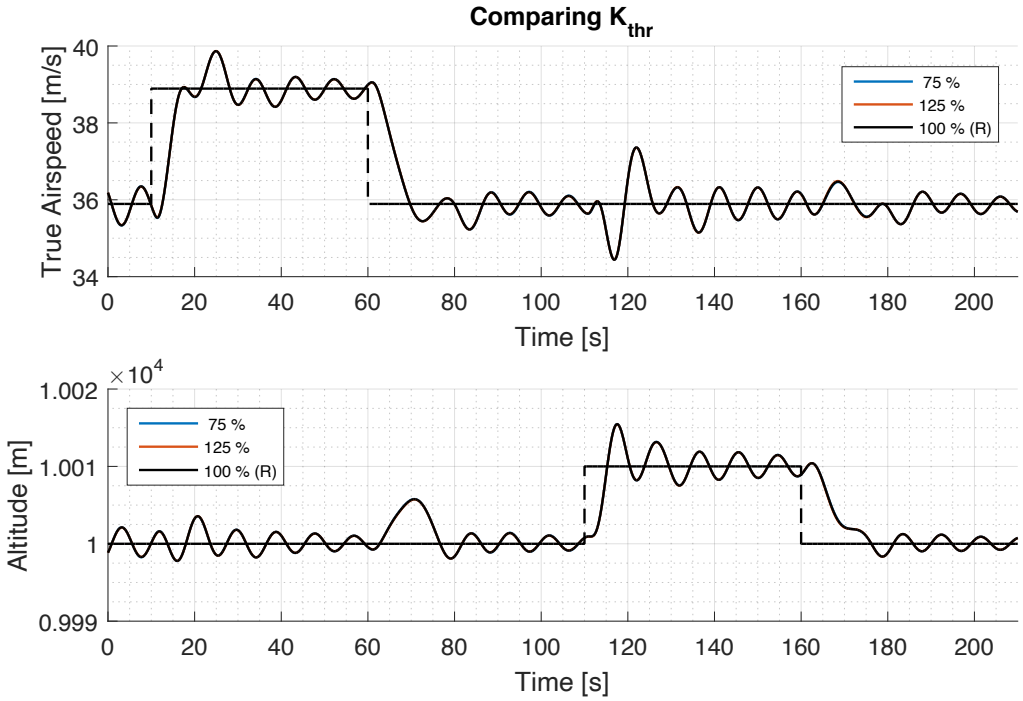

Figure 6.6: Sensitivity Analysis at 10km - K_{thr}.

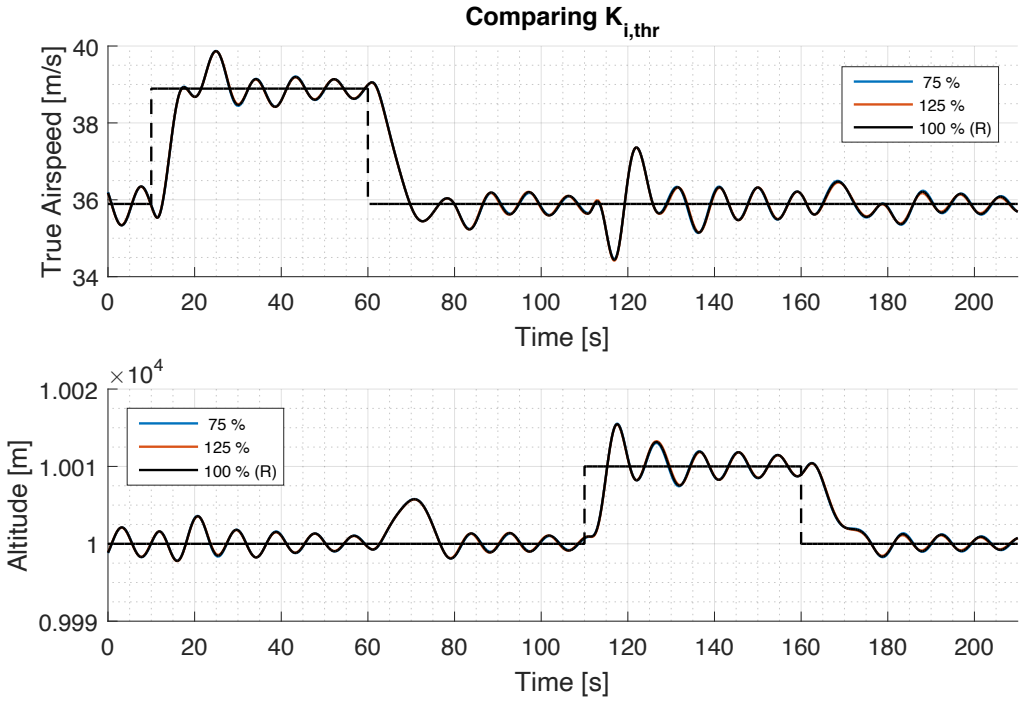

Figure 6.7: Sensitivity Analysis at 10km - $K_{i,thr}$.

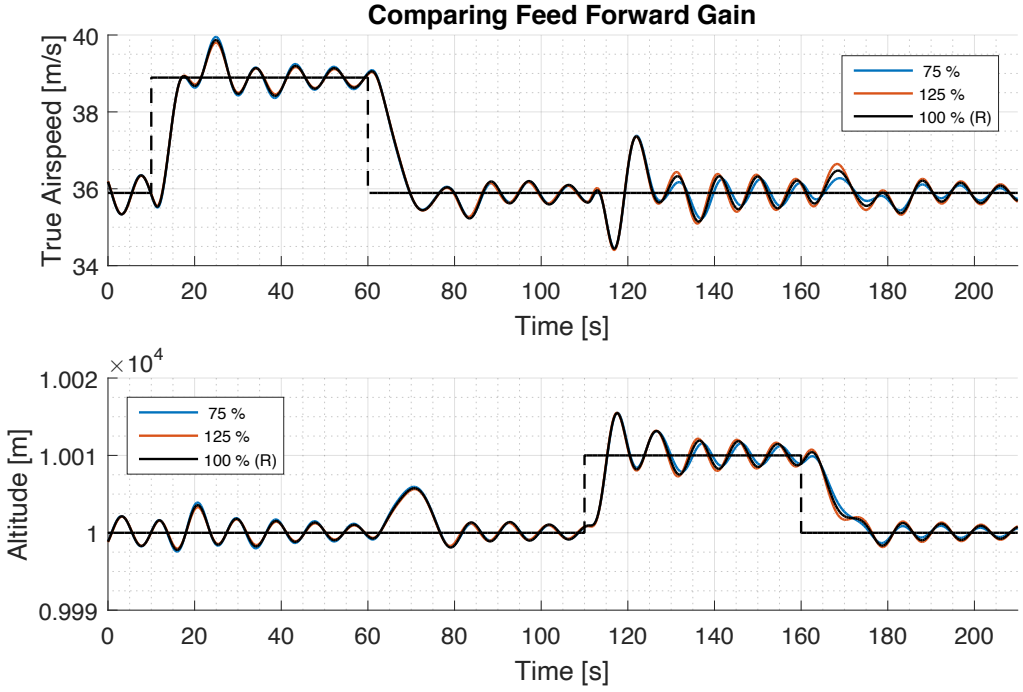

Figure 6.8: Sensitivity Analysis at 10km - K_{FF}.

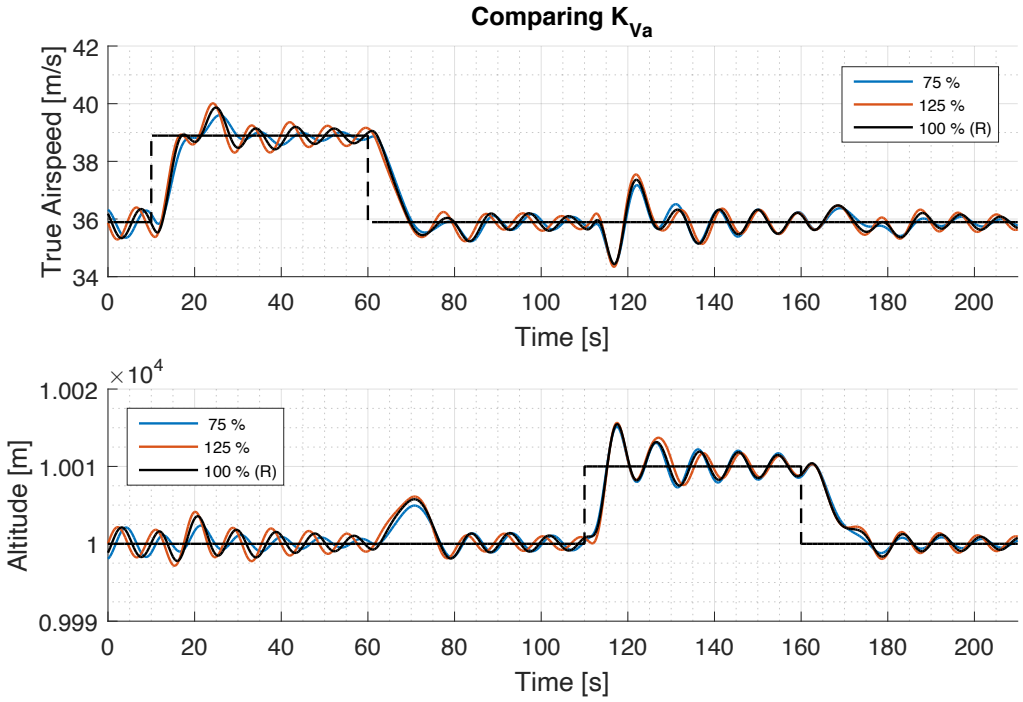

Figure 6.9: Sensitivity Analysis at 10km - K_{Va}.

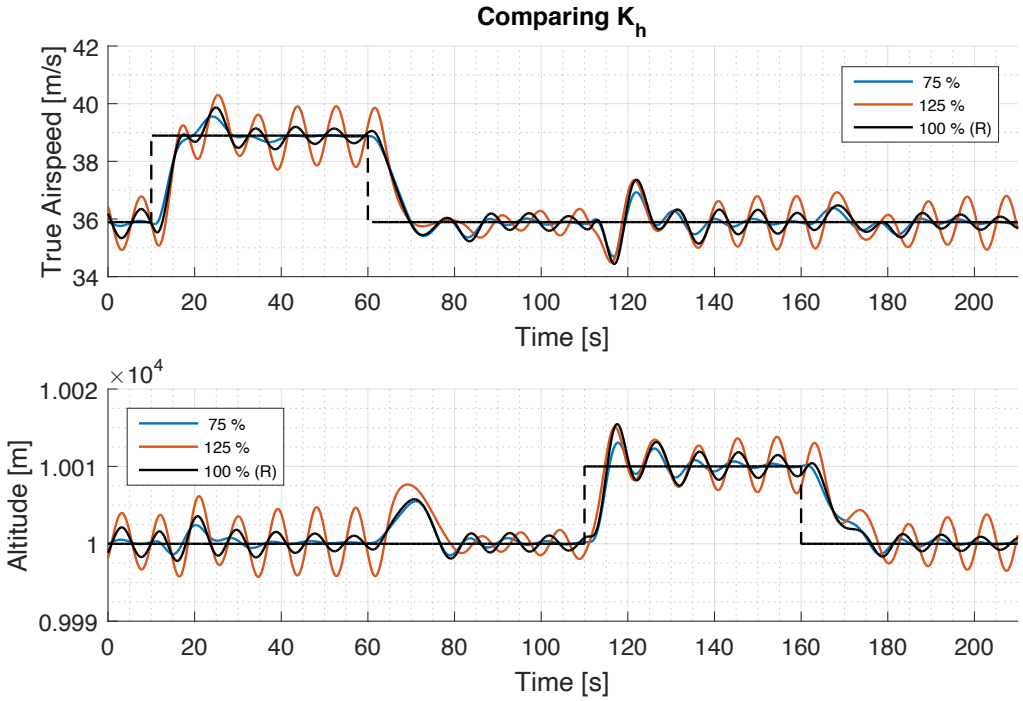

Figure 6.10: Sensitivity Analysis at 10km - K_h.

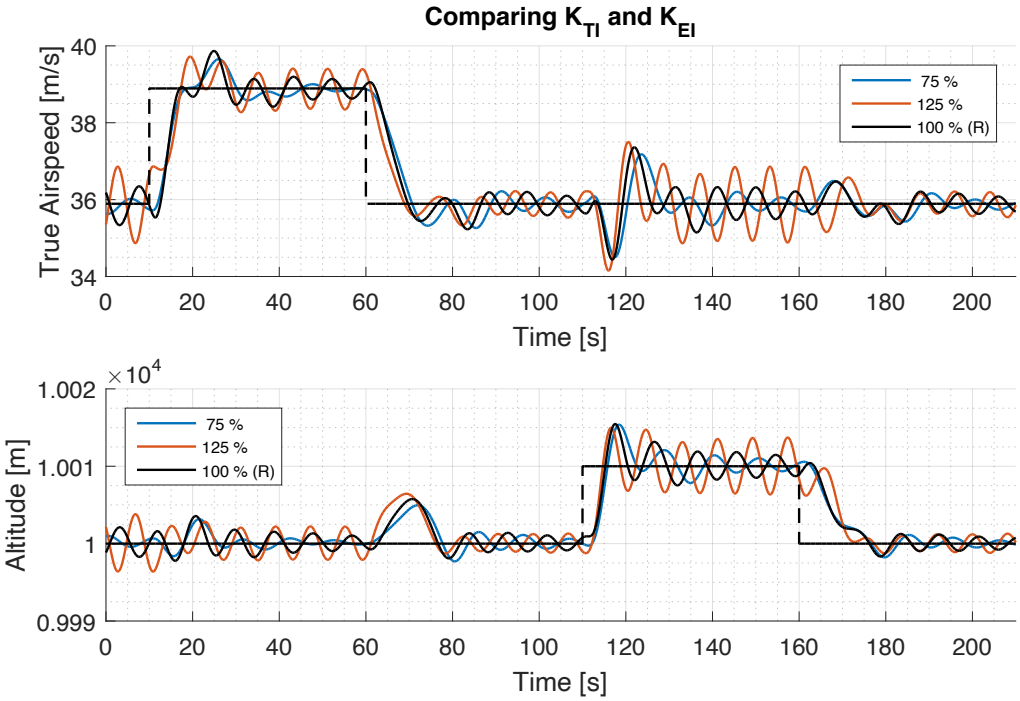

Figure 6.11: Sensitivity Analysis at 10km - K_{TI} and K_{EI}.

Followed by that, an analysis at $20km$ was made, which is shown in Figures 6.12 to 6.20. Once more K_θ is the most influential factor, considerably improving performance when its value is increased, although this time K_{Va} also shows very significant impact, almost stabilizing the system during the airspeed step when its value is decreased. This impact could be related to the increase in drag observed in Figure 5.14. All other gains are shown to have little influence on the process.

Based on these results, K_θ and K_{Va} were chosen as design variables for the gain scheduling strategy.

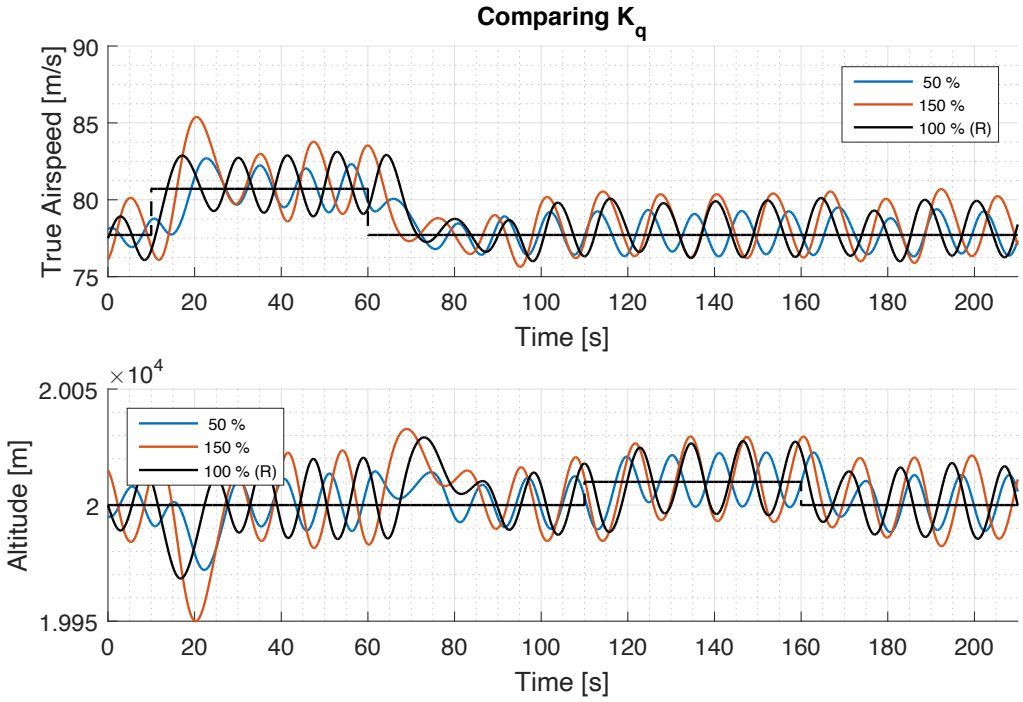

Figure 6.12: Sensitivity Analysis at 20km - K_q.

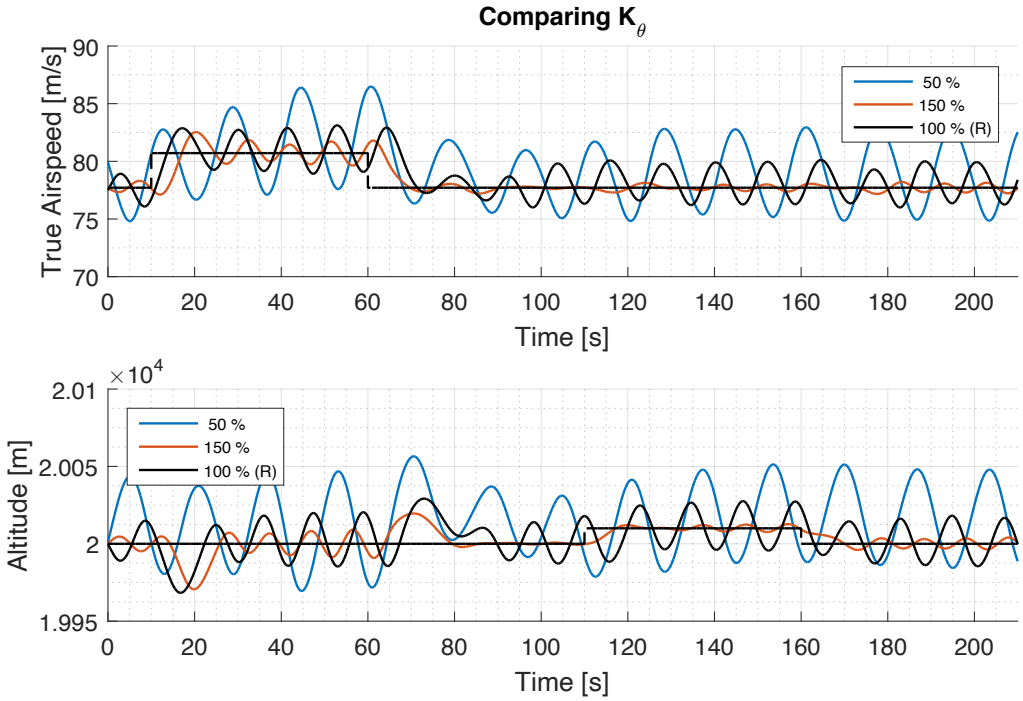

Figure 6.13: Sensitivity Analysis at 20km - K_θ.

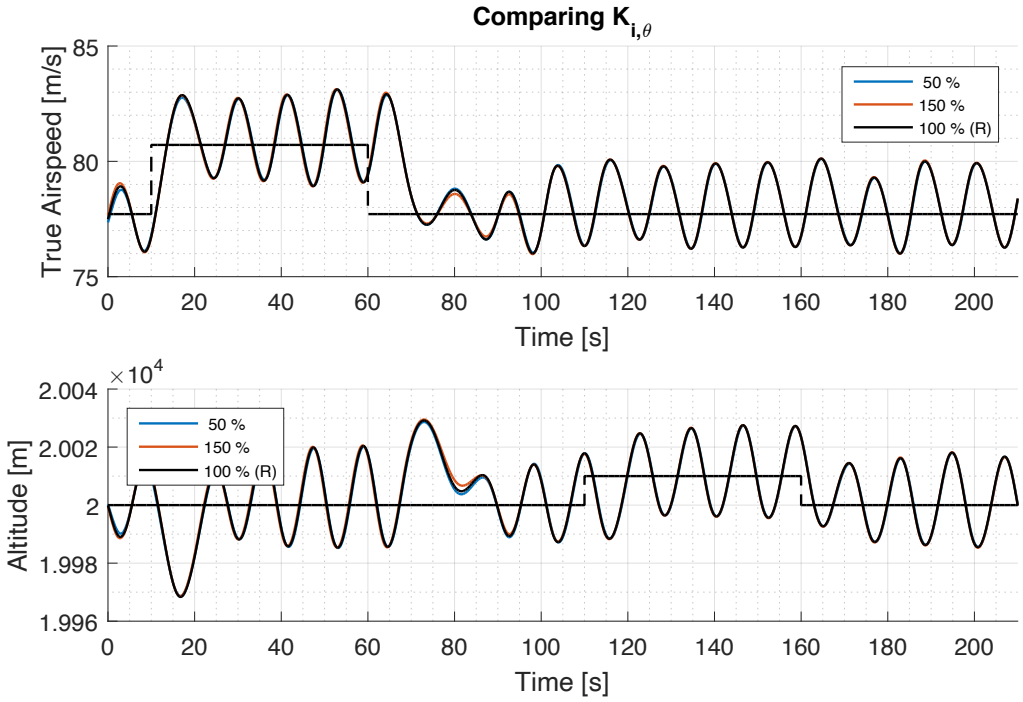

Figure 6.14: Sensitivity Analysis at 20km - $K_{i,\theta}$.

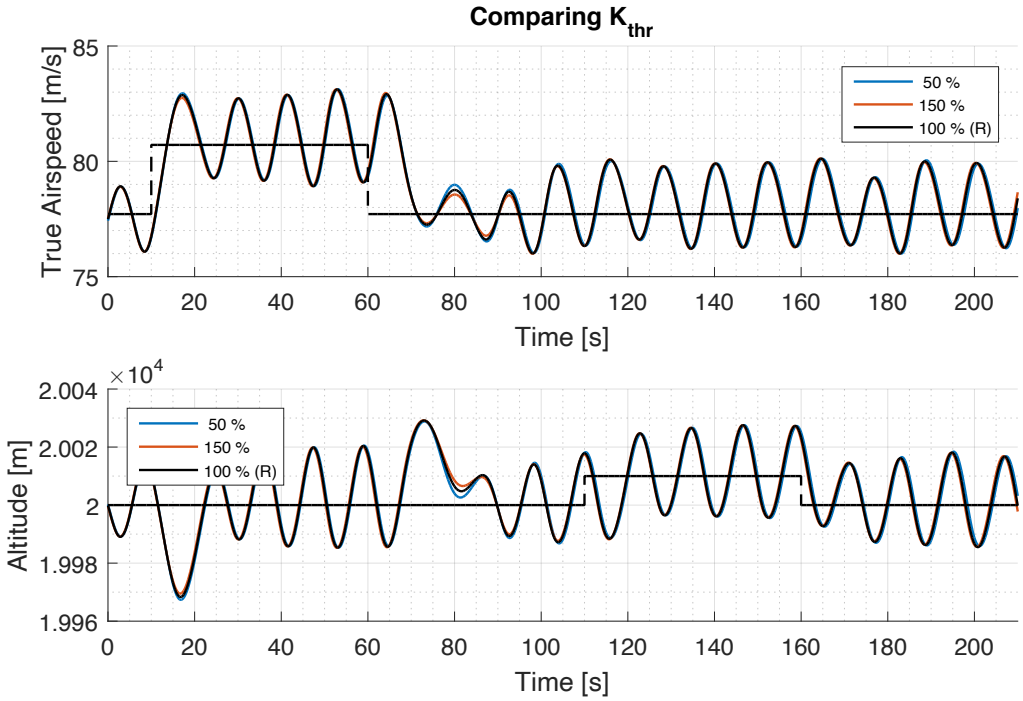

Figure 6.15: Sensitivity Analysis at 20km - K_{thr}.

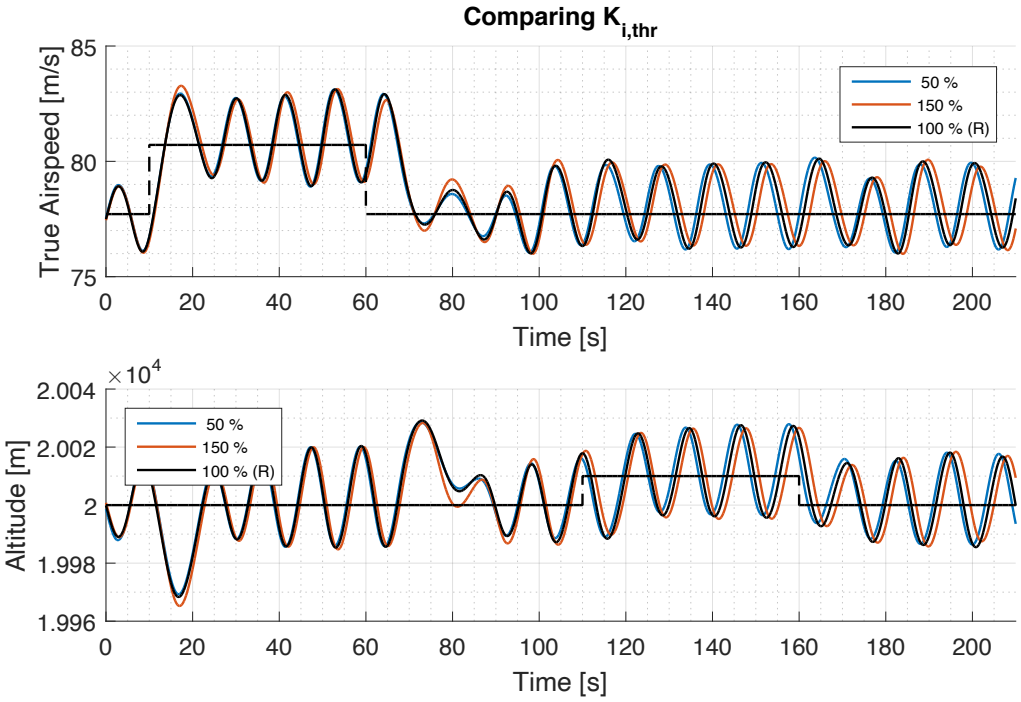

Figure 6.16: Sensitivity Analysis at 20km - $K_{i,thr}$.

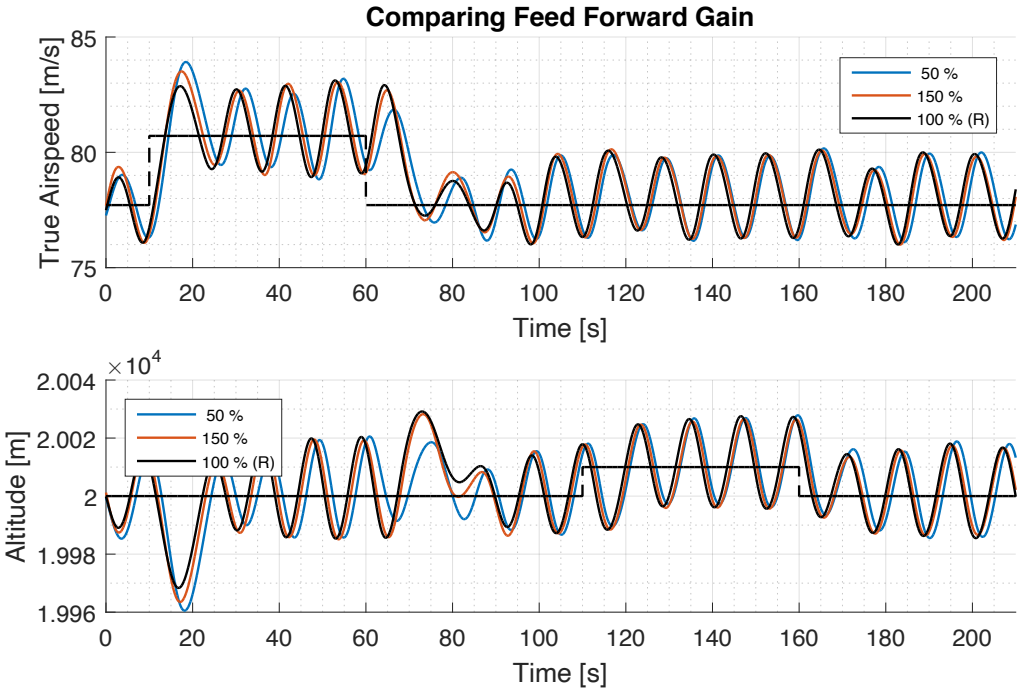

Figure 6.17: Sensitivity Analysis at 20km - K_{FF}.

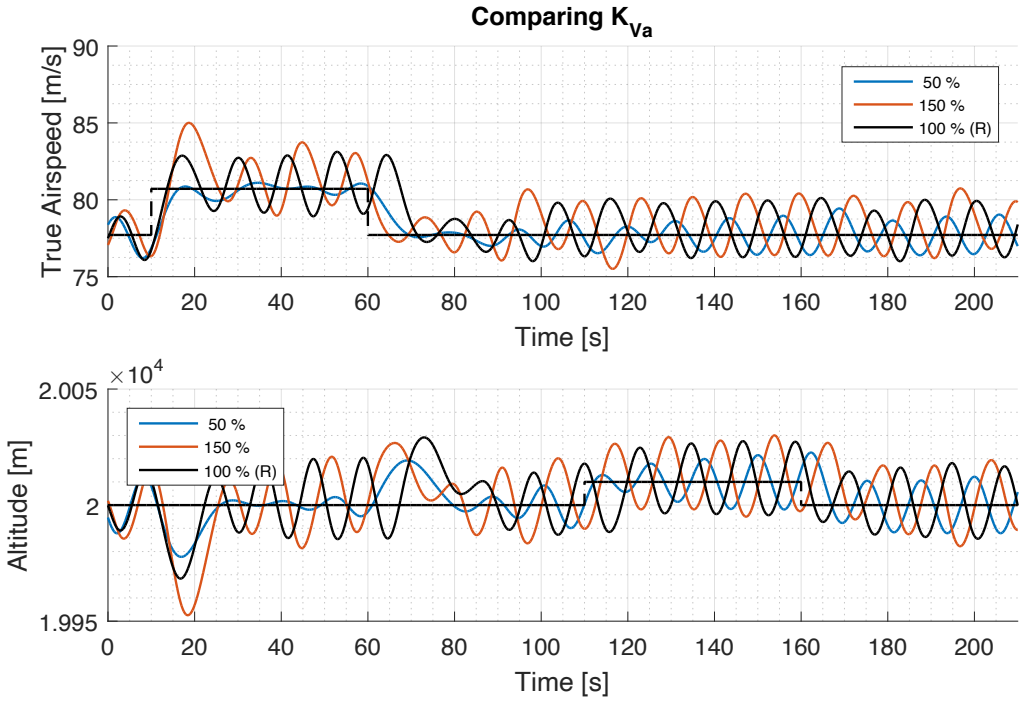

Figure 6.18: Sensitivity Analysis at 20km - K_{Va}.

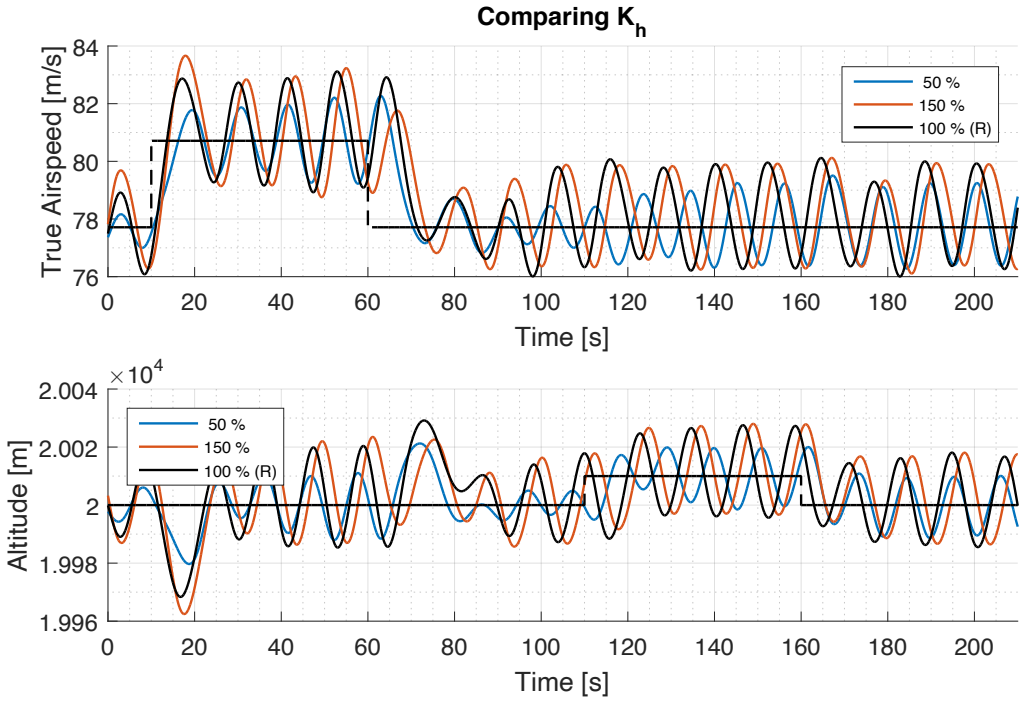

Figure 6.19: Sensitivity Analysis at 20km - K_h.

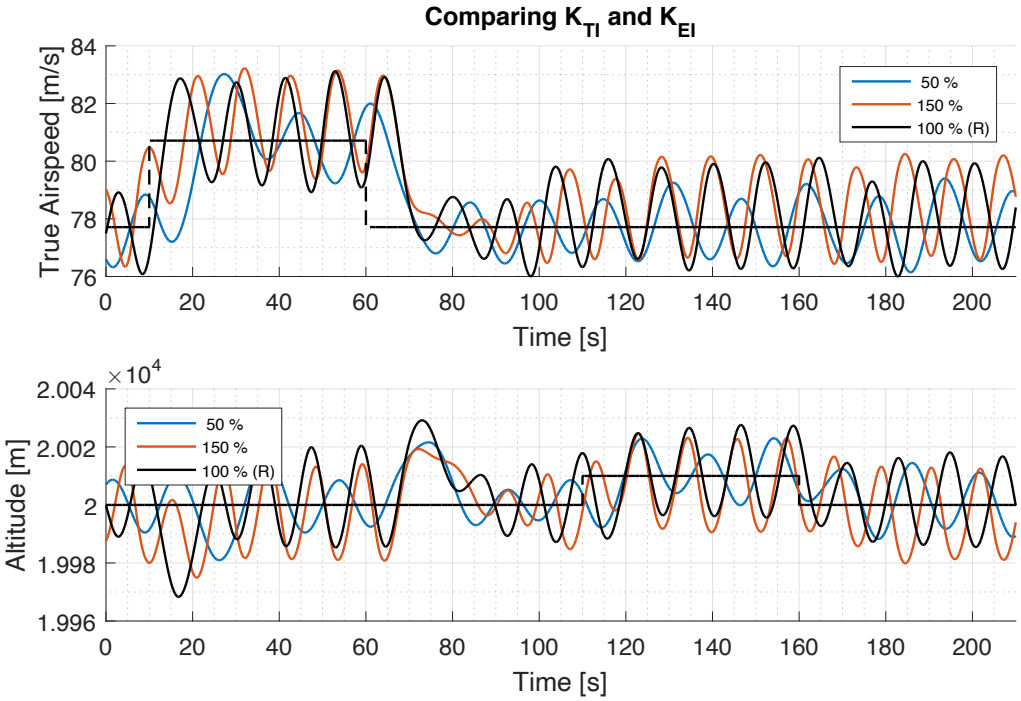

Figure 6.20: Sensitivity Analysis at 20km - K_{TI} and K_{EI}.

6.3.2 Gain Scheduling

In the following, results for the controller gains will be presented at each altitude in a normalized form $K_X/K_{X,0}$, which represents the ratio between the optimal gain value and its original value at mean sea level. The results for system performance will be shown in a single "zero-offset" plot including every four kilometer mark from $0km$ to $20km$.

First, the constant step response approach was used with starting gains being those used in flight by Elektra 2 Solar, and the results are shown in Figure 6.22. As can be observed, with the optimal gain values found, the system remains stable for the entire flight envelope. At $18km$, during the airspeed steps, the altitude varies considerably, which is likely due to the increased drag, where TECS activates its speed priority function and altitude cannot be kept constant as it normally would with said controller. Furthermore, a second overshoot is observed at $20km$ in the airspeed step also because of altitude, where it gets back to its desired state and while stabilizing it causes a small disturbance in airspeed.

Second, the optimal performance approach was used with starting gains also being optimized. This was done using the same criteria for individual optimizations, except in those only design variables K_θ and K_{Va} are changed, and for generating this initial set, all controller gains were optimized. Their values can be found on Table 6.1, and system response with them is illustrated on Figure 6.21. Figure 6.23 shows the results of the gain scheduling optimization process. When it comes to the relative values of the gains, K_θ and K_{Va}'s evolution is very close to the one of the process before, but due to the usage of optimized gains to start, the overall response looks much cleaner.

Parameter	Value	Parameter	Value
K_θ	0.2809	K_{thr}	0.8909
$K_{i,\theta}$	0.0001	$K_{i,thr}$	2.1322
K_q	0.5020	K_{FF}	0.7995
K_h	0.1524	K_{Va}	0.6878
KEP	1	KTP	1
KEI	1.5367	KTI	1.5367

Table 6.1: Initial set of optimized TECS gains for Elektra 2 Solar using the VLM model at a low altitude.

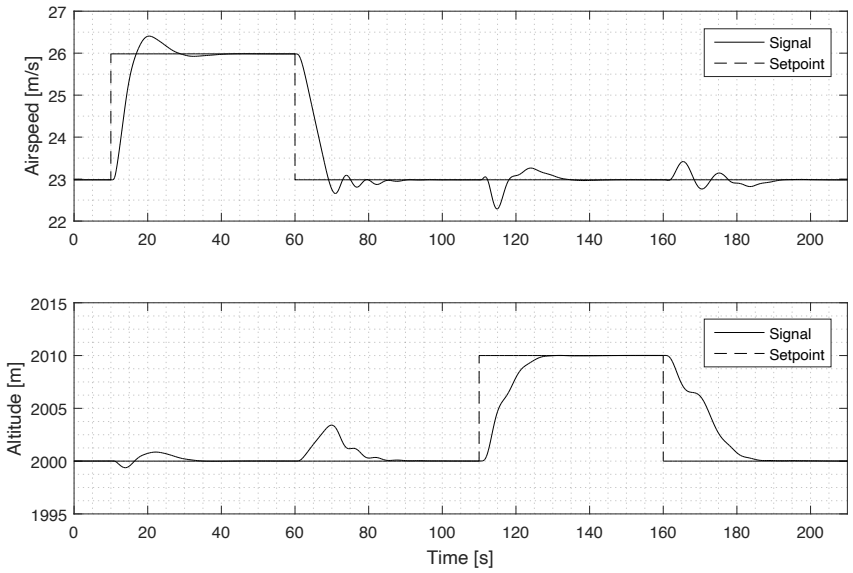

Figure 6.21: System response to steps in airspeed and altitude using the initial set of optimized gains at low altitudes and VLM model.

Lastly, cross strategies can be done, using the constant step response approach for the initial set of optimized gains and the optimal performance strategy for the initial set of flight gains, and these are shown in Figures 6.24 and 6.25 respectively. Much of the same observations as before can be made. The relative values of the gains seem to be somewhat independent of the chosen approach and the initial set of gains, and the overall system response is mostly only dependent on the initial set.

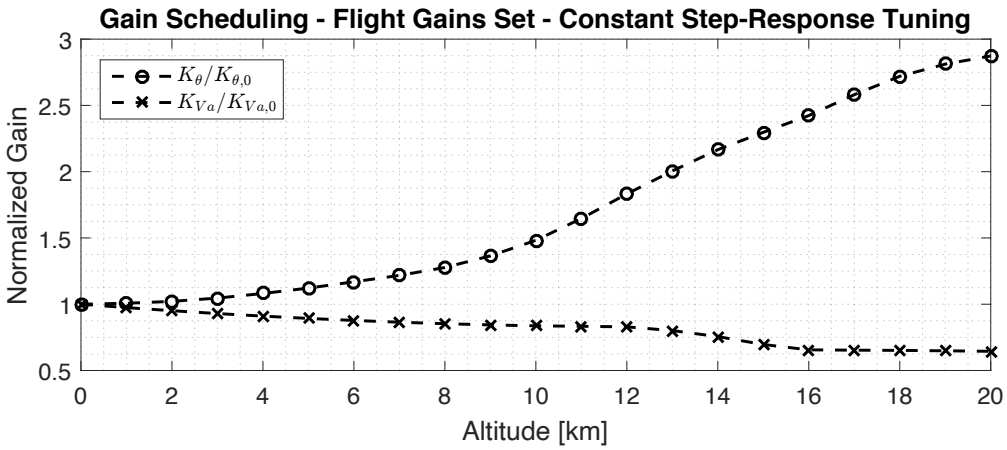

(a) Normalized gains.

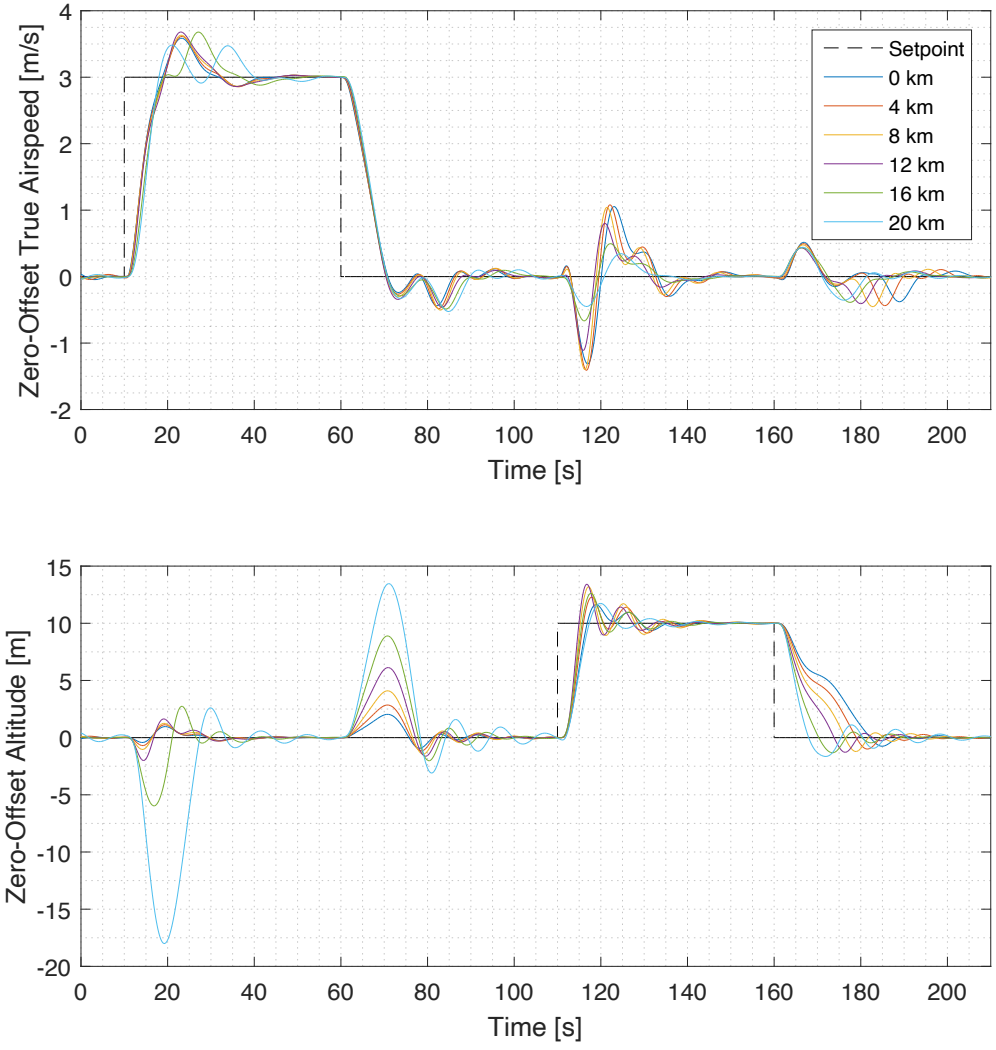

(b) System response at varying altitudes.

Figure 6.22: Optimal gains and system response for the constant step response strategy with flight gains.

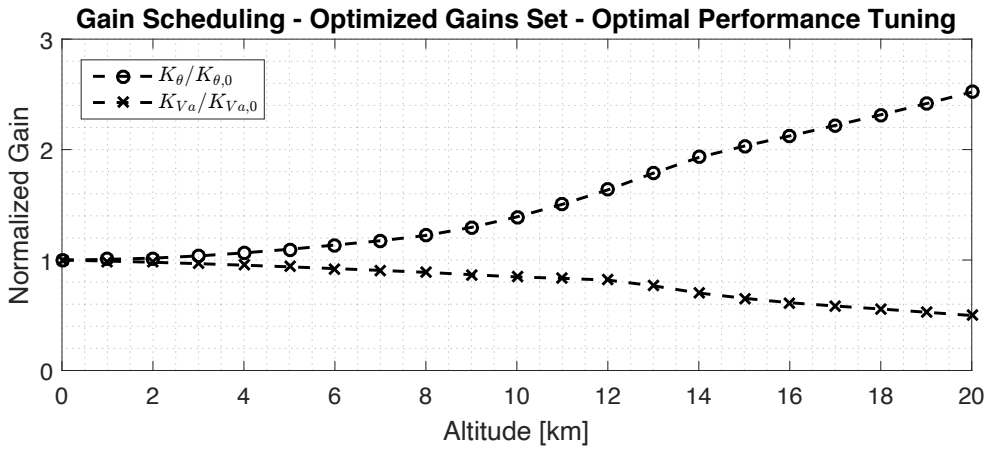

(a) Normalized gains.

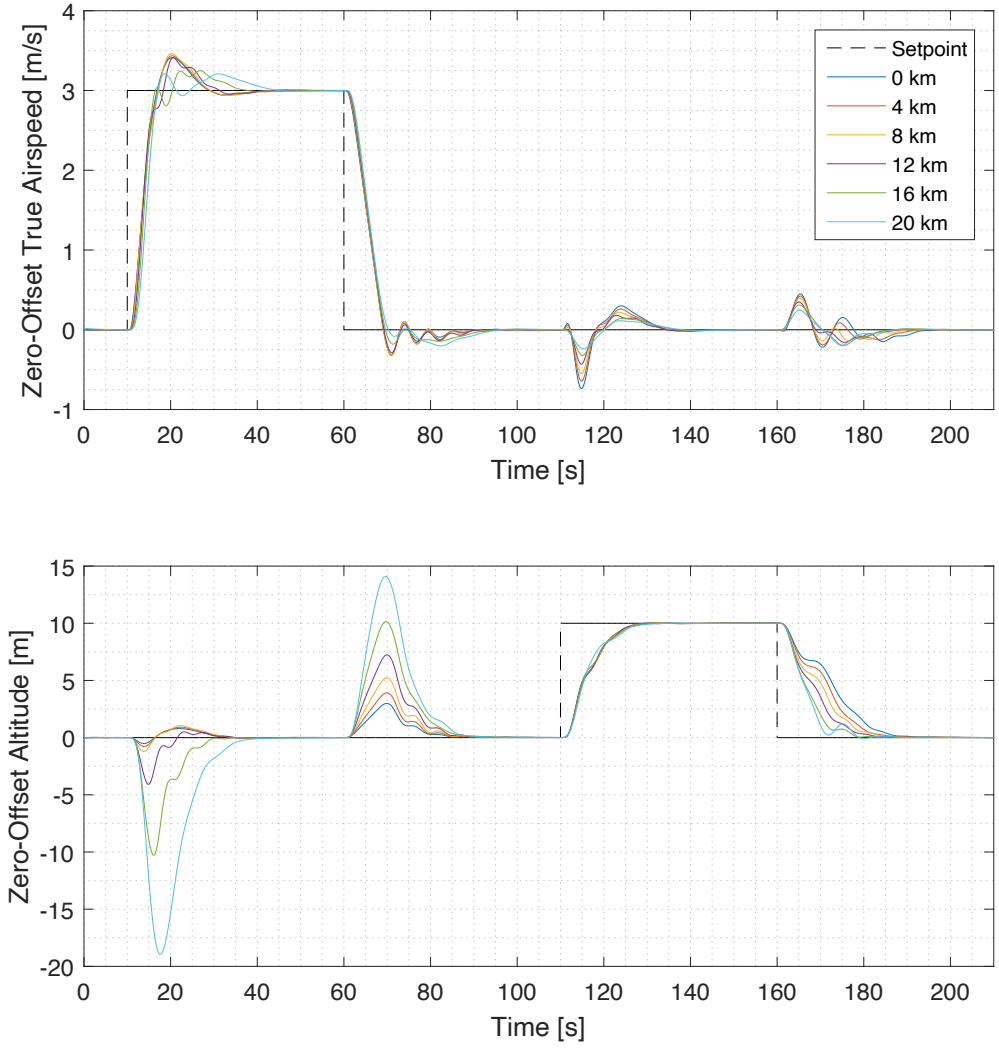

(b) System response at varying altitudes.

Figure 6.23: Optimal gains and system response for the optimal performance strategy with optimized gains.

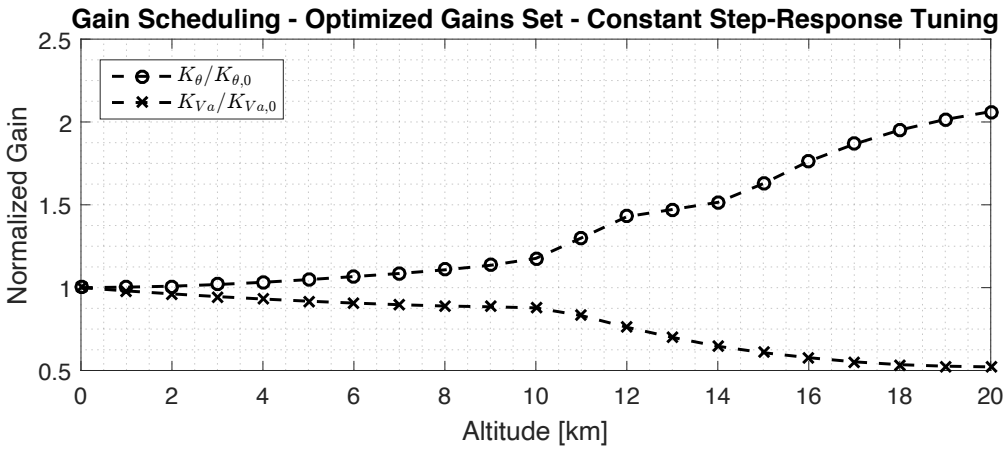

(a) Normalized gains.

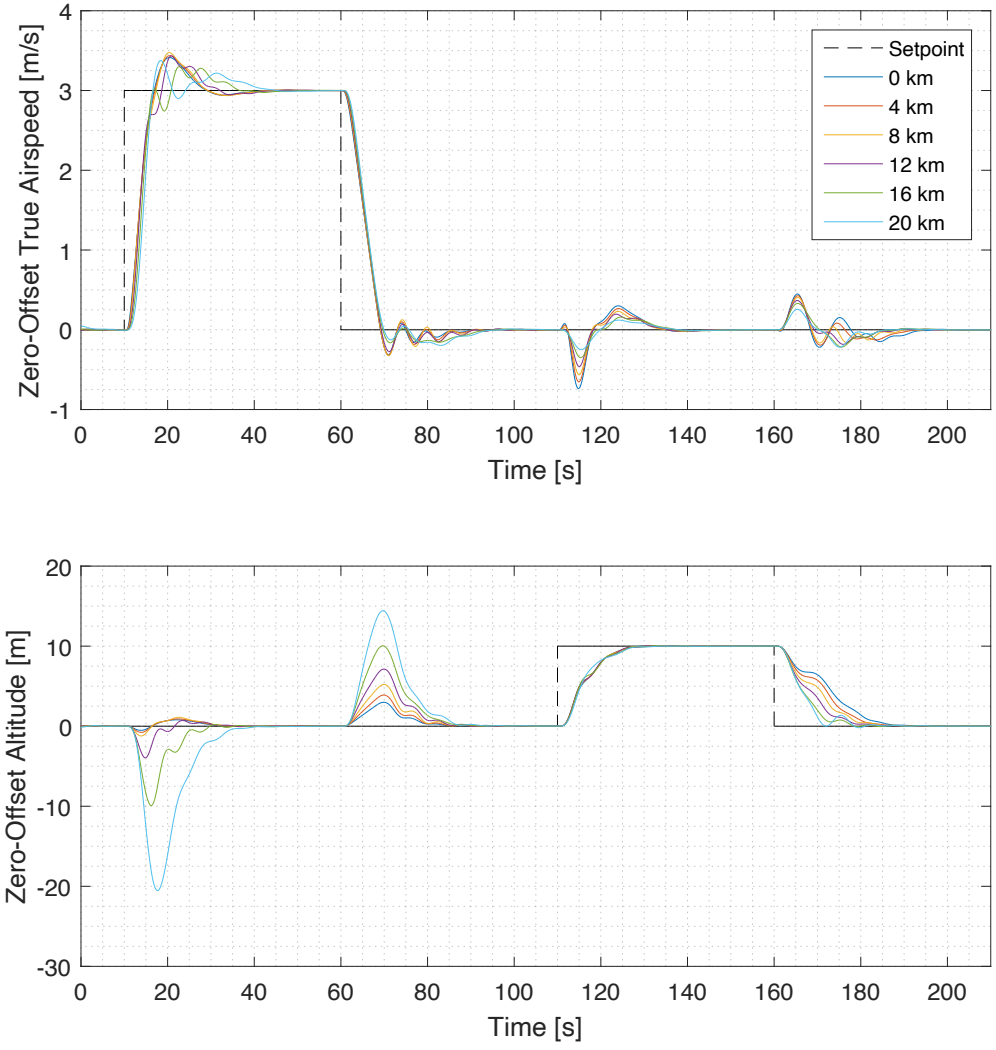

(b) System response at varying altitudes.

Figure 6.24: Optimal gains and system response for the constant step response strategy with optimized gains.

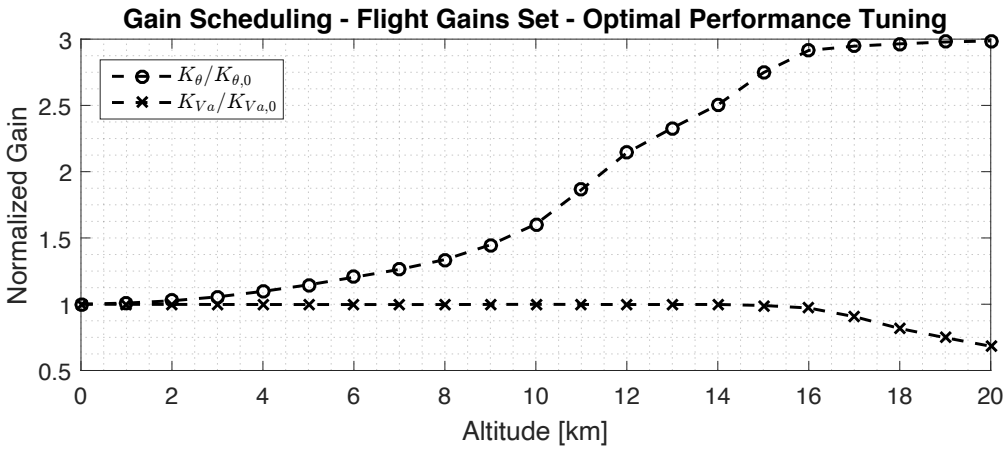

(a) Normalized gains.

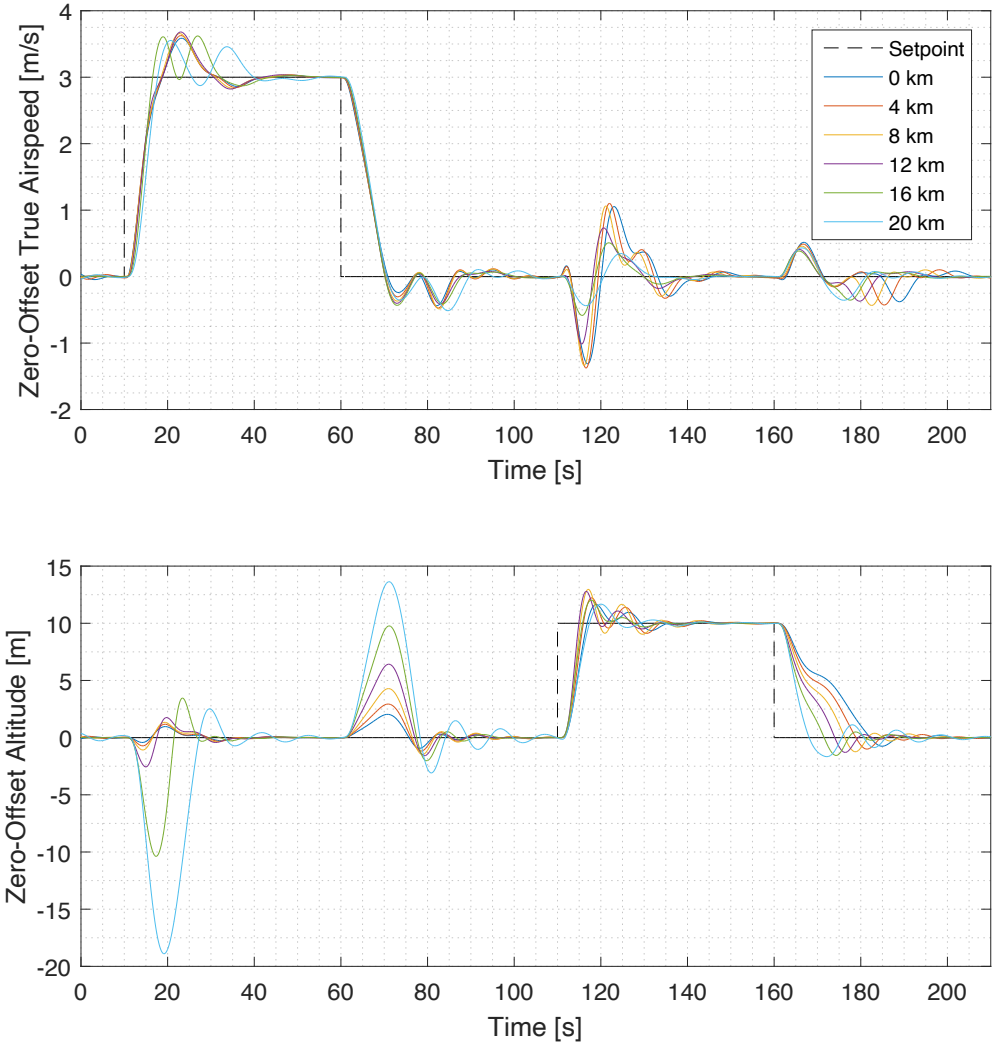

(b) System response at varying altitudes.

Figure 6.25: Optimal gains and system response for the optimal performance strategy with flight gains.

Conclusions and Outlook

In this work, the system identification process used for the presented aircraft was revised and a minimum set of aerodynamics parameters was found. A model was then developed for the Elektra 2 Solar aircraft, which proved itself to be high fidelity by FAA's standards. Furthermore, strong evidence was presented that the model structure developed yields consistent results even with different sets of data.

Using such high fidelity model, the feasibility of landing the HALE aircraft on mobile platforms was assessed. To start with, optimal sets of controller values were found for the UAV, UGV and the cooperative controller that coordinates them during the procedure. An improvement was then suggested to enhance system performance. An analysis was carried out using both deterministic and stochastic methods for the examination of disturbance rejection capabilities and full landing procedure aptness. The tests ensued very positive results, which shows promise of the strategy for future applications.

The aircraft was then modeled at many different operating points using geometry-based methods. The result was validated as being adequate for initial investigation, and an analysis on the behavior of aircraft in increasing altitudes was performed.

Finally, with the models generated for varying altitudes, a methodology to create a gain scheduling scheme was developed, and the strategy was validated by being able to ensure system stability throughout the entire flight envelope all the way up to the stratosphere, which was not possible with constant gains.

7.1 Discussion of Results

One important insight of this thesis comes from connecting results from Sections 3.4.2 and 5.3.4. First, we concluded the GPS data of states u and especially w was not of sufficient quality for a good system identification process; and later, we concluded that, for higher altitudes, vertical speed w becomes increasingly important to the aerodynamics of the aircraft, with the addition of terms related w^2 into the model structure to keep all performance metrics within acceptable ranges. Together, this means system identification of HALE aircraft will be impossible at higher altitudes if methods of acquiring better data are not considered.

Another point to be taken into account is that, while the results shown for gain scheduling do enable stratospheric flight for the considered model, that does not mean they should directly be used in the aircraft in an attempt to do that. The model used for this gain scheduling process was, as discussed, a low fidelity model, due to lack of data. The development shown here was made to validate the strategy as a whole, showing that, by using sensitivity analysis, one can find a minimal set of controller gains that need to be scheduled, and by using optimization-based controller tuning, optimal gain values can be found for each desired altitude.

For the landing procedure, while the results are encouraging, it is clear that a geometrical limit of only $80cm$ around the center of the ground vehicle in length and width is too limiting for disturbance rejection purposes for HALE aircraft. From the analysis of this work, one solution would be extending that to $3m$, which would make it a lot easier to perform such a task even in extreme conditions. Another possible solution is using a much faster ground vehicle; as previously mentioned, in this analysis, a slow vehicle model is used. With faster UGV dynamics, it would be easier to reject disturbances as well, especially in the performance-based solution, which even in the presented case had significantly better results in the lateral direction. With an aircraft with such slow dynamics such as the presented HALE one, it also makes sense that the platform should be relatively fast and play a bigger role in the procedure.

In terms of the approach procedure during landing, the MPC did not show such a big improvement in terms of runway used, and considering the implementation effort, it becomes difficult to justify a possible recommendation in a real test. However, it may be relevant to keep in mind the performance approach still has other advantages, such as its smoother transitions, and therefore, should not be discarded either.

7.2 Future Work

For further development, it would be very important to gather more flight data from different operating points for system identification purposes, ideally with better inertial and wind measurements for both longitudinal and vertical body velocities. With better data, the system identification process can become even more reliable, and with a wider range of data, extrapolation techniques such as the Global System Identification scheme proposed by Lee et al. [4] could be used. That would allow for the repetition of the gain scheduling methodology proposed in this work with a more attested model, leading to better controller synthesis.

Furthermore, as of this moment, only maneuvers for the identification of longitudinal and vertical dynamics were done. For a complete, reliable analysis for both landing and gain scheduling procedures, lateral system identification must also be considered and studied carefully.

Finally, a gain scheduling system that integrates online system identification maneuvers, such as Model Identification Adaptive Control, can also now be considered.

Bibliography

[1] United Nations Office for Outer Space Affairs (UNOOSA), "Online Index of Objects Launched into Outer Space." Available at: http://www.unoosa.org/oosa/osoindex/search-ng.jspx, 2020. Accessed on: 24.06.2020.

[2] Union of Concerned Scientists (UCS), "UCS Satellite Database." Available at: https://www.ucsusa.org/resources/satellite-database, 2020. Accessed on: 24.06.2020.

[3] Romeo G., Frulla G., and Cestino E., "Design of a high-altitude long-endurance solar-powered unmanned air vehicle for multi-payload and operations," *Proceedings of the Institution of Mechanical Engineers, Part G: Journal of Aerospace Engineering*, pp. 199 – 216, 2006.

[4] Lee J., Muskardin T., Pacz C. R., Oettershagen P., Stastny T., Sa I., Siegwart R., and Kondak K., "Towards autonomous stratospheric flight: A generic global system identification framework for fixed-wing platforms," in *2018 IEEE/RSJ International Conference on Intelligent Robots and Systems (IROS)*, pp. 6233–6240, 2018.

[5] O'Brien M., "Google, Facebook in race to build high-altitude aircraft." Available at: https://www.mercurynews.com/2015/11/28/google-facebook-in-race-to-build-high-altitude-aircraft/, November 2015. Accessed on: 24.06.2020.

[6] National Transportation Safety Board (NTSB), "NTSB Identification: DCA16CA197, accident report, aircraft: FACEBOOK UK LTD AQUILA, registration: N565AQ." Available at: https://www.ntsb.gov/_layouts/ntsb.aviation/brief.aspx?ev_id=20160701X62525&key=1, 2016. Accessed on: 24.06.2020.

[7] Burgess M., "Google quietly shut its internet drone project last year." Available at: https://www.wired.co.uk/article/google-project-titan-web-drones, January 2017. Accessed on: 24.06.2020.

[8] National Transportation Safety Board (NTSB), "NTSB Identification: DCA15CA117, accident report, aircraft: TITAN AEROSPACE HOLDINGS INC SOLARA 50, registration: N950TA." Available at: https://www.ntsb.gov/_layouts/ntsb.aviation/brief.aspx?ev_id=20150505X85410&key=1, 2015. Accessed on: 24.06.2020.

[9] Jones R. I., "The design challenge of high altitude long endurance (hale) unmanned aircraft," *The Aeronautical Journal (1968)*, vol. 103, no. 1024, p. 273–280, 1999.

[10] Facebook, "Aquila's successful second flight: Another step forward in bringing the world closer together." Available at:

https://engineering.fb.com/connectivity/aquila-s-successful-second-flight-another-step-forward-in-bringing-the-world-closer-together/, 2017. Accessed on: 24.06.2020.

[11] Muskardin T., *Autonomous Landing of Fixed-Wing Aircraft on Mobile Platforms*. PhD thesis, University of Sevilla, 2020.

[12] UAV Factory, "Penguin BE UAV Platform." Available at: `https://www.uavfactory.com/product/69`, 2015. Accessed on: 24.06.2020.

[13] UAV Factory, "Penguin BE Electric Unmanned Platform - Datasheet v1.1." Available at: `https://www.uavfactory.com/proddnlds/files_99_1585659977.pdf`. Accessed on: 24.06.2020.

[14] Elektra Solar, "Elektra One Solar OPS / UAS." Available at: `https://www.elektra-solar.com/products/elektra-one-solar-ops-and-uas`, 2011. Accessed on: 24.06.2020.

[15] Lee J., "High Fidelity Modelling for High Altitude Long Endurance Solar Powered Aircraft," Master's thesis, ETH Zürich, June 2017.

[16] Elektra Solar, "Elektra Two Solar OPS / UAS." Available at: `https://www.elektra-solar.com/products/elektra-two-solar-ops-and-uas`, 2019. Accessed on: 24.06.2020.

[17] Zadeh L. A., "From Circuit Theory to System Theory," *Proceedings of the IRE*, vol. 50, no. 5, pp. 856–865, 1962.

[18] Hamel P. G. and Jategaonkar R. V., "Evolution of flight vehicle system identification," *Journal of Aircraft*, vol. 33, no. 1, pp. 9–28, 1996.

[19] Jategaonkar R. V., *Flight Vehicle System Identification: A Time-Domain Methodology*. American Institute of Aeronautics and Astronautics (AIAA), 2 ed., 2015.

[20] Klein V. and Morelli E. A., *Aircraft System Identification Theory and Practice*. American Institute of Aeronautics and Astronautics (AIAA), 1 ed., 2006.

[21] Coelho A. F., "System Identification and Parameter Space Control Design for a Small Unmanned Aircraft," Bachelor's thesis, Instituto Federal Fluminense (IFF), Campos, Brazil, September 2017.

[22] Paez C. R., "Simulation of High Altitude Long Endurance Platforms Through Global System Identification," tech. rep., Universidad de Cadiz, July 2017.

[23] Kalra A., "System Identification and Control Design for a Stratospheric Flight Mission of a Solar Electric Aircraft," Master's thesis, École Nationale Supérieure de l'Aéronautique et de l'Espace, 2019.

[24] Muskardin T., Balmer G., Wlach S., Kondak K., Laiacker M., and Ollero A., "Landing of a fixed-wing UAV on a mobile ground vehicle," in *2016 IEEE International Conference on Robotics and Automation (ICRA)*, pp. 1237–1242, 2016.

[25] Lütjens K. H., Lau A., Pfeiffer T., Loth S., Gollnick V., Klimek H., Greßmann B., Löwa S., and Blank C., "Airport2030-Lösungen für den effizienten Lufttransport

der Zukunft," tech. rep., Deutsche Gesellschaft für Luft-und Raumfahrt-Lilienthal-Oberth eV, 2012.

[26] Laiacker M., Kondak K., Schwarzbach M., and Muskardin T., "Vision aided automatic landing system for fixed wing uav," in *2013 IEEE/RSJ International Conference on Intelligent Robots and Systems*, pp. 2971–2976, 2013.

[27] Balmer G. R., "Modelling and Control of a Fixed-wing UAV for Landings on Mobile Landing Platforms," Master's thesis, KTH Royal Institute of Technology, October 2015.

[28] Muskardin T., Balmer G., Persson L., Wlach S., Laiacker M., Ollero A., and Kondak K., "A novel landing system to increase payload capacity and operational availability of high altitude long endurance UAV," in *2016 International Conference on Unmanned Aircraft Systems (ICUAS)*, pp. 495–504, 2017.

[29] Persson L., Muskardin T., and Wahlberg B., "Cooperative rendezvous of ground vehicle and aerial vehicle using model predictive control," in *2017 IEEE 56th Annual Conference on Decision and Control (CDC)*, pp. 2819–2824, 2017.

[30] Pavani M. F. F., "Implementation and analysis of a model predictive controller for landing fixed-wing aircraft on mobile platforms," Master's thesis, TU München, 2018.

[31] Cook M. V., *Flight Dynamics Principles: A Linear Systems Approach to Aircraft Stability and Control*. Elsevier, 3 ed., 2013.

[32] Zipfel P. H., *Modeling and Simulation of Aerospace Vehicle Dynamics*. American Institute of Aeronautics and Astronautics (AIAA), 2 ed., 2007.

[33] Beard R. W. and McLain T. W., *Small Unmanned Aircraft: Theory and Practice*. USA: Princeton University Press, 2012.

[34] Stevens B. L., Lewis F. L., and Johnson E. N., *Aircraft Control and Simulation: Dynamics, Controls Design, and Autonomous Systems*. Wiley-Blackwell, 3 ed., 2015.

[35] Klöckner A., "Geometry based flight dynamics modelling of unmanned airplanes," *AIAA Modeling and Simulation Technologies Conference*, 08 2013.

[36] Brandt J. and Selig M., *Propeller Performance Data at Low Reynolds Numbers*. American Institute of Aeronautics and Astronautics (AIAA), 2012.

[37] Wang K. C. and Iliff K. W., "Retrospective and Recent Examples of Aircraft Parameter Identification at NASA Dryden Flight Research Center," *Journal of Aircraft*, vol. 41, no. 4, pp. 752–764, 2004.

[38] Morelli E. A. and Klein V., "Application of System Identification to Aircraft at NASA Langley Research Center," *Journal of Aircraft*, vol. 42, no. 1, pp. 12–25, 2005.

[39] Oliveira J., Chu Q. P., Mulder J. A., Balini H., and Vos W., *Output Error Method and Two Step Method for Aerodynamic Model Identification*. American Institute of Aeronautics and Astronautics (AIAA), 2012.

[40] Grymin D. and Farhood M., "Two-Step System Identification and Trajectory Tracking Control of a Small Fixed-Wing UAV," *Journal of Intelligent and Robotic Systems*, vol. 83, 11 2015.

[41] Lombaerts T., "Aerodynamic Model Identification of Frauke UAV," in *AIAA Atmospheric Flight Mechanics Conference*, American Institute of Aeronautics and Astronautics (AIAA), 08 2012.

[42] Mulder J., Chu Q., Sridhar J., Breeman J., and Laban M., "Non-linear aircraft flight path reconstruction review and new advances," *Progress in Aerospace Sciences*, vol. 35, no. 7, pp. 673 – 726, 1999.

[43] Kalman R. E., "A new approach to linear filtering and prediction problems," vol. 82, pp. 35–45, 03 1960.

[44] Hoff J. and Cook M., "Aircraft parameter identification using an estimation-before-modelling technique," *Aeronautical Journal*, vol. 100, pp. 259–268, 08 1996.

[45] Stalford H. L., "High-alpha aerodynamic model identification of t-2c aircraft using the ebm method," *Journal of Aircraft*, vol. 18, no. 10, pp. 801–809, 1981.

[46] Stalford H., *High-alpha aerodynamic model identification of the T-2C aircraft using the EBM system identification method*. American Institute of Aeronautics and Astronautics (AIAA), 2012.

[47] Raol J. R., Girija G., and Singh J., *Modelling and Parameter Estimation of Dynamic Systems*. The Institution of Engineering and Technology, 2004.

[48] Johansen T. A., Cristofaro A., Sørensen K., Hansen J. M., and Fossen T. I., "On estimation of wind velocity, angle-of-attack and sideslip angle of small UAVs using standard sensors," in *2015 International Conference on Unmanned Aircraft Systems (ICUAS)*, pp. 510–519, 2015.

[49] Grymin D. J., *Two-Step System Identification and Primitive-Based Motion Planning for Control of Small Unmanned Aerial Vehicles*. PhD thesis, Virginia Tech, 2013.

[50] Evans R., Goodwin G., Feik R., Martin C., and Lozano-Leal R., "Aircraft flight data compatibility checking using maximum likelihood and extended kalman filter estimation," *IFAC Proceedings Volumes*, vol. 18, no. 5, pp. 487 – 492, 1985. 7th IFAC/IFORS Symposium on Identification and System Parameter Estimation, York, UK, 3-7 July.

[51] Vepa R., *Flight Dynamics, Simulation, and Control: For Rigid and Flexible Aircraft*. Taylor & Francis, 2014.

[52] Ljung L., *System Identification: Theory for the User*. Pearson Education, 1998.

[53] Jategaonkar R., Behr R., Gockel W., and Zorn C., "Data analysis of phoenix reusable launch vehicle demonstrator flight test," *Journal of Aircraft*, vol. 43, no. 6, pp. 1732–1737, 2006.

[54] Rencher A. and Christensen W., *Methods of Multivariate Analysis*. Wiley Series in Probability and Statistics, Wiley, 2012.

[55] U.S Department of Transportation, "Airplane Simulator Qualification (AC 120-40C)," tech. rep., Federal Aviation Administration (FAA), 1995.

[56] Lambregts A., *Vertical flight path and speed control autopilot design using total energy principles*. American Institute of Aeronautics and Astronautics (AIAA).

[57] Kastner N. and Looye G., "Generic tecs based autopilot for an electric high altitude solar powered aircraft," 04 2013.

[58] Lambregts A. A., "TECS Generalized Airplane Control System Design – An Update," in *Advances in Aerospace Guidance, Navigation and Control* (Chu Q., Mulder B., Choukroun D., van Kampen E.-J., de Visser C., and Looye G., eds.), (Berlin, Heidelberg), pp. 503–534, Springer Berlin Heidelberg, 2013.

[59] Muskardin T., Coelho A., Noce E. R. D., Ollero A., and Kondak K., "Energy-Based Cooperative Control for Landing Fixed-Wing UAVs on Mobile Platforms Under Communication Delays," *IEEE Robotics and Automation Letters*, vol. 5, no. 4, pp. 5081–5088, 2020.

[60] Lambregts A. and Creedon J., *Development and flight evaluation of automatic flare laws with improved touchdown dispersion*. American Institute of Aeronautics and Astronautics (AIAA).

[61] de Sá Marques W. J., "Analysis and Comparison of Cooperative Control Architectures for Landing a Small Fixed-Wing Aircraft on a Mobile Platform," Bachelor's thesis, 2019.

[62] Skogestad S. and Postlethwaite I., *Multivariable Feedback Control: Analysis and Design*. Wiley, 2005.

[63] Ogata K., *Modern Control Engineering*. Instrumentation and controls series, Prentice Hall, 2010.

[64] Astrom K. J. and Murray R. M., *Feedback System: An Introduction for Scientists and Engineers*. Princeton University Press, 2.11b ed., 2012.

[65] Dorf R. and Bishop R., *Modern Control Systems*. Prentice Hall, 2001.

[66] Lagarias J., Reeds J., Wright M., and Wright P., "Convergence properties of the nelder–mead simplex method in low dimensions," *SIAM Journal on Optimization*, vol. 9, pp. 112–147, 12 1998.

[67] de Ockham G., Ockham W., Boehner P., and Brown S., *Philosophical Writings: A Selection*. Hackett Classics Series, Hackett Publishing Company, 1990.

[68] Balmer G., Muskardin T., Wlach S., and Kondak K., "Enhancing Model-Free Wind Estimation for Fixed-Wing UAV," in *2018 International Conference on Unmanned Aircraft Systems (ICUAS)*, pp. 1242–1247, 06 2018.

[69] Fishman G., *Monte Carlo: Concepts, Algorithms, and Applications*. Springer Series in Operations Research and Financial Engineering, Springer New York, 2013.

[70] Drela M. and Youngren H., "Athena Vortex Lattice." Available at: http://web.mit.edu/drela/Public/web/avl/, Feb. 2017. Accessed on: 24.06.2020.

[71] Deperrois A., "XFLR5." Available at: http://www.xflr5.tech/xflr5.htm, July 2019. Accessed on: 24.06.2020.

[72] Brockhaus R., Alles W., and Luckner R., *Flugregelung.* Springer-Verlag Berlin Heidelberg, 3 ed., 2011.

[73] Barbosa G. C., Bertolin R., González P. J., Neto A. B. G., and Silvestre F. J., *Fuzzy Gain-Scheduling Applied for a Very Flexible Aircraft.* 2018.